Technische Universität München
Fakultät für Physik

Abschlussarbeit im Masterstudiengang
Kern-, Teilchen- und Astrophysik

# Reinterpretation of ATLAS Searches for Supersymmetry in the Context of R-Parity Violating Models

Eingereicht von
Dominik Krauss
am
24. Februar 2015

Max-Planck-Institut für Physik
(Werner-Heisenberg-Institut)

Themensteller: PD. Dr. H. Kroha
Betreuer: Michael Flowerdew

# Acknowledgments

First of all I would like to express my particular thanks to my supervisor Mike Flowerdew, that he has always taken the time to answer my numerous questions and helped me with my problems. Without him and his enormous knowledge I would not have been able to write this thesis. Furthermore I would like to thank Hubert Kroha and the Max Planck Institute for Physics that they made this thesis possible for me. In addition to that I would like to thank Maximilian Goblirsch as well, who helped me with my questions or problems.

Moreover I would like to thank all members of the ATLAS experiment who made my analysis possible by developing the corresponding software.

Finally I would like to thank my mother and my aunt Inge for their great support.

# Abstract

Most searches for supersymmetry at the Large Hadron Collider are interpreted in the context of models in which R-parity is conserved. R-parity conservation (RPC) is introduced to prevent proton decay, but the stability of the proton can also be ensured by other mechanisms than RPC. Therefore investigation of R-parity violating (RPV) models is important to cover the full parameter space of supersymmetric extensions of the Standard Model. These models have experimental signatures that are distinctly different from those of RPC models. In particular, the lightest supersymmetric particle (LSP) can decay, which leads to final states with a large number of leptons and/or jets and a lower missing transverse energy compared to the case of RPC where the LSP is stable. It is interesting to examine to which degree existing ATLAS searches are already sensitive also to RPV models. In this thesis, ATLAS searches for supersymmetry with $\sqrt{s} = 8$ TeV proton-proton collisions are used to constrain gluino and squark production cross-sections followed by prompt RPV decays of the LSP to leptons and jets.

# Contents

**1 Introduction** . . . . . . . . . . . . . . . . . . . . . . . . . . . . . . . . . . . 1

**2 Supersymmetric Extensions of the Standard Model** . . . . . . . . . . . . . 3
  2.1 The Standard Model . . . . . . . . . . . . . . . . . . . . . . . . . . . . . . 3
  2.2 Limitations of the Standard Model . . . . . . . . . . . . . . . . . . . . . . 6
  2.3 A Symmetry Relating Fermions and Bosons . . . . . . . . . . . . . . . . . 8
  2.4 The Minimal Supersymmetric Standard Model . . . . . . . . . . . . . . . . 9
    2.4.1 Particle Content . . . . . . . . . . . . . . . . . . . . . . . . . . . . 9
    2.4.2 Gauge Coupling Unification . . . . . . . . . . . . . . . . . . . . . . 10
    2.4.3 R-Parity . . . . . . . . . . . . . . . . . . . . . . . . . . . . . . . . 11
  2.5 R-Parity Violation . . . . . . . . . . . . . . . . . . . . . . . . . . . . . 13
    2.5.1 Introduction . . . . . . . . . . . . . . . . . . . . . . . . . . . . . . 14
    2.5.2 Phenomenological Consequences . . . . . . . . . . . . . . . . . . . . 14

**3 The ATLAS Experiment** . . . . . . . . . . . . . . . . . . . . . . . . . . . 17
  3.1 The Large Hadron Collider . . . . . . . . . . . . . . . . . . . . . . . . . 17
  3.2 The ATLAS Detector . . . . . . . . . . . . . . . . . . . . . . . . . . . . 19
    3.2.1 Coordinate System . . . . . . . . . . . . . . . . . . . . . . . . . . . 19
    3.2.2 Detector Components . . . . . . . . . . . . . . . . . . . . . . . . . . 20
    3.2.3 The Trigger System . . . . . . . . . . . . . . . . . . . . . . . . . . . 22
  3.3 Particle Reconstruction and Identification . . . . . . . . . . . . . . . . . 23
  3.4 Monte Carlo Event Generation and Detector Simulation . . . . . . . . . . . 25

**4 A Selection of ATLAS Searches for Supersymmetry** . . . . . . . . . . . . . 27
  4.1 Overview . . . . . . . . . . . . . . . . . . . . . . . . . . . . . . . . . . 27
  4.2 Four-Lepton Search . . . . . . . . . . . . . . . . . . . . . . . . . . . . . 28
    4.2.1 Experimental Signatures . . . . . . . . . . . . . . . . . . . . . . . . 28

4.2.2 Event Selection and Signal Regions . . . . . . . . . . . . . . . . . . . . 30
4.2.3 Background Estimation . . . . . . . . . . . . . . . . . . . . . . . . . . . 32
4.2.4 Results . . . . . . . . . . . . . . . . . . . . . . . . . . . . . . . . . . . . 33
4.3 Zero-Lepton Search . . . . . . . . . . . . . . . . . . . . . . . . . . . . . . 36
4.3.1 Experimental Signatures . . . . . . . . . . . . . . . . . . . . . . . . . . 36
4.3.2 Event Selection and Signal Regions . . . . . . . . . . . . . . . . . . . . 36
4.3.3 Background Estimation . . . . . . . . . . . . . . . . . . . . . . . . . . . 39
4.3.4 Results . . . . . . . . . . . . . . . . . . . . . . . . . . . . . . . . . . . . 40

**5 Reinterpretation of Searches in R-Parity Violating Supersymmetric Models** 45
5.1 Production and Decay Modes . . . . . . . . . . . . . . . . . . . . . . . . . 46
5.1.1 LLE Decays . . . . . . . . . . . . . . . . . . . . . . . . . . . . . . . . . 47
5.1.2 LQD Decays . . . . . . . . . . . . . . . . . . . . . . . . . . . . . . . . . 52
5.1.3 Simulated Mass Grids . . . . . . . . . . . . . . . . . . . . . . . . . . . . 55
5.1.4 Signal Cross-Sections . . . . . . . . . . . . . . . . . . . . . . . . . . . . 57
5.2 Truth-Level Monte Carlo Studies . . . . . . . . . . . . . . . . . . . . . . . 59
5.2.1 Signal Acceptance and Sensitivity . . . . . . . . . . . . . . . . . . . . . 60
5.2.1.1 The Gluino Model with LLE Couplings . . . . . . . . . . . . . 60
5.2.1.2 The Gluino Model with LQD Couplings . . . . . . . . . . . . . 65
5.2.1.3 The Squark Model with LQD Couplings . . . . . . . . . . . . . 71
5.2.2 Model-Dependent Systematic Uncertainties . . . . . . . . . . . . . . . . 75
5.3 Results of the Reinterpretation . . . . . . . . . . . . . . . . . . . . . . . . 77
5.3.1 Statistical Procedure . . . . . . . . . . . . . . . . . . . . . . . . . . . . 78
5.3.2 Four-Lepton Analysis Reinterpretation . . . . . . . . . . . . . . . . . . 79
5.3.3 Zero-Lepton Analysis Reinterpretation . . . . . . . . . . . . . . . . . . 86
5.3.3.1 Signal Contamination in the Control Regions . . . . . . . . . . 87
5.3.3.2 The Gluino Model with LQD Couplings . . . . . . . . . . . . . 88
5.3.3.3 The Squark Model with LQD Couplings . . . . . . . . . . . . . 95

**6 Summary** . . . . . . . . . . . . . . . . . . . . . . . . . . . . . . . . . . . 103

**A Signal Yields and Acceptance Uncertainties** . . . . . . . . . . . . . . . . . 105

**Bibliography** . . . . . . . . . . . . . . . . . . . . . . . . . . . . . . . . . . 115

# Chapter 1

# Introduction

With the discovery of quantum mechanics and special relativity at the beginning of the 20th century, one of the most successful chapters in the history of physics started. The Standard Model of particle physics, which describes the fundamental interactions of elementary particles, was developed as a consequence of many ground-breaking experimental and theoretical discoveries and it has survived numerous experimental tests. The most recent success was the discovery of the Higgs boson in July 2012 by the experiments ATLAS [1] and CMS [2] of the Large Hadron Collider (LHC). The Higgs boson was the last missing particle of the Standard Model to be discovered. On the other hand, there are observations in nature that cannot be explained by the Standard Model: Dark matter and dark energy, which constitute about 95% of the energy density of the universe. In addition, gravitational interactions are not described by the Standard Model, and the fact that gravity is much weaker than the other three known forces is currently unexplained.

One of the extensions of the Standard Model that could address many of these problems is supersymmetry. Supersymmetry introduces a superpartner for each particle of the Standard Model. Both differ by half a unit of spin. The ATLAS and CMS experiments have searched for supersymmetric particles in high-energy proton-proton collisions at center-of-mass energies up to 8 TeV. Until now, no signs for supersymmetry have been found. The next run of the LHC starting in 2015 at a center-of-mass energy of 13 TeV will improve the sensitivity to many supersymmetric models.

To extend the experimental coverage of supersymmetric models in the future LHC runs it is important to better understand the strengths and weaknesses of the existing searches. Results from the supersymmetry searches of the ATLAS experiment are used in this thesis to constrain supersymmetric models not considered up to now. All models studied violate R-parity, with the result that all supersymmetric particles decay to Standard Model particles, while with R-parity conservation the lightest supersymmetric particle is stable, and assume supersymmetric particle production via the strong interaction.

The theoretical and experimental background for this work is described in the next three chapters. Supersymmetry and R-parity are introduced in chapter 2. Chapter 3 gives a brief overview of the ATLAS detector. Chapter 4 discusses searches for supersymmetry with the ATLAS experiment with emphasis on two searches that are particularly relevant for the method applied in this work. These searches are reinterpreted in terms of the supersymmetric models described in chapter 5. Finally, the conclusions are presented in chapter 6.

# Chapter 2

# Supersymmetric Extensions of the Standard Model

## 2.1 The Standard Model

The Standard Model of particle physics (SM) is the current fundamental theory of elementary particles and their interactions. It was developed in the 20th century based on the concepts of quantum field theory and on numerous experimental discoveries [3]. Up to the present day, the Standard Model has been tested in hundreds of experiments and its predictions have been verified with very high precision. For example, the predicted and the measured values of the anomalous magnetic moment of the electron agree up to the twelfth significant digit [4].

The Standard Model describes three of the four known fundamental forces, the electromagnetic, the weak and the strong interactions. It is a relativistic quantum field theory. The interactions of the Standard Model are defined by the local gauge symmetry $SU(3)_C \times SU(2)_L \times U(1)_Y$. Quantum chromodynamics, the quantum theory of the strong force, is described by the gauge group $SU(3)_C$. The associated charge quantum number, called color, assumes three values, denoted red, green and blue, with corresponding anti-colors. The $SU(2)_L \times U(1)_Y$ group defines the electroweak force which unifies the electromagnetic and weak interactions. The charges belonging to the $SU(2)_L$ and the $U(1)_Y$ group are the weak isospin, $\vec{I}$, and weak hypercharge, $Y$, respectively. The electric charge $Q$ of a particle is related to the hypercharge $Y$ and the third component $I_3$ of the weak isospin via $Q = \frac{Y}{2} + I_3$.

The fundamental particles of the Standard Model (see figure 2.1) are point-like and can be divided into two classes, fermions with half-integer spin $1/2$ and bosons with integer spin.

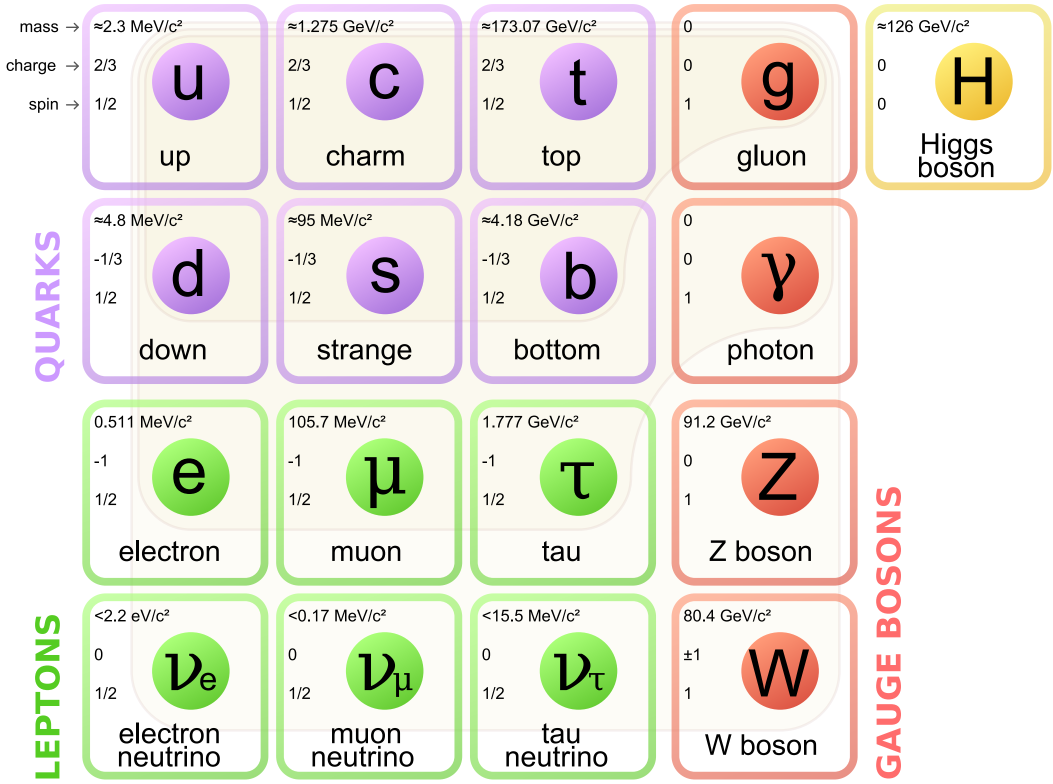

**Figure 2.1:** Overview of the particles of the Standard Model [5].

Each particle of the Standard Model has an anti-particle with opposite electric charge but the same mass, except the neutral photon, $Z$ and Higgs boson and two of the eight gluons.

The fermions are quarks and leptons which in contrast to the quarks do not participate in the strong interaction. Left-handed quarks and leptons appear in pairs, doublets of the fundamental representation of the $SU(2)_L$ gauge group weak isospin up- and down-components. Corresponding quark and lepton doublets come in three generations [6] as indicated by the first three columns in figure 2.1. Atoms consists of the charged fermions of the first generation.

Up-type quarks (called up, charm and top) and down-type quarks (called down, strange and bottom) have electric charge quantum numbers $+2/3$ and $-1/3$, respectively. The masses of the quarks increase with the generation. The top quark with a mass of about 173 GeV is the heaviest particle in the Standard Model [7]. Quarks carry color charges and exist only in color-neutral bound states, the hadrons, due to the phenomenon of confinement of coloured particles [8]. Quark confinement is related to the fact that the strength of the strong force increases with distance. There are two types of hadrons, mesons consisting of a quark and an anti-quark and baryons, like the proton or the neutron, which consist of three quarks.

The charged leptons ($e$, $\mu$, $\tau$) have electric charge quantum number $-1$. Only the electron $e$ is stable. The muon $\mu$ has a lifetime of about $2.2 \cdot 10^{-6}$ s, while the lifetime of the $\tau$ lepton is about $2.9 \cdot 10^{-13}$ s. Each charged lepton has an associated neutrino $\nu_e$, $\nu_\mu$, $\nu_\tau$, which is electrically neutral. In the Standard Model the neutrinos are massless. The observation of neutrino oscillations, however, requires them to have small masses (see section 2.2).

The interactions of the Standard Model fermions are mediated by the exchange of force carriers, the gauge bosons with spin 1. The gauge boson which has been first discovered is the photon, which is the mediator of the electromagnetic force. The strong force is mediated by eight gluons, which carry color charges and do not appear as free particles. Finally, the weak interaction is mediated by the $W^{\pm}$ and $Z$ bosons, which are the only massive gauge bosons of the Standard Model.

The fact that the vector bosons of the weak interaction are massive is in conflict with the requirement of the local gauge theories that gauge bosons are massless. In 1964, the conflict was resolved by Peter Higgs and others [9–12] by introducing a complex scalar $SU(2)_L$ doublet field. The masses of the $W$ and $Z$ bosons result from their interaction with this scalar Higgs field. The Higgs field assumes a non-zero vacuum expectation value breaking the electroweak gauge symmetry. The photon and $Z$ boson fields, $A$ and $Z$, are mixtures of the gauge fields $B$ and $W_3$ of the weak hypercharge and the third component of the weak isospin,

$$\begin{pmatrix} A \\ Z \end{pmatrix} = \begin{pmatrix} \cos\theta_W & \sin\theta_W \\ -\sin\theta_W & \cos\theta_W \end{pmatrix} \begin{pmatrix} B \\ W_3 \end{pmatrix}, \tag{2.1}$$

with the Weinberg angle $\theta_W \approx 28.74^\circ$, given by $\cos\theta_W = m_W/m_Z$.

A consequence of the Higgs mechanism of electroweak symmetry breaking is the existence of a massive neutral scalar boson, the Higgs boson $H$. In 2012, the Higgs boson was discovered by the LHC experiments ATLAS [1] and CMS [2] with a mass of about 125 GeV [13, 14].

## 2.2 Limitations of the Standard Model

The Standard Model predicts that neutrinos are massless. However, the observation of neutrino flavour oscillations for solar neutrinos [15, 16] and neutrinos from cosmic ray air showers [17], nuclear reactors [18] and neutrino beams produced by accelerators [19] requires small but non-zero neutrino masses. The values of the neutrino masses are not yet known, but upper limits of 2.05 eV, 170 keV and 18.2 MeV (95% confidence level (CL)) for $\nu_e$, $\nu_\mu$ and $\nu_\tau$, respectively, exist [20].

Besides neutrino oscillations, there are further observations that cannot be explained by the Standard Model. The most dramatic examples are dark energy and dark matter. The existence of dark matter was first postulated to explain the radial dependence of the rotation speed of galaxies, which requires more gravitational matter than it is visible [21]. More recently, the abundance of dark matter has been constrained by precise measurements of the fluctuations in the temperature of the cosmic microwave background radiation. These measurements suggest that the universe consists of 27% dark matter and 68% dark energy [22], while Baryonic matter and neutrinos, i.e. Standard Model particles, make up only about 5% of the total energy density of the universe.

A common hypothesis is that dark matter consists of weakly interacting massive particles (WIMPs). Three main strategies are used in the search for WIMPs. One is to search for them directly by detecting the recoil in elastic WIMP-nucleon scattering [23–25]. The second approach is indirect, looking for evidence of WIMP annihilation in the universe [26,27]. Finally, WIMP searches are performed in high energy proton-proton collisions at the LHC [28–33]. So far no hints of dark matter particles have been found.

Dark energy was introduced as an explanation for the observed accelerating expansion of the universe [34]. In general one would expect that the expansion slows down over time due to the attractive gravitational force. But from surveys of type Ia supernovae there is strong evidence that the expansion of the universe is accelerating [35,36]. The origin of dark energy is still unclear.

There are other theoretical issues, which indicate that the Standard Model cannot be the final theory. One is the fact that gravity, which is described very successfully at macroscopic scales by Albert Einstein's theory of general relativity [37], is not part of the Standard Model and there is no quantum field theory of gravitation yet [38].

Another shortcoming is the problem of the hierarchy of the energy scales of the fundamental interactions [39–42], i.e. the question why gravity is so much weaker than the other

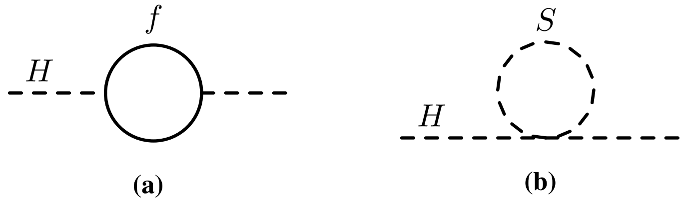

**Figure 2.2:** Feynman diagrams of loop corrections to the Higgs boson propagator for (a) fermions ($f$) and (b) scalar bosons ($S$).

forces. The large difference in the energy scales of the electroweak symmetry breaking of order $m_W$ and of quantum gravity, the Planck scale ($m_{\text{Pl}} \approx 10^{19}$ GeV) requires extreme fine-tuning to explain the smaller Higgs boson mass compared to $m_{\text{Pl}}$. Since it is a scalar particle, the mass of the Higgs boson receives quadratically divergent radiative loop corrections from all particles that couple to the Higgs boson, including yet undiscovered massive particles. The Standard Model fermion masses in contrast are protected against such corrections by chiral symmetries. The leading-order correction to the Higgs boson mass $M_H$ due to fermion loops (see figure 2.2a) is given by:

$$\Delta M^2_{H,f} = -\frac{|\lambda_f|^2}{8\pi^2}\Lambda^2 + \dots \tag{2.2}$$

where $\lambda_f$ is the Yukawa coupling constant of the fermion to the Higgs field, which is proportional to the fermion mass. $\Lambda$ is the cutoff in the fermion energies in the loop, i.e. the energy scale up to which the Standard Model is valid. If the Planck scale is assumed to be the cutoff energy, one would expect the Higgs mass in the range of the Planck mass in contrast to the observation. Without new physics beyond the Standard Model below $m_{\text{Pl}}$, it would be necessary to fine-tune the Standard Model parameters with extreme accuracy, which appears unnatural.

There are several possible solutions to the hierarchy problem, such as composite Higgs models [43, 44] or extra spatial dimensions [45]. A very elegant solution is provided by supersymmetry [46–51], which predicts a new scalar boson for every fermionic degree of freedom of the Standard Model, which leads to additional bosonic corrections to $M_H$ (see figure 2.2b):

$$\Delta M^2_{H,S} = +\frac{\lambda_S}{16\pi^2}\Lambda^2 + \dots \tag{2.3}$$

with opposite sign compared to the fermion terms in equation (2.2). If supersymmetry were an exact symmetry and $\lambda_S = |\lambda_f|^2$, the corrections cancel exactly and the Higgs mass is stable to all orders of perturbation theory. A similar cancellation of corrections to $M_H$ due to gauge boson loops occurs with their supersymmetric partners, fermions with spin $1/2$.

## 2.3 A Symmetry Relating Fermions and Bosons

Supersymmetry [52–60] is a symmetry between bosons and fermions. It is the only consistent extension of the space-time symmetries [61]. Supersymmetric transformations are generated by anti-commuting fermionic spinor operators $\widehat{Q}$, which transform bosonic states into fermionic states and vice versa:

$$\widehat{Q}\,|\text{fermion}\rangle = |\text{boson}\rangle, \qquad \widehat{Q}\,|\text{boson}\rangle = |\text{fermion}\rangle. \tag{2.4}$$

If supersymmetry were an exact symmetry, the masses of the corresponding bosonic and fermionic states had to be equal. Since there are no such particle combinations in the Standard Model, supersymmetry must be broken and new supersymmetric partner particles must be introduced for each Standard Model particle in spin differing by $1/2$ (see figure 2.3). For example, the superpartner of the electron (spin $1/2$) is the selectron, a scalar boson with spin 0. The spinor operator $\widehat{Q}$ commutes with the generators of all gauge symmetries. Thus, the sparticles have the same electric, weak and color charges as their Standard Model partners.

In the minimal supersymmetric Standard Model ‘soft’ supersymmetry breaking [46] is assumed where additional mass terms to the superpartners are introduced which break supersymmetry but maintain the cancellation of quadratically divergent corrections to all scalar masses in all orders of perturbation theory. In contrast to exact supersymmetry, corrections proportional to $\ln\Lambda$ remain,

$$\Delta M_H^2 = m_{\text{soft}}^2 \left[ \frac{\lambda}{16\pi^2} \ln\Lambda/m_{\text{soft}} + \ldots \right], \tag{2.5}$$

where $\lambda$ is a dimensionless coupling and $m_{\text{soft}}$ denotes the supersymmetry breaking and sparticle mass scale. If $\Lambda$ is close to the Planck scale, then the masses of at least some of the sparticles have to be on the order of TeV, otherwise the corrections to the Higgs mass would be too large and supersymmetry could not solve the hierarchy problem.

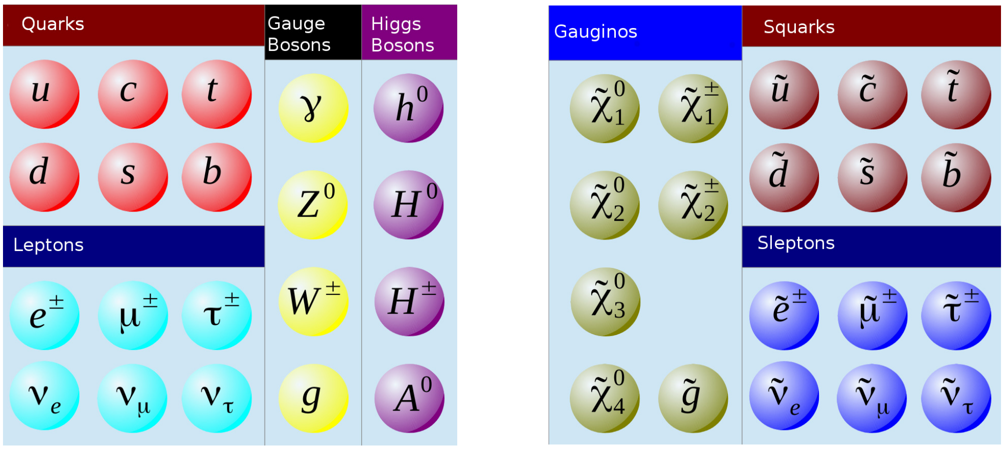

**Figure 2.3:** Overview of the particles of the MSSM [72].

There are several possible mechanisms of supersymmetry breaking. One possibility is gravity-mediated supersymmetry breaking [62–67] where supersymmetry is spontaneously broken in a hidden sector, interacting with Standard Model particles only via the gravitational interaction.

## 2.4 The Minimal Supersymmetric Standard Model

The minimal supersymmetric extension of the Standard Model (MSSM) [46, 68–71] contains only the smallest possible number of additional sparticles and Higgs bosons (see figure 2.3).

### 2.4.1 Particle Content

The symbols of the supersymmetric particles shown on the right hand side of figure 2.3 are the ones for the Standard Model particles with tilde in front, $e \to \tilde{e}$, etc. The names of the superpartners of the fermions have an additional letter ‘s’ e.g. slepton, squark etc. All sfermions are scalar particles with spin 0. The names of the superpartners of the bosons have the letters ‘-ino’ attached, e.g. higgsino, gluino, zino, etc. The gauginos, the partners of the gauge bosons, and the higgsinos have spin $1/2$. The gravitino, the superpartner of the spin-2 graviton in supergravity theories, has spin $3/2$.

The MSSM requires an additional Higgs doublet to generate the masses of the Standard Model fermions. The two Higgs doublets have eight degrees of freedom, three of which correspond to the longitudinal polarisation degrees of freedom of the massive vector bosons

$Z$ and $W^{\pm}$. The remaining five degrees of freedom are massive Higgs bosons. Besides the $h^0$ with similar properties as the Standard Model Higgs boson, there are three more scalar Higgs particles, $H^0$, $H^+$, $H^-$ and a pseudoscalar, $A^0$. Since the superpartners of the Higgs bosons and of the electroweak gauge bosons all have spin $1/2$, they in general mix to form mass eigenstates shown in figure 2.3. The four neutral spin $1/2$ particles are the neutralinos, $\tilde{\chi}_1^0$, $\tilde{\chi}_2^0$, $\tilde{\chi}_3^0$, $\tilde{\chi}_4^0$, and the four charged spin $1/2$ particles, $\tilde{\chi}_1^{\pm}$, $\tilde{\chi}_2^{\pm}$, are called charginos.

The sfermions are categorised as left- and right-handed states. Despite they are scalar particles, which are the partners of the left- and right-handed fermion fields, which have different weak interactions because of parity violation [73, 74]. Left- and right-handed sfermions $\tilde{f}_{L,R}$ may mix leading to mass eigenstates $\tilde{f}_{1,2}$ with different mass eigenvalues, for example:

$$\begin{pmatrix} \tilde{f}_1 \\ \tilde{f}_2 \end{pmatrix} = \begin{pmatrix} \cos\theta_{\tilde{f}} & -\sin\theta_{\tilde{f}} \\ \sin\theta_{\tilde{f}} & \cos\theta_{\tilde{f}} \end{pmatrix} \begin{pmatrix} \tilde{f}_L \\ \tilde{f}_R \end{pmatrix}, \tag{2.6}$$

with the mixing angle $\theta_{\tilde{f}}$. Since the mixing strength increases with the mass of the Standard Model partner, because mixing is mediated by the Higgs fields which couple to fermions proportional to their masses, only third-generation mixing for $\tilde{b}$, $\tilde{t}$, $\tilde{\tau}$ usually is considered.

### 2.4.2 Gauge Coupling Unification

An additional attractive feature of supersymmetry broken at the TeV-scale is that it naturally leads to gauge coupling unification. The strengths of the different forces are described by their respective gauge couplings $\alpha_i$, where $i = 1, 2$ and $3$ refer to the symmetry groups $U(1)_Y$, $SU(2)_L$ and $SU(3)_C$, respectively. The coupling values depend on the interaction energy scale $Q$ due to higher-order loop corrections. This effect is known as the running of the couplings. The abelian electromagnetic interaction becomes stronger with increasing energy while the non-abelian weak and strong interactions show the opposite behaviour, resulting in asymptotic freedom. In the Standard Model the coupling strengths (left) do not quite meet at high energies as shown in picture of figure 2.4, while in the case of the MSSM, they converge to a common value at an energy of about $10^{16}$ GeV [50, 75–82] (see figure 2.4, right), which corresponds to the prediction of the so-called Grand Unification scale at which all gauge interactions of the Standard Model unify in a single gauge group.

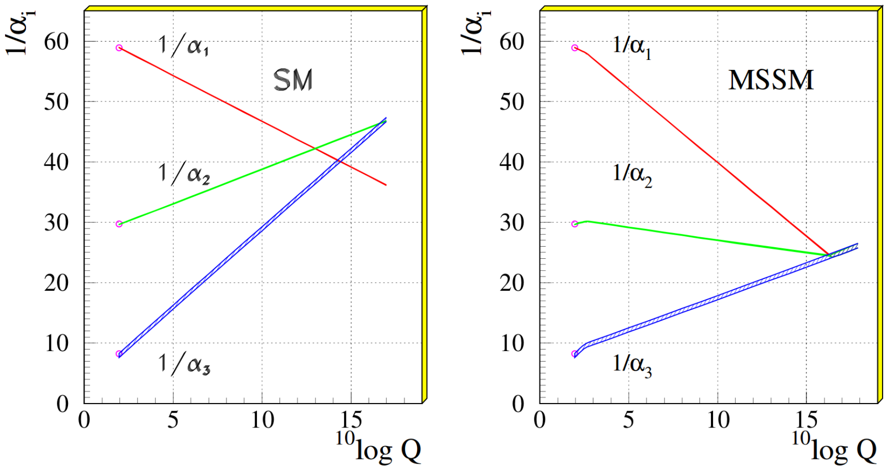

**Figure 2.4:** Energy ($Q$) dependence of the inverse gauge coupling strengths of the $U(1)_Y$ ($\alpha_1$, red), $SU(2)_L$ ($\alpha_2$, green) and $SU(3)$ ($\alpha_3$, blue) symmetries in the Standard Model (left) and in the MSSM with supersymmetry breaking scale in the TeV-range (right) [83].

### 2.4.3 R-Parity

Particle interactions invariant under supersymmetry transformations in supersymmetric extensions of the Standard Model are described by a so-called superpotential in the Lagrangian from which the forces are obtained as derivatives. The superpotential in its most general form contains gauge-invariant and renormalisable contributions leading to the violation of lepton number $L$ or baryon number $B$:

$$W_{\Delta L=\pm 1} = \frac{1}{2}\lambda_{ijk} L_i L_j \overline{E}_k + \lambda'_{ijk} L_i Q_j \overline{D}_k + \mu_i L_i H_u, \tag{2.7}$$

$$W_{\Delta B=\pm 1} = \frac{1}{2}\lambda''_{ijk} \overline{U}_i \overline{D}_j \overline{D}_k. \tag{2.8}$$

The symbols denote the chiral supermultiplets with the left-handed ($L$) and right-handed ($\overline{E}$) (s)leptons, the left-handed ($Q$) and right-handed ($\overline{U}, \overline{D}$) (s)quarks and the Higgs doublet $H_u$ giving masses to the up-type fermions. The parameters $\lambda$, $\lambda'$, $\lambda''$ and $\mu$ are coupling constants with indices $i$, $j$ and $k$ labelling the (s)fermion generations involved in the interaction. In general there can be $3^3 = 27$ independent values for each coupling $\lambda$, $\lambda'$, $\lambda''$. But, due to gauge invariance, the $\lambda$ and $\lambda''$ couplings are antisymmetric in two of their indices: $\lambda_{ijk} = -\lambda_{jik}$, $\lambda''_{ijk} = -\lambda''_{ikj}$. Therefore, there are only nine different couplings $\lambda$, $\lambda''$. For the

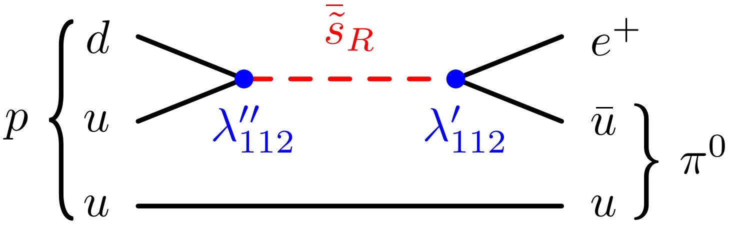

**Figure 2.5:** Example of a proton decay by exchange a virtual strange squark.

$\lambda'$ couplings there is no such restriction and all 27 combinations of generation indices are allowed. While $\lambda$, $\lambda'$ and $\lambda''$ are dimensionless, the three $\mu_i$ parameters have the dimension of mass.

Simultaneous violation of lepton and baryon number leads to a rapid proton decay, for example into a lepton and a meson as shown in figure 2.5. However, measurements at the Japanese water Čerenkov detector Super Kamiokande [84] set a lower limit of the proton lifetime of about $10^{33}$ years (90% CL) due to the absence of such a decay. There are comparable limits also from other decay modes [20]. Therefore, a new conserved multiplicative quantum number is introduced into the MSSM called R-parity,

$$P_\mathrm{R} = (-1)^{3(B-L)+2s}, \tag{2.9}$$

where $s$ is the spin of the particle. All particles of the Standard Model together with the five Higgs bosons of the MSSM have $P_\mathrm{R} = +1$ while all supersymmetric particles have $P_\mathrm{R} = -1$. Thus, R-parity conservation (RPC) has the following implications for supersymmetry searches at collider experiments:

1. The lightest supersymmetric particle (LSP) with $P_\mathrm{R} = -1$ is stable, since it cannot decay into lighter Standard Model particles, because such a final state always has $P_\mathrm{R} = +1$.
2. Mixing between Standard Model particles and their superpartners is not possible.
3. Supersymmetric particles can be produced only in even numbers (usually pairs) at colliders.
4. Supersymmetric particles, apart from the LSP, decay in cascades into final states which contain an odd number of LSPs (usually one).

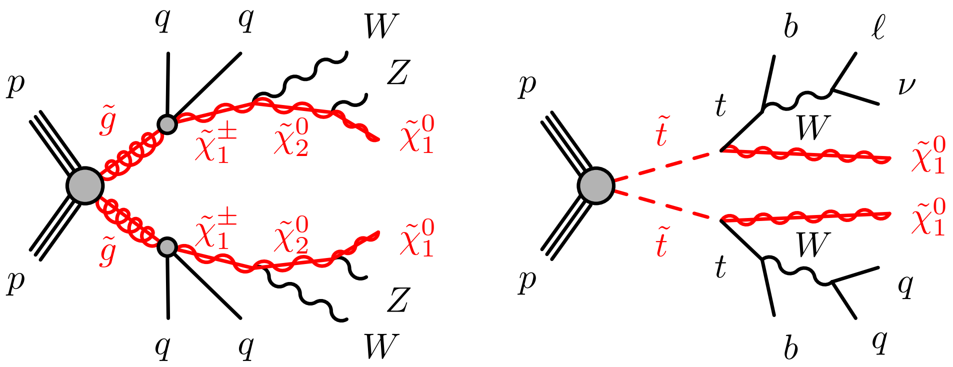

**Figure 2.6:** Examples of gluino (left) and stop (right) pair production with subsequent cascade decays to the neutralino LSP $\tilde{\chi}_1^0$ assuming R-parity conservation.

5. RPC also forbids lepton number and baryon number violating terms in equations (2.7) and (2.8).

Figure 2.6 shows two examples[1] of sparticle production and decay at the LHC if R-parity is conserved. In both cases, supersymmetric particles are produced via the strong interaction. In the right diagram each stop decays directly to the LSP (here the lighest neutralino) while in the left diagram the gluino decays in several steps. The final states of the two examples consist of several jets, charged leptons, neutrinos and two LSPs.

As mentioned in section 2.2, weakly interacting massive particles (WIMPs) are a possible candidate for dark matter. In R-parity conserving supersymmetric theories, the stable LSP is a viable WIMP candidate [85,86], if it is electrically neutral and has no color [86,87]. Usually, the lightest neutralino or the gravitino are assumed to be the LSP. The third possibility, the sneutrino, has already been ruled out by direct dark matter searches [88–90].

## 2.5 R-Parity Violation

An extensive overview of R-parity violating (RPV) supersymmetry and its phenomenological implications can be found in reference [91].

---

[1] In all diagrams of production and decay processes, particles and antiparticles are **not** differentiated, for simplicity. Thus, figure 2.6 (right) actually describes stop anti-stop pair production.

### 2.5.1 Introduction

R-parity was introduced into the MSSM for phenomenological reasons. Supersymmetric extensions of the Standard Model by themselves in general allow for baryon and lepton number violation and do not require RPC. Furthermore, the observation that there is only a negligible amount of antimatter, known as the baryon asymmetry of the universe, indicates that there must be processes that violate baryon and lepton numbers at least at high energies [92]. The main reason for introducing R-parity conservation is to prevent rapid proton decay. RPC also provides a dark matter candidate. But there are other mechanisms to protect the proton against decaying by exchange of supersymmetric particles. For instance, a less restrictive symmetry than R-parity, which only forbids some of the terms in equations (2.7) and (2.8) can be introduced. In references [93, 94], for example, baryon triality conservation is proposed, which allows for lepton number violating RPV couplings while baryon number violating terms are forbidden. Proton decay can only occur if lepton and baryon number are both violated. Thus, a restricted set of RPV interactions is compatible with a stable or sufficiently long-lived proton. Therefore the search for R-Parity violating supersymmetric models is also well motivated.

An implication of RPV supersymmetry is that all supersymmetric particles can decay directly in Standard Model particles. The LSP in general is not a dark matter candidate. Any supersymmetric particle can be the LSP, leading to experimental signatures which are not possible with RPC. Furthermore, supersymmetric particles can mix with Standard Model particles if they possess the same quantum numbers. For example, neutrinos can mix with neutralinos [95] and naturally acquire a mass [96, 97]. The mixing is caused by the bilinear $\mu_i L_i H_u$ term of the RPV superpotential (equation (2.7)). Neutrino oscillations can, therefore, be explained by RPV supersymmetry. In the case of RPC supersymmetry additional mechanisms like the seesaw mechanism are needed to explain small neutrino masses. A shortcoming of RPV supersymmetry is that it does not provide a dark matter candidate if the lifetime of the LSP is shorter than the age of the universe. Dark matter particles thus have to come from other extensions of the Standard Model [98–100].

### 2.5.2 Phenomenological Consequences

The lifetime of the LSP plays a crucial role for the collider phenomenology of RPV supersymmetric models. It depends on the values of the coupling parameters in equations (2.7) and (2.8). To observe the decay of the LSP, it must occur within the detector volume. For lifetimes greater than about $10^{-7}$ s, RPC signatures are recovered if the LSP is neutral, else it would appear as a long-lived charged particle. In the other extreme, if the decay length of the LSP is shorter than the detector resolution, the decay effectively is prompt. For LSPs lifetimes in the range of about $10^{-13}$ s to $10^{-7}$ s, the decay vertex can be resolved at the LHC. Such signatures are covered by dedicated searches [101, 102]. In this thesis only prompt LSP decays leading to leptonic signatures are studied which originate from the trilinear RPV Yukawa coupling terms with lepton number violation:

$$W_{\text{RPV}} = \frac{1}{2}\lambda_{ijk}L_iL_j\overline{E}_k + \lambda'_{ijk}L_iQ_j\overline{D}_k. \tag{2.10}$$

In the case of RPC supersymmetry, supersymmetric particles are produced in pairs, each decaying in a cascade to the LSP which escapes undetected (see chapter 3.2.2). Thus the experimental signatures of RPC signals involve charged leptons and jets produced in the cascade decays and missing transverse energy $E_{\text{T}}^{\text{miss}}$ from the two LSPs (see figure 2.6). In most RPV supersymmetric models investigated at colliders, only the LSP decays via RPV couplings leaving the pair production and the cascade decays of the sparticles unchanged compared to RPC. This assumption is motivated by low-energy constraints on the maximum RPV coupling values [103], which suppress RPV decays of other sparticles than the LSP. Due to the fact that the two LSPs of an event decay directly to Standard Model particles, the experimental signature of RPC supersymmetry of large $E_{\text{T}}^{\text{miss}}$ is lost in most cases and replaced by additional leptons and jets. Non-zero $E_{\text{T}}^{\text{miss}}$ arises in RPV supersymmetric models from neutrinos which are produced either in the LSP decay directly or in the decays of the LSP decay products, e.g. $\tau^- \to \ell^- \bar{\nu}_\ell \nu_\tau$.

If the LSP is a sfermion, the couplings in equation (2.10) lead to two-body decays to Standard Model fermions as listed in table 2.1. On the other hand, a gaugino LSP (e.g. a neutralino) undergoes a three-body decay mediated by a virtual sfermion (see the example of such a three-body decay in figure 2.7, where the neutralino decays to first and second generation leptons via the $\lambda_{121}$ coupling).

To sum up, sparticle production at the LHC can produce radically different signatures if R-parity is violated. The phenomenology of supersymmetric models with RPV is dominated by the LSP decay. Equation (2.10) introduces $9+27=36$ possible new coupling parameters that have to be investigated. Each coupling leads to a different experimental signature. Studies of RPV models leading to such LSP decays are limited so far. RPV supersymmetry studies are considerably extended in this thesis.

**Table 2.1:** Sfermion couplings to Standard Model particles from equation (2.10). $L$ and $R$ denote the particle states of left- and right-handed particles, respectively. The (s)fermion generations are labelled with the indices $i$, $j$ and $k \in 1,2,3$ (e.g. $l_1$ is an electron and $u_3$ a top quark).

| Sfermion | $\lambda_{ijk}$ coupling | $\lambda'_{ijk}$ coupling |
|---|---|---|
| $\tilde{\nu}_{i,L}$ | $l^+_{j,L} l^-_{k,R}$ | $\bar{d}_{j,L} d_{k,R}$ |
| $\tilde{l}^-_{i,L}$ | $\bar{\nu}_{j,L} l^-_{k,R}$ | $\bar{u}_{j,L} d_{k,R}$ |
| $\tilde{\nu}_{j,L}$ | $l^+_{i,L} l^-_{k,R}$ | |
| $\tilde{l}^-_{j,L}$ | $\bar{\nu}_{i,L} l^-_{k,R}$ | |
| $\tilde{l}^-_{k,R}$ | $\nu_{i,L} l^-_{j,L}$ or $l^-_{i,L} \nu_{j,L}$ | |
| $\tilde{u}_{j,L}$ | | $l^+_{i,L} d_{k,R}$ |
| $\tilde{d}_{j,L}$ | | $\bar{\nu}_{i,L} d_{k,R}$ |
| $\tilde{d}_{k,R}$ | | $\nu_{i,L} d_{j,L}$ or $l^-_{i,L} u_{j,L}$ |

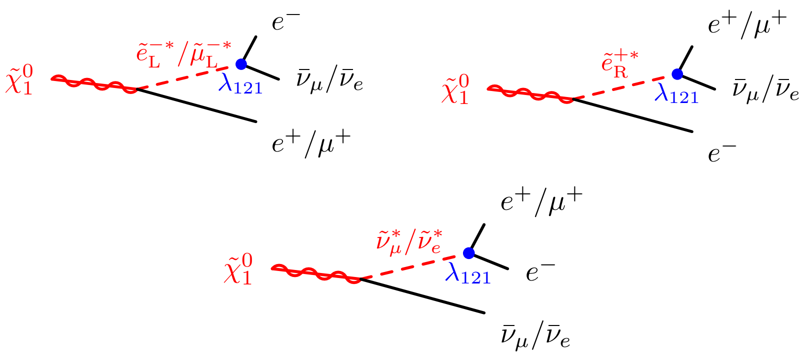

**Figure 2.7:** Diagrams of neutralino LSP decays with leptons in the final state via the $\lambda_{121}$ coupling in RPV models of supersymmetry. There are also the charge conjugate decays which are not shown.

# Chapter 3

# The ATLAS Experiment

## 3.1 The Large Hadron Collider

The ATLAS (**A** **T**oroidal **L**HC **A**pparatu**s**) experiment is one of the four principal detectors at the Large Hadron Collider (LHC) and it is the largest collider detector in the world with a length of 44 m, a diameter of 25 m and a total weight of about 7000 tons. Along with CMS (Compact Muon Solenoid), ATLAS is a multi-purpose detector for the study of electroweak symmetry breaking and searches for new physics beyond the Standard Model. Their most notable success so far is the discovery of the Higgs boson in 2012 [1,2].

The LHC is the world's largest particle accelerator with a circumference of 26.7 km. It was completed in 2009. For the construction of the LHC, the existing tunnel of its predecessor, the LEP (Large Electron-Positron) collider, was used, which runs near Geneva and the Franco-Swiss border at a depth between 50 m and 175 m at the European Organization for Nuclear Research (CERN). At the LHC, protons and/or lead nuclei are brought to collision at four intersection points where detectors are located. Most of the time the LHC is operated with protons. The particles are kept in their orbit by about 1200 superconducting dipole magnets, which are cooled with liquid helium to an operating temperature of 1.4 K. The centre-of-mass energy of the proton-proton collisions was 7 TeV in the first two years of operation and was increased to 8 TeV in 2012. This period, from November 2009 to December 2012, is referred to as 'Run 1'. For the second run beginning in 2015 the collision energy will be raised to 13 TeV.

The two beams of the LHC are divided into bunches of protons (1380 bunches per beam in 2012). Each bunch contains more than $10^{11}$ protons and is a few centimetres long. During the first two years of operation, the spacing of the bunches in time was 50 ns. Due to the high proton density at the interaction points, there are multiple proton-proton collisions per

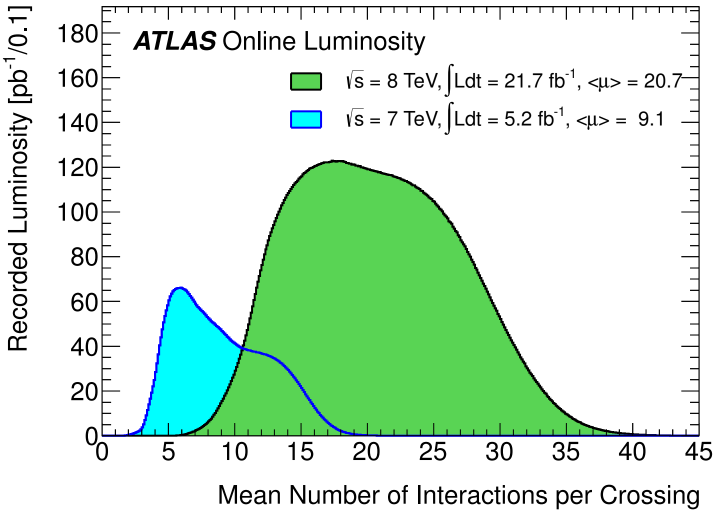

**Figure 3.1:** Distribution of the mean number of proton-proton collisions per bunch-crossing for the 7 TeV and 8 TeV runs [104].

bunch crossing, an effect called pileup. Therefore it is important to resolve which particle track belongs to a individual proton-proton collision. Figure 3.1 shows the distribution of the mean number $\mu$ of collisions per bunch-crossing in 2011 and 2012. In the 8 TeV run in 2012, the average number of collisions per bunch crossing was $\langle\mu\rangle = 21$.

An important quantity characterising the proton-proton collision rate is the instantaneous luminosity $\mathcal{L} = \frac{1}{\sigma}\frac{dN}{dt}$ which is the event rate for a given process divided by its production cross-section $\sigma$. The instantaneous luminosity depends on properties of the proton beams like the bunch-crossing frequency, the beam width and the number of protons per bunch. The total number of events per unit cross-section that occurs over a period of time is given by the integrated luminosity $L = \int \mathcal{L} dt$. Figure 3.2 shows the integrated luminosities of data delivered to and recorded by the ATLAS detector as well as the fraction where all important detector components were operational and which could be used for the data analysis. In 2012, 21.3 $\text{fb}^{-1}$ were recorded by ATLAS of which 20.3 $\text{fb}^{-1}$ satisfied all data-quality requirements.

The instantaneous luminosity is measured with different detectors and methods [105]. For the luminosity measurements in particular three forward detectors, ALFA, ZDC and LUCID, are used which are located at distances of 240 m, 140 m and 17 m from the interaction point respectively on each side of the ATLAS detector.

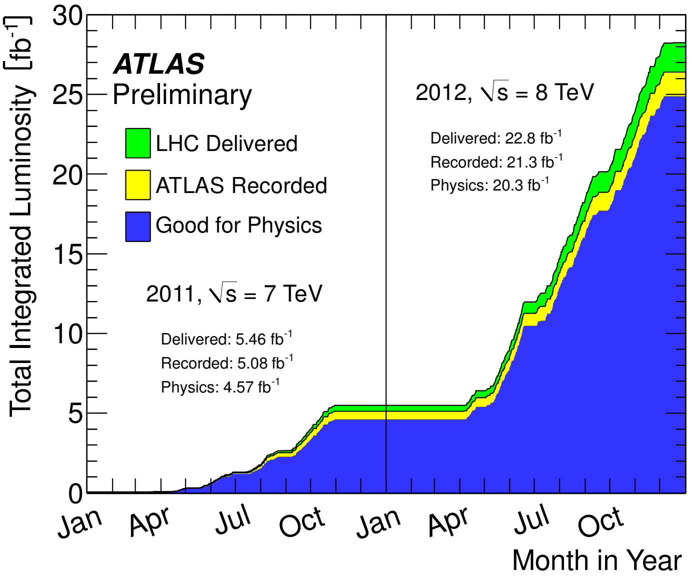

**Figure 3.2:** Integrated luminosity as a function of time, delivered by the LHC and recorded by the ATLAS detector in the years 2011 and 2012 [104].

## 3.2 The ATLAS Detector

A detailed description of the design and construction of the ATLAS detector can be found in reference [106].

### 3.2.1 Coordinate System

The ATLAS detector has a forward-backward symmetric cylindrical geometry. A right-handed coordinate system with origin at the nominal interaction point is used. The $z$-axis is directed parallel to the beam axis, the $x$-axis points toward the centre of the LHC ring and the $y$-axis vertically upwards. Polar coordinates $r$, $\theta$ and $\phi$ are also used, where the radius $r = \sqrt{x^2 + y^2}$ denotes the transverse distance from the interaction point and the azimuthal angle $\phi$ is measured from the $x$-axis in the $xy$-plane. The polar angle $\theta$ is measured with respect to the positive $z$-axis. The pseudorapidity $\eta = -\ln(\tan(\theta/2))$ is related to $\theta$ and particularly suitable for high-energy collider experiments (see figure 3.3). This is because at high energies, the pseudorapidity of a particle becomes equal to its rapidity $y = \frac{1}{2}\ln\left(\frac{E+p_z}{E-p_z}\right)$, which is invariant under Lorentz transformations along the beam axis.

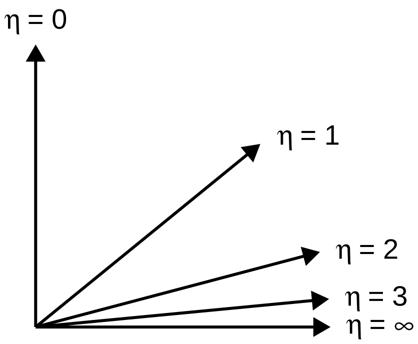

**Figure 3.3:** Sketch of pseudorapidity values, where the beam line is horizontal in the plane of the page.

### 3.2.2 Detector Components

Figure 3.4 shows the ATLAS detector and its components. The beam pipe is surrounded by the inner tracking detector which consists of a silicon pixel detector, a silicon micro-strip detector and a straw tube tracker (TRT) that can detect transition radiation. A superconducting solenoid magnet surrounds the tracker and generates a magnetic field with a strength of 2 T, which deflects electrically charged particles in order to measure their momenta. Charged particle tracks up to a pseudorapidity of $\pm 2.5$ are measured by the tracker.

The inner detector is surrounded by the calorimeters which measure the energies of particles by absorbing them completely. All calorimeters in ATLAS are sampling calorimeters, which consist of alternating active and passive layers. In the passive layers, the particles interact with the absorber material producing secondary particles that are then detected in the active layers.

The ATLAS calorimeter system consists of electromagnetic and hadron calorimeters. The electromagnetic part is optimised for the detection of electrons and photons, whereas in the hadronic part the energy depositions of hadrons and jets are measured. The electromagnetic calorimeter consists of a central barrel part and the end-caps covering pseudorapidities ranges of $|\eta| < 1.475$ and $1.375 < |\eta| < 3.2$, respectively. It uses liquid argon as active material, together with accordion shaped lead absorber plates.

In the barrel part of the hadronic calorimeter, covering $|\eta| < 1.0$ with an extension to $0.8 < |\eta| < 1.7$, steel is used as absorber and scintillating tiles as detection material. Furthermore, two hadronic end-caps cover the region $1.5 < |\eta| < 3.2$ using copper absorber plates

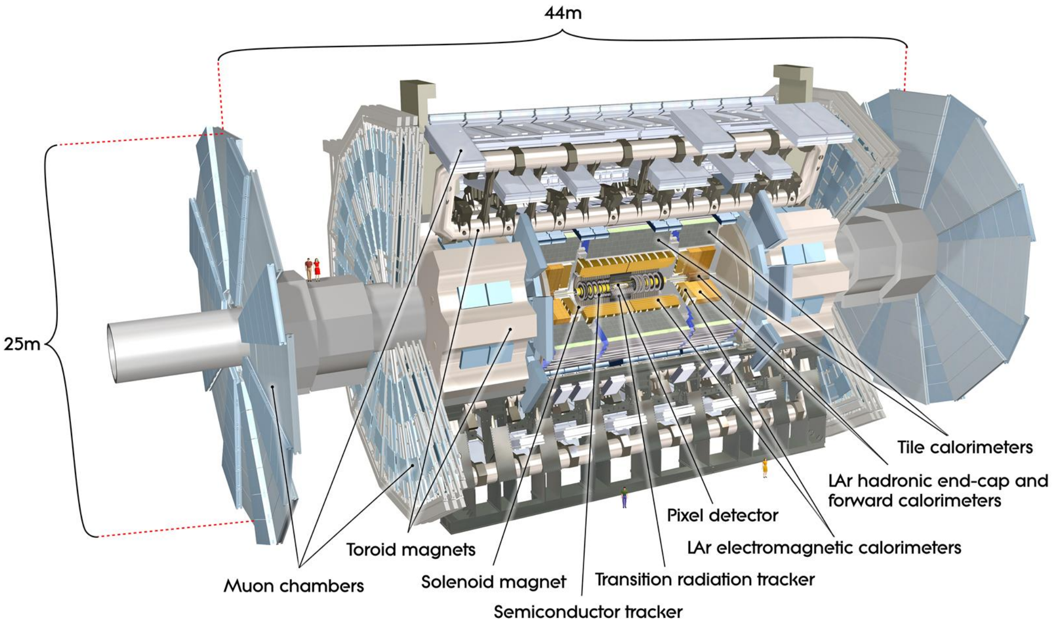

**Figure 3.4:** Cut-away view of the ATLAS detector [107].

with liquid argon as active material in the same cryostats together with the electromagnetic end-caps. The forward liquid argon calorimeters cover pseudorapidities in the range of $3.1 < |\eta| < 4.9$, and consist each of an electromagnetic and two hadronic modules with copper and tungsten as absorber, respectively.

A large solid angle range for the measurement of jets and missing transverse energy $E_{\mathrm{T}}^{\mathrm{miss}}$ is covered by the calorimeters. $E_{\mathrm{T}}^{\mathrm{miss}}$ is measured in the plane transverse to the proton beam because the $z$ component of the momenta of the quarks and gluons inside the colliding protons is unknown and particles leave the detector undetected in the forward directions with respect to the beam. Non-zero $E_{\mathrm{T}}^{\mathrm{miss}}$ indicates an momentum imbalance in the transverse plane which may be caused by undetected particles such as a neutrino or a supersymmetric particle.

The outer part of the detector surrounding the calorimeters is the muon spectrometer. Due to their long lifetime and high mass compared to electrons, muons pass through the calorimeters with only a small loss of energy. Therefore, the muon spectrometer is needed to precisely measure their trajectories and momenta. Muons passing through the spectrometer

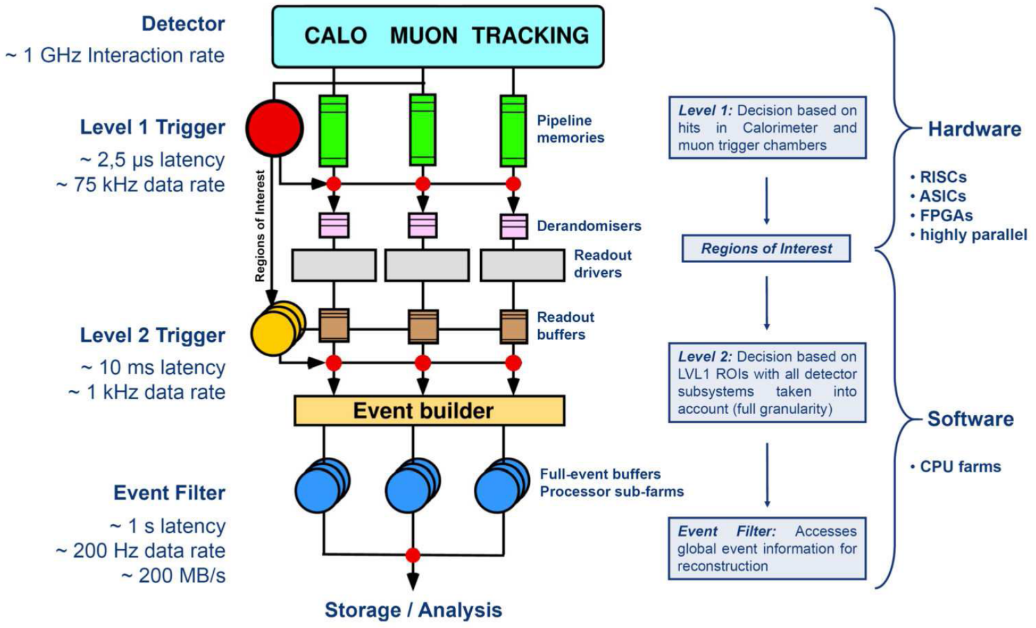

**Figure 3.5:** Overview of the ATLAS trigger system ( [108], adapted from [109]). The numbers correspond to the 7 TeV run conditions. For the 8 TeV run the final output event rate was increased, up to 400 Hz.

are deflected in a toroidal magnetic field created by superconducting magnets. The large size of the muon spectrometer is required to measure muon momenta in the 1 TeV range with a precision of 10%.

### 3.2.3 The Trigger System

The ATLAS trigger system selects collision events that are of interest for further analysis. It consists of three levels as shown in figure 3.5. In Run 1, up to 400 events out of several hundred million have been selected per second and stored to disk. The other events were discarded.

The first level of the trigger system (L1) consists of custom-made electronics which are mounted on the detectors themselves. It uses rudimentary information from the calorimeters and the muon spectrometer. Events are selected if muons, electromagnetic clusters, jets (including such from tau lepton decays), missing transverse energy or total transverse energy $E_\mathrm{T}$ are found above certain transverse momentum thresholds. Only 2.5 microseconds are available to reach a decision. The trigger objects are used to define regions of interest which are passed on to the second trigger level.

Unlike L1, the other two trigger levels are software triggers implemented on large computer farms. The second level (L2) trigger investigates the regions of interest using the full information from all detector components. It takes on average 10 ms to make a decision. For events that have passed the L2 trigger, the event builder (L3) collates information from the whole ATLAS detector and reconstructs events using the offline reconstruction algorithms. With a latency of four seconds events are written to disk at a rate of up to 400 Hz.

## 3.3 Particle Reconstruction and Identification

Events selected by the event filter are reconstructed by the offline algorithms which reconstruct tracks in the inner detector and muon spectrometer and energy clusters in the calorimeters and identify electrons, photons, muons, hadronically decaying taus, hadron jets, $b$-jets, $E_{\mathrm{T}}^{\mathrm{miss}}$ and primary interaction and secondary decay vertices. The vertex with the highest scalar sum of squared transverse momenta of associated tracks is defined as the primary vertex.

The electron reconstruction algorithm searches for seed energy clusters in the calorimeters with a transverse energy of at least 2.5 GeV. Inner detector tracks are then matched to these seed clusters in $\eta$-$\phi$ space. In 2012, the electron reconstruction efficiency was greater than 95% for electrons with $E_{\mathrm{T}} > 15$ GeV [110]. The algorithm for identifying electrons among the reconstructed candidates applies cuts on 21 discriminating variables. Three categories of electron candidates are defined, loose, medium and tight electrons, with decreasing efficiency and increasing background rejection. The electron identification efficiencies in the 8 TeV run have been measured to be 95% - 98% for loose electron identification criteria, 87% - 91% for medium electrons and 77% - 81% for tight electrons depending on the number of primary interaction vertices of pile-up events [110].

Muons are reconstructed using charged tracks in the inner detector and in the muon spectrometer. Four categories of muons are distinguished. So called stand-alone muons are reconstructed using information from the muon spectrometer alone. In this case, the muon trajectory in the muon detector is extrapolated to the beam line. Combined muons use tracks reconstructed independently in the inner detector and in the muon spectrometer which are statistically combined. Finally, inner detector tracks can be associated with track segments in the muon spectrometer or energy deposits in the calorimeters to construct segment-tagged and calorimeter-tagged muons, respectively. The reconstruction efficiency for muons of all categories in 2012 was greater than 99%, for muons with $0.1 < |\eta| < 2.5$ [111].

Jets are reconstructed using 3-dimensional calorimeter clusters called topological clusters [112]. The topological cluster algorithm searches for seed cells with energies four times larger than the cell noise. Neighbouring cells with a signal-to-noise ratio of at least two are added to the seed cell. Finally, all direct neighbours are included without a signal-to-noise ratio requirement. To separate energy depositions of particles close to each other, clusters with several internal local energy maxima are split and the topological cluster algorithm is applied to each of these as seeds. The clusters obtained in this way are then combined to jets using the anti-$k_t$ algorithm [113] with a distance parameter $R = 0.4$ in $\eta$-$\phi$ space. In 2011, the reconstruction efficiency for jets with $p_{\mathrm{T}} > 50$ GeV was close to 100% [112]. Jets with $B$-hadrons ($b$-jets) often contain a displaced secondary vertex due to the long $b$-quark lifetime of about $10^{-12}$ s. Multivariate techniques are used to identify $b$-jets using the displaced vertex and other information [114].

Tau leptons can decay either leptonically ($\tau^- \to \ell^- \bar{\nu}_\ell \nu_\tau$) or hadronically. Electrons and muons from tau decays are reconstructed using the methods described above. Hadronic tau decays are reconstructed using a dedicated algorithm [115] where jets with $p_{\mathrm{T}} > 10$ GeV and $|\eta| < 2.5$ are used as seeds. Due to the relatively longs lifetime of the tau, it often decays at a secondary vertex displaced from the primary vertex. Therefore, for each tau candidate, the best associated vertex is selected [115]. Tracks satisfying certain quality criteria and originating from this vertex are associated to the tau candidate. Hadronic tau decays contain an odd number of charged hadrons, dominantly one or three charged pions or kaons, and possibly additional neutral mesons as well as a tau neutrino. Thus hadronic tau decays are categorised as '1-prong' or '3-prong' based on the number of tracks in the core cone with radius $\Delta R < 0.2$ around the seed direction. In addition, information from tracks in the extended radial region $0.2 < \Delta R < 0.4$ is used to discriminate between tau candidates and jets. Furthermore the contribution of misidentified electrons and muons is reduced by using TRT information and muon reconstruction algorithms, respectively. Three classes of hadronic tau candidates are defined, loose, medium and tight, with identification efficiencies of 65% (45%), 55% (40%) and 35% (25%) for 1-prong (3-prong) decays, respectively [115].

The missing transverse energy is determined as the negative sum of the energies of reconstructed jets, electrons, photons, and muons as well as topological clusters in the calorimeters that are not associated to a reconstructed particle [116], separately in the $x$- and $y$-directions:

$$E_{(x,y)}^{\text{miss}} = E_{(x,y)}^{\text{miss,jets}} + E_{(x,y)}^{\text{miss},e} + E_{(x,y)}^{\text{miss},\gamma} + E_{(x,y)}^{\text{miss},\mu} + E_{(x,y)}^{\text{miss,clus}}. \tag{3.1}$$

The missing transverse energy is given by $E_{\mathrm{T}}^{\text{miss}} = \sqrt{\left(E_x^{\text{miss}}\right)^2 + \left(E_y^{\text{miss}}\right)^2}$.

## 3.4 Monte Carlo Event Generation and Detector Simulation

Predictions of Standard Model and supersymmetric processes in the ATLAS detector are obtained using detailed Monte Carlo simulations [117], which consist of three steps:

- Generation of proton-proton collision events including decays of short-lived particles.
- Simulation of the detector response to the produced particles.
- Reconstruction of the simulated events (see section 3.3).

The event generation consists of several steps. First, the hard process is simulated, in which the partons of the incoming protons interact to produce the outgoing particles (e.g. supersymmetric particles) according to the quantum mechanical matrix element calculated in perturbation theory convolved with the parton distribution functions in the proton. After that, parton showers are simulated which represent QCD corrections to the hard process due to gluon radiation. In the next step, the hadronisation of coloured particles is modelled which cannot be described by perturbation theory (see e.g. [118]). Finally, the underlying event is simulated which includes interactions from partons not involved in the hard process.

The detector response is simulated using the program Geant4 [119], in which the particle interactions with the detector components, passive materials and magnetic fields are described in detail using Monte Carlo techniques. Besides a detailed detector simulation [120], a faster, less computationally intense version can be used when high precision is less important than limited computing resources [121]. At this stage, expected signals of pileup events are added. Finally, the same algorithms as described in the last section for the data reconstruction are used to reconstruct the simulated events.

# Chapter 4

# A Selection of ATLAS Searches for Supersymmetry

## 4.1 Overview

Searches for supersymmetry with the ATLAS detector have been performed in many possible production and decay channels, in an attempt to cover as many supersymmetric scenarios as possible and not to overlook a possible signal. These searches are optimised for different production processes and final states. Strong and electroweak production of supersymmetric particles is distinguished. Gluinos and squarks are produced via the strong force, whereas sleptons and gauginos are produced via the electroweak interaction. Typical diagrams for the two production mechanisms are shown in figure 4.1. Final states are characterised by the number of leptons, jets, $b$-jets and by the missing transverse energy $E_{\mathrm{T}}^{\mathrm{miss}}$.

In this thesis, RPV supersymmetric models with leptonic LSP decays are investigated. Table 4.1 shows a selection of ATLAS searches for supersymmetry that may be sensitive to these scenarios. Two of these searches are discussed in more detail below. The four-lepton

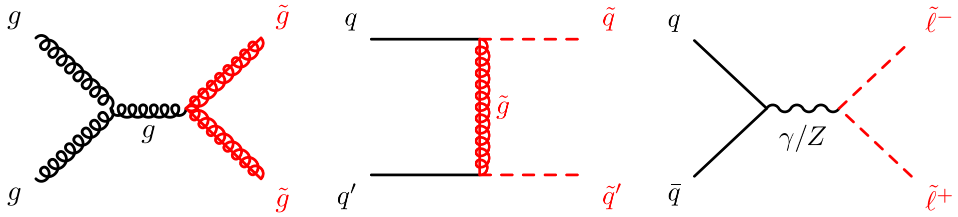

**Figure 4.1:** Examples of strong (first two) and electroweak (last) production processes of sparticles on the parton level.

**Table 4.1:** Overview of ATLAS searches for supersymmetry with increasing number of leptons in the final state referred to in the text by their short names

| Production | Short name | Final state | Reference |
|---|---|---|---|
| Strong | Zero lepton | $e/\mu$ veto, 2-6 jets and $E_T^{\text{miss}}$ | [122] |
| Strong | Multijet | $e/\mu$ veto, 7-10 jets and $E_T^{\text{miss}}$ | [123] |
| Strong (only $\tilde{t}\bar{\tilde{t}}$,$\tilde{b}\bar{\tilde{b}}$) | Two $b$-jets | $e/\mu$ veto, two $b$-jets and $E_T^{\text{miss}}$ | [124] |
| Strong | One lepton | One isolated $e/\mu$, 2-6 jets, 0-2 $b$-jets and $E_T^{\text{miss}}$ | [125] |
| Electroweak | Two leptons | Two $e/\mu$ and $E_T^{\text{miss}}$ | [126] |
| Strong (only $\tilde{t}\bar{\tilde{t}}$) | Stop $Z$ | Two or three $e/\mu$ (including $Z \to \ell^-\ell^+$ candidate), 3-5 jets, at least one $b$-jet and $E_T^{\text{miss}}$ | [127] |
| Electroweak | Three leptons | Three leptons (including up to two taus), $b$-jet veto and $E_T^{\text{miss}}$ | [128] |
| Strong | Same-sign/three leptons | Two same-sign $e/\mu$ or three $e/\mu$, 3-5 jets and $E_T^{\text{miss}}$ | [129] |
| Strong and electroweak | Four leptons | At least four leptons (including up to two taus), $E_T^{\text{miss}}$ or $m_{\text{eff}}$ | [130] |

analysis has already demonstrated excellent sensitivity to RPV models with $\lambda$ couplings [130] while the zero-lepton analysis [122] is used in the next chapter to examine RPV models with $\lambda'$ couplings.

## 4.2 Four-Lepton Search

### 4.2.1 Experimental Signatures

The four-lepton search requires at least four isolated leptons. The different final states are classified by the number of light leptons (electrons or muons) and the number of hadronically decaying taus. Signal regions with at least four, exactly three or exactly two light leptons are considered. Another important property of the final states is whether there is a $Z$ boson

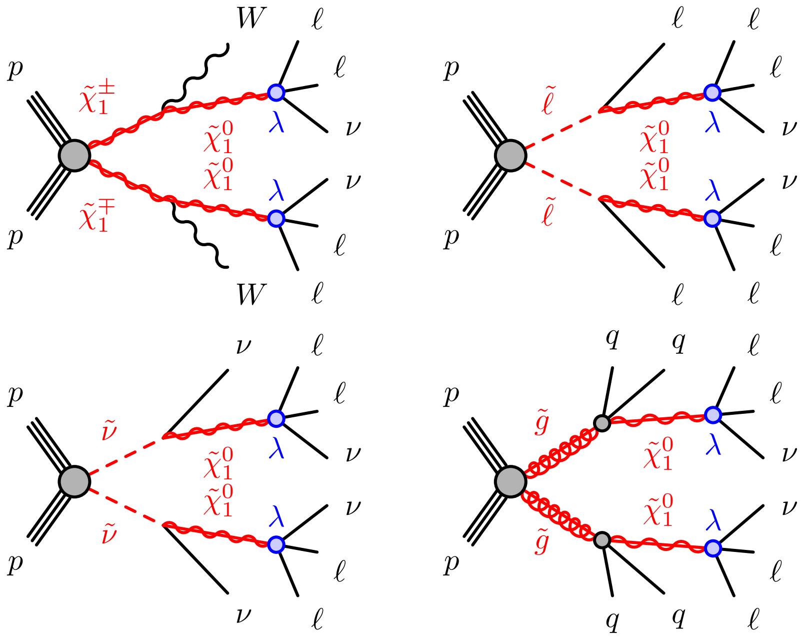

**Figure 4.2:** Diagrams for the simplified RPV models of reference [130], weak production of charginos and sleptons and strong production of gluinos.

candidate or not. A $Z$ boson candidate is an $e^+e^-$ or a $\mu^+\mu^-$ pair with an invariant mass consistent with the $Z$ boson mass.

Searches for such final states can be interpreted both in RPC and in RPV supersymmetric models. Furthermore, both strong and electroweak production processes are investigated. In the case of RPV, only simplified models where only a small subset of the supersymmetric particles contributes to the production and decay processes are considered. The other sparticles are assumed to be decoupled, i.e. that their masses are so high (4.5 TeV here) that they cannot be produced. In figure 4.2, the diagrams for the different simplified RPV models considered are shown. In all cases the neutralino is the LSP, which is assumed to be bino-like and therefore has no wino or higgsino components. For the decays of the neutralino only the subset $\lambda_{121}$, $\lambda_{122}$, $\lambda_{133}$ and $\lambda_{233}$ of the $\lambda$ couplings (see equation (2.7)) is used. Each $\lambda$ coupling is examined independently. The four simplified models differ in the next-to-lightest supersymmetric particle (NLSP) that is directly produced in the proton-proton collisions. The NLSPs considered are wino-like charginos, left-/right-handed sleptons, sneutrinos and gluinos. They decay to their Standard Model partners and a neutralino, with the exception of

**Table 4.2:** Cuts in $p_T$ and $\eta$ of the final state leptons and jets

| Object | $p_T/E_T$ [GeV] | $\|\eta\|$ |
|---|---|---|
| $e$ | $> 10$ | $< 2.47$ |
| $\mu$ | $> 10$ | $< 2.5$ |
| $\tau$ | $> 10$ | $< 2.47$ |
| jet | $> 20$ | $< 4.5$ |

the gluino which decays into two light quarks (first and second generation) plus the neutralino. Gluino production is taken into account as a benchmark model for strong production which has a much larger cross-section than electroweak production.

Information on the RPC supersymmetric models can be found in [130].

### 4.2.2 Event Selection and Signal Regions

Selected events have to fulfil several criteria. The first stage is the trigger selection. Single lepton and dilepton triggers of electrons and/or muons above certain $E_T$ or $p_T$ thresholds are used.

In the next step, lepton and jet candidates are selected with cuts in $E_T$ or $p_T$ and pseudorapidity $\eta$ which depend on the selected object (see table 4.2). Subsequently, an overlap removal procedure is used to resolve ambiguities and overlaps between multiply identified objects. For example, electrons can also be reconstructed as jets and have to be removed from the list of jet candidates in this case. For the overlap removal a minimum geometric angular distance between the momentum vectors of objects is required. If two objects are closer then required, one or even both objects are discarded. After the overlap removal, all $e^+e^-$ and $\mu^+\mu^-$ pairs with an invariant mass below 12 GeV are removed to suppress light leptons originating from Drell-Yan processes [131] and low-mass resonance decays.

In the last step after the preselection, the final objects are selected by applying additional criteria. Electrons and muons have to be isolated from hadronic activity in the tracker and calorimeters, i.e. the scalar sum of the transverse momenta of all tracks within a certain cone around an electron or muon candidate has to be smaller than a given threshold using information from the inner detector and the calorimeters. The axis of jets is required to be within $|\eta| < 2.5$.

**Table 4.3:** Signal regions of the four-lepton search

| | $N(\ell)$ | $N(\tau)$ | Z-veto | $E_{\mathrm{T}}^{\mathrm{miss}}$ [GeV] | | $m_{\mathrm{eff}}$ [GeV] |
|---|---|---|---|---|---|---|
| SR0noZa | $\geq 4$ | $\geq 0$ | SFOS, SFOS + $\ell$ / SFOS | $> 50$ | | - |
| SR1noZa | $= 3$ | $\geq 1$ | SFOS, SFOS + $\ell$ | $> 50$ | | - |
| SR2noZa | $= 2$ | $\geq 2$ | SFOS | $> 75$ | | - |
| SR0noZb | $\geq 4$ | $\geq 0$ | SFOS, SFOS + $\ell$ / SFOS | $> 75$ | or | $> 600$ |
| SR1noZb | $= 3$ | $\geq 1$ | SFOS, SFOS + $\ell$ | $> 100$ | or | $> 400$ |
| SR2noZb | $= 2$ | $\geq 2$ | SFOS | $> 100$ | or | $> 600$ |
| | $N(\ell)$ | $N(\tau)$ | Z-requirement | $E_{\mathrm{T}}^{\mathrm{miss}}$ [GeV] | | |
| SR0Z | $\geq 4$ | $\geq 0$ | SFOS | $> 75$ | | - |
| SR1Z | $= 3$ | $\geq 1$ | SFOS | $> 100$ | | - |
| SR2Z | $= 2$ | $\geq 2$ | SFOS | $> 75$ | | - |

Nine signal regions are defined for the four-lepton search, which are classified in three groups by the number of light leptons and taus in an event (see table 4.3). The SR0x, SR1x and SR2x signal regions require at least four, exactly three or exactly two light leptons as well as zero or more, one or more or two or more taus, respectively. For ‘noZ’ signal regions a $Z$-veto against events containing at least one same-flavour opposite sign (SFOS) lepton pair ($e^+e^-$, $\mu^+\mu^-$) with an invariant mass $m_{\mathrm{SFOS}}$ in the range $|m_{\mathrm{SFOS}} - m_Z| < 10$ GeV is applied, because many background processes, like $ZZ$ production, are rich in leptonically decaying $Z$ bosons. Depending on the light lepton multiplicity requirement, also three- and four-lepton combinations, SFOS + $\ell$ and SFOS + SFOS, are vetoed to suppress radiative $Z$ decays ($Z \to \ell\ell\gamma$, $Z \to 4\ell$). The ‘noZ’ regions are split into ‘noZa’ and ‘noZb’ regions. The ‘noZa’ regions require high $E_{\mathrm{T}}^{\mathrm{miss}}$, while events in the ‘noZb’ regions must satisfy either a large $E_{\mathrm{T}}^{\mathrm{miss}}$ or a large ‘effective mass’ requirement. The effective mass $m_{\mathrm{eff}}$ of an event is defined as the scalar sum of the transverse momenta of all leptons, of jets with $p_{\mathrm{T}} > 40$ GeV and $E_{\mathrm{T}}^{\mathrm{miss}}$. On the other hand, the three ‘Z’ regions require at least one $Z$ boson candidate, i.e. a SFOS pair with an invariant mass $|m_{\mathrm{SFOS}} - m_Z| < 10$ GeV.

### 4.2.3 Background Estimation

The background processes are divided into two categories. Background processes leading to the same final states as the signal processes are referred to as irreducible background. In the case of the four-lepton analysis, the irreducible background events contain final states with four isolated leptons from $W$ and $Z$ boson decays. Reducible background events resemble signal events only due to imperfections in the reconstruction or due to misidentification of particles. The reducible background processes for the four-lepton analysis contain at least one 'fake' lepton originating from the semileptonic decay of a hadron, the misidentification of a light-flavour jet, or a photon conversion.

The main irreducible background processes are

- $ZZ$ and $Z\gamma^*$ production,
- $ZWW$ and $ZZZ$ production,
- $t\bar{t}+Z$ and $t+WZ$ production, and
- Standard Model Higgs boson decays to $ZZ^*$ or Higgs boson production in association with a $Z$ boson or a $t\bar{t}$ pair

while the principal reducible background contributions arise from

- $t\bar{t}$ production,
- $Z+$jets and $Z+\gamma$ production,
- $WZ+$jets and $WZ+\gamma$ production.

Which background processes dominate depends on the signal regions. In the case of light lepton final states, $t\bar{t}+Z$ is the dominant process, whereas for signal regions involving taus the reducible component is by far the largest one.

The amount of irreducible background is estimated with Monte Carlo simulations while the reducible background is determined from the data with the 'weighting method'. The weighting method is a data-driven technique using events with reconstructed leptons that fail one or more of the identification criteria. Such leptons are called 'loose', whereas leptons that fulfil all selection criteria are called 'tight'. The so called fake ratio $F = f/\bar{f}$ is defined, with the probabilities $f(\bar{f})$ that a fake lepton is a tight (loose) lepton. For each signal region, two data control regions CR1 and CR2 are defined. For CR1 three tight and one loose lepton and for CR2 two tight and two loose leptons are required. The number of reducible background events $N_{\mathrm{red}}^{\mathrm{SR}}$ in one of the signal regions is then estimated according to the equation

$$N_{\mathrm{red}}^{\mathrm{SR}} = \left[N_{\mathrm{data}}^{\mathrm{CR1}} - N_{\mathrm{irr}}^{\mathrm{CR1}}\right] \times F - \left[N_{\mathrm{data}}^{\mathrm{CR2}} - N_{\mathrm{irr}}^{\mathrm{CR2}}\right] \times F_1 \times F_2, \tag{4.1}$$

where the number of irreducible background events $N_{\mathrm{irr}}^{\mathrm{CR}}$ from simulation is subtracted from the number of data events $N_{\mathrm{data}}^{\mathrm{CR}}$ in each control region and multiplied with the fake ratios $F$ and $F_1$ and $F_2$ for each loose lepton to extrapolate from the control regions to the signal regions. The term for CR2 is subtracted to correct for double-counting of events with two fake leptons.

For the background estimation various systematic uncertainties are taken into account. There are two kinds of systematic uncertainties, those arising from experimental imperfections and those from theoretical calculations. The first type includes uncertainties in the energy scales and resolutions, the identification and trigger efficiencies and in the luminosity measurement as well as Monte Carlo statistical uncertainties. The latter are the dominant experimental uncertainties and are in the range of 20% to 30% depending on the background source. All other experimental uncertainties are below 6%. The theoretical uncertainties are usually much larger than the experimental uncertainties. They originate from cross-section calculations and the comparison of different Monte Carlo generators for the background processes. These uncertainties range from 5% for $ZZ/Z\gamma^*$ to up to 50% for $t+WZ$. The choice of Monte Carlo generators leads to uncertainties of 5-20% for $ZZ/Z\gamma^*$ and 30-40% for $t\bar{t}+Z$. In the ‘noZ’ regions, the relative uncertainties in the irreducible background are 30-50%, while in the ‘Z’ regions the uncertainties decrease to 15-25%. For the irreducible background the cross-section uncertainty is dominant. The relative uncertainties of the reducible backgrounds can be as high as 100% for signal regions without taus and 30-45% (35-50%) for signal regions with at least one (two) taus.

### 4.2.4 Results

Table 4.4 shows the results of the four-lepton analysis for all signal regions [130]. No significant excess has been observed. These results have been used to determine model-independent 95% confidence level (CL) upper limits $N_{\mathrm{BSM}}$ on the number of signal events beyond the Standard Model (BSM) background expectation. The expected upper limits $N_{\mathrm{BSM}}^{\mathrm{exp}}$ are derived from the Standard Model background estimations, while the observed upper

**Table 4.4:** The numbers of observed events and expected Standard Model background events for each signal region of the four-lepton search together with the observed and expected model-independent 95% CL upper limits $N_{\mathrm{BSM}}$ on the contribution of beyond the Standard Model (BSM) events. In the last column, the $p_0$ value for the background-only hypothesis is given (which is truncated if it is above 50%).

| | Data | SM background | $N_{\mathrm{BSM}}^{\mathrm{obs}}$ | $N_{\mathrm{BSM}}^{\mathrm{exp}}$ | $p_0$ |
|---|---|---|---|---|---|
| SR0noZa | 3 | $1.6 \pm 0.5$ | 5.9 | $4.4^{+1.6}_{-1.0}$ | 0.15 |
| SR1noZa | 4 | $4.6^{+1.3}_{-1.2}$ | 5.7 | $5.9^{+2.5}_{-1.5}$ | 0.50 |
| SR2noZa | 7 | $4.0^{+1.2}_{-1.3}$ | 9.2 | $6.1^{+2.5}_{-1.4}$ | 0.13 |
| SR0noZb | 1 | $1.4 \pm 0.4$ | 3.7 | $3.9 \pm 1.4$ | 0.50 |
| SR1noZb | 1 | $2.9^{+1.0}_{-0.9}$ | 3.5 | $4.7^{+1.9}_{-1.2}$ | 0.50 |
| SR2noZb | 6 | $3.0 \pm 1.0$ | 8.7 | $5.6^{+2.3}_{-1.3}$ | 0.10 |
| SR0Z | 7 | $5.6 \pm 1.4$ | 8.1 | $6.7^{+2.7}_{-1.6}$ | 0.29 |
| SR1Z | 3 | $2.5 \pm 0.6$ | 5.3 | $4.7^{+1.9}_{-1.1}$ | 0.34 |
| SR2Z | 1 | $1.8 \pm 0.5$ | 3.5 | $4.1^{+1.7}_{-0.8}$ | 0.50 |

limits $N_{\mathrm{BSM}}^{\mathrm{obs}}$ are obtained from data [132]. They can give a first impression of the sensitivity to new models by comparing them to the number of expected signal events in these models.

The results are interpreted in the context of various signal models. Only the simplified RPV gluino model shown in figure 4.2 is relevant for the studies in chapter 5. Therefore, only for this model the 95% CL limits in the gluino-neutralino mass plane are shown in figure 4.3. The same systematic uncertainties have been taken into account for the signal and for the irreducible background contributions.

Four different cases with $\lambda$ couplings were considered separately. LSP decays with $\lambda_{121}$ and $\lambda_{122}$ couplings lead to final states with light leptons, whereas $\lambda_{133}$ and $\lambda_{233}$ couplings give rise to tau leptons in the final state. Due to the lower tau reconstruction efficiency compared to light leptons (see section 3.3), the limits for the latter couplings are much weaker. In the case of light leptons, lower limits of at least 1350 GeV can be placed on the gluino mass[1] for LSP masses $m\left(\tilde{\chi}_1^0\right) > 0.2 \cdot m(\tilde{g})$. In the scenarios with tau leptons and

---

[1] For all mass limits cited the theoretically predicted cross-sections are reduced by one standard deviation of the theoretical uncertainty, a convention of the ATLAS and CMS experiments in order to set conservative limits.

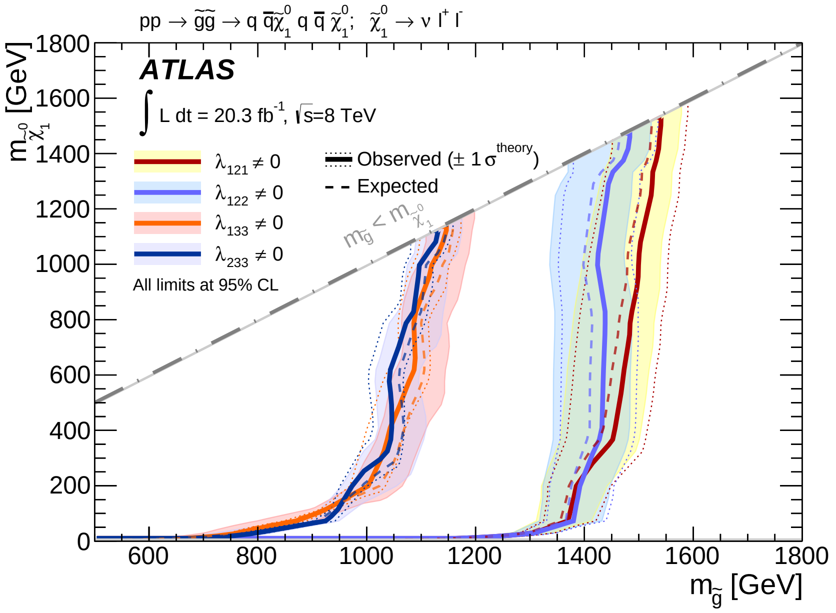

**Figure 4.3:** Observed (solid) and expected (dashed) 95% CL exclusion limits in the gluino-neutralino mass plane for the simplified RPV supersymmetric model of gluino pair production from the four-lepton search. The regions on the left side of the limit contours are excluded up to the dashed-dotted kinematical limit $m\left(\tilde{\chi}_1^0\right) = m\left(\tilde{g}\right)$ for this model. Limits for four independent choices of the dominant $\lambda$ couplings are given. The exclusion limits include all uncertainties except the theoretical signal cross-section uncertainty. The effect of the latter is indicated by the dotted lines on either side of the observed exclusion limit contours. The shaded bands around each expected exclusion limit curve show the $\pm 1\sigma$ uncertainties in the expectations [130].

near the kinematical limit $m\left(\tilde{\chi}_1^0\right) = m\left(\tilde{g}\right)$, gluino masses below 1080 GeV are excluded, while for smaller LSP masses $m\left(\tilde{\chi}_1^0\right) > 0.2 \cdot m\left(\tilde{g}\right)$, gluinos with masses less than 950 GeV are excluded. In all cases, the exclusion limits decrease strongly for LSP masses below $0.2 \cdot m\left(\tilde{g}\right)$ because the leptons from the LSP decays are then low energetic leading to a lower sensitivity. LSP decays corresponding to the remaining five $\lambda$ couplings lead to limits in between the two extreme cases. The intermediate scenarios are discussed in chapter 5.

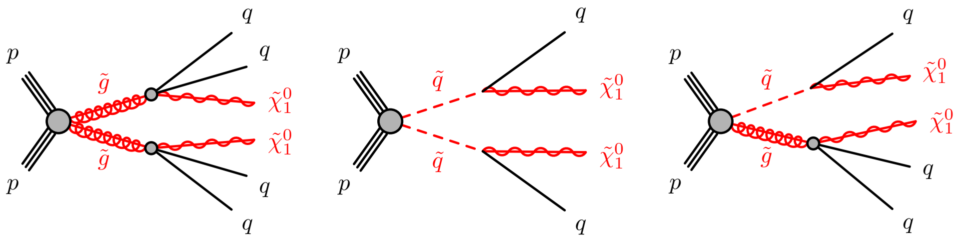

**Figure 4.4:** Diagrams of gluino and squark pair production in simplified RPC supersymmetric models considered in the zero-lepton search. All sparticles produced decay directly to the lightest neutralino (LSP) which is stable.

## 4.3 Zero-Lepton Search

### 4.3.1 Experimental Signatures

The zero-lepton search considers supersymmetric models with gluino and squark production leading to events with high-$p_\mathrm{T}$ jets, $E_\mathrm{T}^\mathrm{miss}$ and without light leptons. These final states are classified according to the minimum jet multiplicity, which has to be in the range of two to six. Events with light leptons are vetoed to avoid the overlap with other searches like in reference [125]. Hadronic tau decays are not reconstructed explicitly, but treated as jets. Only models with R-parity conservation and the neutralino as LSP are investigated leading to a high amount of $E_\mathrm{T}^\mathrm{miss}$.

The interpretations of this search include various simplified models where, for example, squarks and gluinos decay directly to the LSP as shown in figure 4.4 and the other sparticles are decoupled by setting their masses to 4.5 TeV. The gluinos decay to a quark, an anti-quark and a neutralino, whereas the squarks decay to their Standard Model partners and a neutralino. For squark production, only first and second generation squarks are considered. In addition to these simplified models, more detailed supersymmetric models with specific choices of parameters all leading to similar signatures are considered.

### 4.3.2 Event Selection and Signal Regions

The trigger selects events containing at least one jet with $p_\mathrm{T} > 80$ GeV and $E_\mathrm{T}^\mathrm{miss} > 100$ GeV. For the background estimation, single electron, muon and photon triggers requiring $p_\mathrm{T} >$ 24 GeV, 24 GeV and $p_\mathrm{T} > 120$ GeV, respectively, are used.

**Table 4.5:** Cuts in $p_T$ and $\eta$ of the final state leptons, photons and jets of the zero-lepton analysis

| Object | $p_T$ cut [GeV] | $\lvert\eta\rvert$ cut |
|---|---|---|
| jet | $> 20$ | $< 4.5$ |
| $b$-jet | $> 40$ | $< 2.5$ |
| $e$ | $> 10$ | $< 2.47$ |
| $\mu$ | $> 10$ | $< 2.4$ |
| $\gamma$ | $> 130$ | $< 1.37$ or $1.52 < \lvert\eta\rvert < 2.47$ |

Table 4.5 shows the cuts in $p_T$ and $\eta$ for the selection of electron, muon, photon, jet and $b$-jet candidates. For the identification of jets originating from $c$ and $b$ quarks, the MV1 algorithm is used with a nominal efficiency of 70% [114]. In addition to the standard $e$ and $\mu$ candidates defined in table 4.5, also high-purity candidates are selected with an increased $p_T$ cut at 25 GeV and isolation and impact parameter cuts. These high-purity leptons are used for the control regions to estimate the $W$ + jets and top quark background contributions. Photon candidates are only considered for the control regions to estimate the $Z$ + jets background and are required to be isolated and to fulfil electron rejection criteria. Jets with $\lvert\eta\rvert > 2.8$ are not considered further after $E_T^{\text{miss}}$ has been calculated. As in the four-lepton analysis, an overlap-removal procedure is applied to resolve ambiguities in the reconstruction of different objects. Jets close to electrons and photons are, thus, discarded, as well as electrons and muons close to jets.

Fifteen signal regions are defined according to the minimum jet multiplicity and the amount of background rejection. Supersymmetric particles are expected to have high masses. Therefore, the effective mass $m_{\text{eff}}$ is used to discriminate between signal and background. Two different $m_{\text{eff}}$ definitions are used that differ by the selection of the jets used in the calculation. If a signal region requires $N_j$ jets, $m_{\text{eff}}(N_j)$ is the scalar sum of the transverse momenta of the leading $N_j$ jets and the missing transverse energy. In contrast, all jets with $p_T > 40$ GeV are taken into account in the computation of $m_{\text{eff}}(\text{incl})$. Events with electrons or muons are rejected for all signal regions. The amount of background rejection ranges from very loose to very tight with mainly an increase of the $m_{\text{eff}}(\text{incl})$ cut. For example, the

**Table 4.6:** Requirements for the signal regions of the zero-lepton search with at least five jets (see text)

| Requirement | Signal Region | | | | |
|---|---|---|---|---|---|
| | 5j | 6jl | 6jm | 6jt | 6jt+ |
| $E_{\mathrm{T}}^{\mathrm{miss}}$ [GeV] | $> 160$ | | | | |
| $p_{\mathrm{T}}(j_1)$ [GeV] | $> 130$ | | | | |
| $p_{\mathrm{T}}(j_2)$ [GeV] | $> 60$ | | | | |
| $p_{\mathrm{T}}(j_3)$ [GeV] | $> 60$ | | | | |
| $p_{\mathrm{T}}(j_4)$ [GeV] | $> 60$ | | | | |
| $p_{\mathrm{T}}(j_5)$ [GeV] | $> 60$ | | | | |
| $p_{\mathrm{T}}(j_6)$ [GeV] | – | $> 60$ | | | |
| $\Delta\Phi(\mathrm{jet}_{1,2,3}, E_{\mathrm{T}}^{\mathrm{miss}})_{\mathrm{min}}$ | $> 0.4$ | | | | |
| $\Delta\Phi(\mathrm{jet}_{i>3}, E_{\mathrm{T}}^{\mathrm{miss}})_{\mathrm{min}}$ | $> 0.2$ | | | | |
| $E_{\mathrm{T}}^{\mathrm{miss}}/m_{\mathrm{eff}}(N_j)$ | $> 0.2$ | | | $> 0.25$ | $> 0.15$ |
| $m_{\mathrm{eff}}(\mathrm{incl})$ [GeV] | $> 1200$ | $> 900$ | $> 1200$ | $> 1500$ | $> 1700$ |

signal regions requiring at least six jets with loose, medium and tight background rejection are called SR6jl, SR6jm and SR6jt, respectively.

Another variable used for background discrimination is $\Delta\Phi(\mathrm{jet}, E_{\mathrm{T}}^{\mathrm{miss}})_{\mathrm{min}}$, the smallest azimuthal separation between $E_{\mathrm{T}}^{\mathrm{miss}}$ and any jet with $p_{\mathrm{T}} > 40$ GeV. Two cuts are used to suppress the QCD jet background in which mismeasurement of a jet energy generates fake missing transverse momentum along that jet direction, $\Delta\Phi(\mathrm{jet}_{1,2,3}, E_{\mathrm{T}}^{\mathrm{miss}})_{\mathrm{min}} > 0.4$ for the leading three jets and $\Delta\Phi(\mathrm{jet}_{i>3}, E_{\mathrm{T}}^{\mathrm{miss}})_{\mathrm{min}} > 0.2$ for all other jets. This background is further reduced by the cut on the ratio $E_{\mathrm{T}}^{\mathrm{miss}}/m_{\mathrm{eff}}(N_j)$. Table 4.6 summarises the different cuts for signal regions with at least five jets. All other signal regions were found to be irrelevant for the study in chapter 5. In the following discussion of the background estimation only these signal regions are considered.

**Table 4.7:** The four control regions CR of the zero-lepton search for the estimation of the different background processes in the signal region SR and their selection criteria and selected event types.

| CR | SR background | CR process | CR selection |
|---|---|---|---|
| CR$\gamma$ | $Z(\to \nu\nu)$+jets | $\gamma$+jets | Isolated photon, $p_{\mathrm{T}}(\gamma) > 130$ GeV |
| CRQ | Multi-jet | Multi-jet | Reversed SR requirements on $\Delta\Phi(\text{jet}, E_{\mathrm{T}}^{\mathrm{miss}})_{\min}$<br>and $E_{\mathrm{T}}^{\mathrm{miss}}/m_{\mathrm{eff}}(N_j)$ |
| CRW | $W(\to \ell\nu)$+jets | $W(\to \ell\nu)$+jets | $30\text{ GeV} < m_{\mathrm{T}}(\ell, E_{\mathrm{T}}^{\mathrm{miss}}) < 100\text{ GeV}$, $b$-jet veto |
| CRT | $t\bar{t}$ and single-$t$ | $t\bar{t} \to b\bar{b}qq'\ell\nu$ | $30\text{ GeV} < m_{\mathrm{T}}(\ell, E_{\mathrm{T}}^{\mathrm{miss}}) < 100\text{ GeV}$, $\geq 1 b$-jet |

### 4.3.3 Background Estimation

The dominant background processes for the zero-lepton search are $Z$ + jets, $W$ + jets, top quark pair, single top and multi-jet production. The $Z$ + jets background is primarily due to the irreducible component with $Z \to \nu\bar{\nu}$ decays where the neutrinos lead to significant $E_{\mathrm{T}}^{\mathrm{miss}}$. The $W$ + jets background arises mostly due to $W \to \tau\nu$ decays with subsequent hadronic tau decays. Since top quarks decay via $t \to bW$, the top quark pair background is largely due to semileptonic decays of one of the two $W$ bosons, $t\bar{t} \to b\bar{b}\ell\nu qq'$ and $t\bar{t} \to b\bar{b}\tau\nu qq'$, where the neutrino produces $E_{\mathrm{T}}^{\mathrm{miss}}$. Also, single top events (t-/s-channel and $Wt$ production) with the $W$ boson decaying leptonically are relevant. The multi-jet background is due to misreconstruction of jet energies in the calorimeters or semileptonic decays of heavy-flavour hadrons causing $E_{\mathrm{T}}^{\mathrm{miss}}$.

For the estimation of the background, four control regions (CR$\gamma$, CRQ, CRW and CRT) are defined for each signal region, each dedicated to different background sources (see table 4.7). The control regions inherit the $m_{\mathrm{eff}}$ cuts from the corresponding signal regions in most cases. This is required to allow for the extrapolation of the data in each control region to the signal region.

Table 4.7 lists the control region selections and the target background processes. The control region CR$\gamma$ is used to estimate the $Z(\to \nu\nu)$+jets background, based not on selected $Z(\to \nu\nu)$+jets events, but on $\gamma$+jets events with $p_{\mathrm{T}}(\gamma) > 130$ GeV where the photon $p_{\mathrm{T}}$ is added to the $E_{\mathrm{T}}^{\mathrm{miss}}$ to emulate the $E_{\mathrm{T}}^{\mathrm{miss}}$ from neutrinos of a $Z$ boson decay. Such $\gamma$+jets events have very similar kinematics as $Z(\rightarrow \nu\nu)$+jets events and the advantage of higher statistics. CRQ uses reversed requirements on $\Delta\Phi(\mathrm{jet}, E_{\mathrm{T}}^{\mathrm{miss}})_{\mathrm{min}}$ and $E_{\mathrm{T}}^{\mathrm{miss}}/m_{\mathrm{eff}}(N_j)$ with respect to the corresponding signal region to estimate the multi-jet background. The $W(\rightarrow \ell\nu)$+jets background is estimated from CRW and $t\bar{t}$ and single top quark background from selected semileptonic $t\bar{t}$ decays in CRT. CRW requires a veto against $b$-jets whereas CRT requires at least one $b$-jet. Both CRW and CRT require a high-purity lepton $\ell$, $E_{\mathrm{T}}^{\mathrm{miss}}$ and a transverse invariant mass[2] $m_{\mathrm{T}}(\ell, E_{\mathrm{T}}^{\mathrm{miss}})$ of the lepton-$E_{\mathrm{T}}^{\mathrm{miss}}$ system between 30 GeV and 100 GeV consistent with a $W$ boson decay. This lepton is treated as a jet in the selection criteria to model background events with hadronic tau decays. In addition, CRW and CRT do not require cuts on $\Delta\Phi(\mathrm{jet}, E_{\mathrm{T}}^{\mathrm{miss}})_{\mathrm{min}}$ and $E_{\mathrm{T}}^{\mathrm{miss}}/m_{\mathrm{eff}}(N_j)$ to increase the data sample size. In the case of SR6jt, both control regions require $m_{\mathrm{eff}} > 1300$ GeV instead of $> 1500$ GeV for the same reason.

The estimated background contribution $N_i(\mathrm{SR})$ to the signal region SR for the process $i$ is obtained by extrapolating the number of observed events $N_i^{\mathrm{data}}(\mathrm{CR})$ in the corresponding control region with a scale factor $s = \frac{N_i^{\mathrm{MC}}(\mathrm{SR})}{N_i^{\mathrm{MC}}(\mathrm{CR})}$ derived from Monte Carlo (MC) simulation according to the following relation:

$$N_i(\mathrm{SR}) = N_i^{\mathrm{data}}(\mathrm{CR}) \times \frac{N_i^{\mathrm{MC}}(\mathrm{SR})}{N_i^{\mathrm{MC}}(\mathrm{CR})}. \tag{4.2}$$

A primary source of the systematic error is the statistical uncertainty in the control region yields, in particular for CRT and CRW. Limited Monte Carlo statistics is relevant only in the case of SR6jt. Theoretical uncertainties in the background cross-section prediction are in general the second largest systematic error. Experimental uncertainties in the jet energy and $E_{\mathrm{T}}^{\mathrm{miss}}$ scales are only relevant for SR6jl. The total systematic uncertainty increases with the amount of background rejection: it is 10% for SR6jl while it is 33% for SR6jt+.

### 4.3.4 Results

Table 4.8 summarises the results of the zero-lepton analysis for $\sqrt{s} = 8$ TeV data. The background predictions are in very good agreement with the data. Therefore upper limits are

---

[2] The transverse mass of two particles (1, 2) produced in a two-body decay is given by $m_{\mathrm{T}} = \sqrt{(E_{\mathrm{T}}(1) + E_{\mathrm{T}}(2))^2 + (\vec{p}_{\mathrm{T}}(1) + \vec{p}_{\mathrm{T}}(2))^2}$. The mass $m$ of the parent particle is the endpoint of the transverse mass distribution: $m_{\mathrm{T}} \leq m$. For $W^{\pm} \rightarrow \ell^{\pm}\nu$, $\vec{p}_{\mathrm{T}}(\nu) = \vec{E}_{\mathrm{T}}^{\mathrm{miss}}$ is used.

**Table 4.8:** Overview of the zero-lepton results for signal regions requiring at least five jets. The Standard Model (SM) background estimations are shown together with the numbers of observed events. Based on these numbers, model-independent 95% CL upper limits $N_{\mathrm{BSM}}$ for beyond-Standard-Model (BSM) signal yields are given together with the $p_0$-value for the background-only hypothesis truncated at 50%.

| Signal region | 5j | 6jl | 6jm | 6jt | 6jt+ |
|---|---|---|---|---|---|
| | | | Background estimates | | |
| Diboson | $16 \pm 8$ | $9 \pm 4$ | $4 \pm 2$ | $1.6 \pm 0.8$ | $0.2 \pm 0.1$ |
| $Z/\gamma^*$+jets | $31 \pm 8$ | $9 \pm 4$ | $3 \pm 2$ | $0.6 \pm 0.6$ | $0.6^{+0.8}_{-0.6}$ |
| $W$+jets | $28 \pm 8$ | $15 \pm 7$ | $9 \pm 5$ | $1.2 \pm 0.9$ | $0.3^{+1.2}_{-0.3}$ |
| $t\bar{t}$(+EW) + single top | $51 \pm 9$ | $76 \pm 7$ | $16 \pm 4$ | $1.8 \pm 0.6$ | $3.7 \pm 1.7$ |
| Multi-jets | $1.0^{+2.6}_{-1.0}$ | $1.7^{+3.0}_{-1.7}$ | $0.4^{+0.8}_{-0.4}$ | $0.01^{+0.03}_{-0.01}$ | $0.3^{+0.4}_{-0.3}$ |
| Total | $126 \pm 13$ | $111 \pm 11$ | $33 \pm 6$ | $5.2 \pm 1.4$ | $4.9 \pm 1.6$ |
| Observed events | 121 | 121 | 39 | 5 | 6 |
| | | | 95% CL upper limits | | |
| $N^{\mathrm{obs}}_{\mathrm{BSM}}$ | 35 | 39 | 25 | 6.6 | 7.9 |
| $N^{\mathrm{exp}}_{\mathrm{BSM}}$ | $37^{+13}_{-10}$ | $31^{+12}_{-6}$ | $20^{+6}_{-4}$ | $6.2^{+2.6}_{-1.3}$ | $6.6^{+2.6}_{-1.6}$ |
| $p_0$ | 0.50 | 0.27 | 0.25 | 0.50 | 0.36 |

set on the beyond-Standard-Model signal yields and cross-sections. Figure 4.5 shows the interpretation of these results in simplified models with gluino and squark pair production (illustrated in figure 4.4) in terms of exclusion regions in the NLSP-neutralino mass plane. In the case of the gluino model with decoupled squarks (upper part of figure 4.5), gluino masses up to 1340 GeV are excluded at 95% CL for neutralino masses below 200 GeV. For neutralino masses in the range 250 to 500 GeV, the lower limit on the gluino mass lies between 1.0 and 1.1 TeV. No exclusion limits can be set for neutralino masses above 550 GeV.

The lower part of figure 4.5 shows lower limits on the squark mass for two models of pair production of first and second generation squarks where the gluino is decoupled. One model considers eight active squark states with degenerate masses, i.e. all states of the first two generations, the other model just one active squark state. Concerning the model with eight squarks, the excluded squark mass range reaches as high as 870 GeV (780 GeV) for neutralino masses below 100 GeV (300 GeV). No mass limits can be set for neutralinos heavier than 380 GeV. For the model with only one active squark state, the excluded squark mass range decreases to 440 GeV, while no constraint is possible for $m\left(\tilde{\chi}_1^0\right) > 140$ GeV.

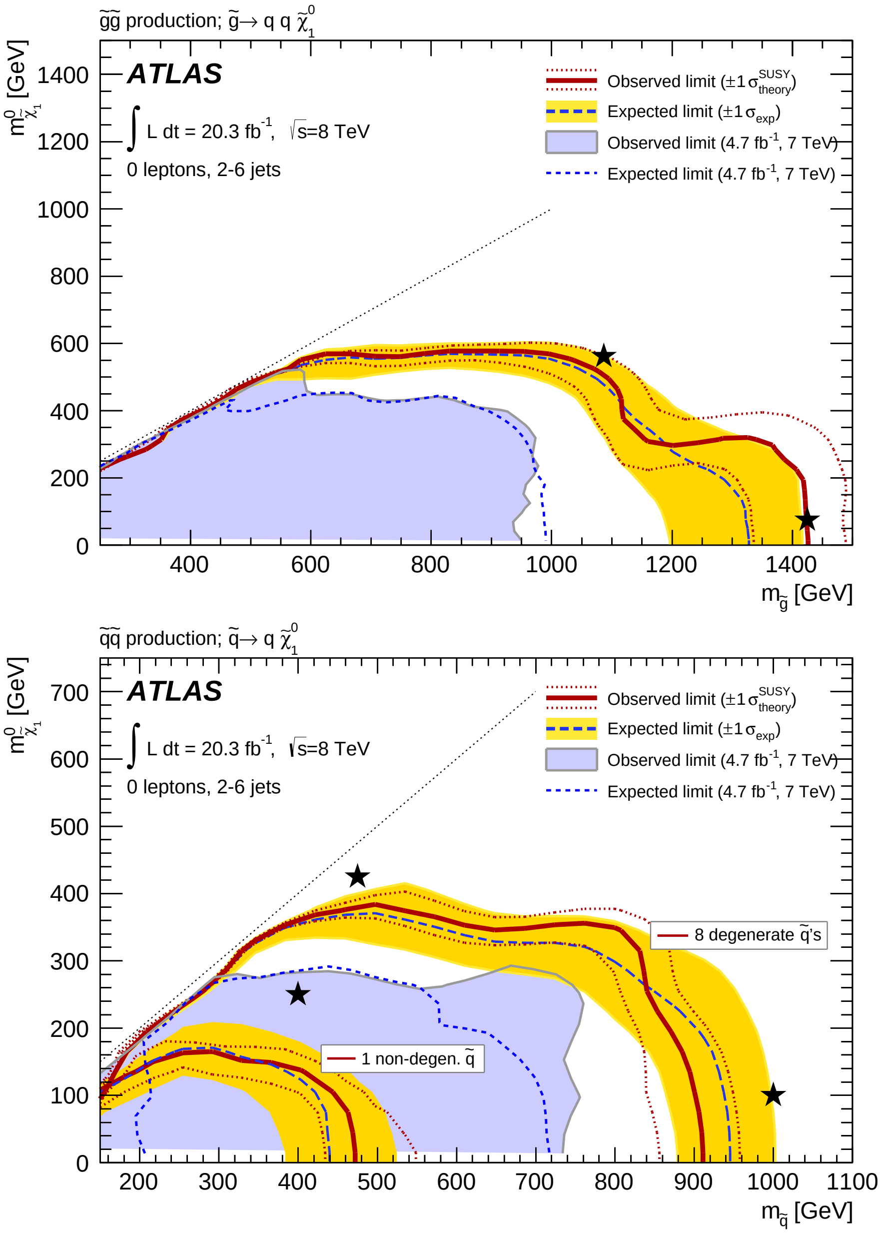

**Figure 4.5:** Observed (solid) and expected (dashed) 95% CL exclusion limits in the NLSP-neutralino mass plane for simplified models with gluino (top) and 1st and 2nd generation squark pair production (bottom) from the zero-lepton search. The yellow bands show the $\pm 1\sigma$ uncertainties in the expectations and the dotted contours indicate the theoretical uncertainties from cross-section calculations. The diagonal dashed line shows the kinematic limit for the models where $m(\tilde{g}) = m\left(\tilde{\chi}_1^0\right)$ or $m(\tilde{q}) = m\left(\tilde{\chi}_1^0\right)$. The black stars indicate benchmark models (see reference [122]).

# Chapter 5

# Reinterpretation of Searches in R-Parity Violating Supersymmetric Models

In this chapter, ATLAS searches for RPC and RPV supersymmetry (as they have been discussed in the previous chapter) are reinterpreted in the context of simplified RPV supersymmetric models. Only models with lepton-number-violating couplings are considered, since similar reinterpretations have already been performed for baryon-number-violating couplings in an ATLAS search for new massive particles decaying to multi-jet final states [133]. The bilinear couplings in equation (2.7) are not considered as their impact on neutrino masses make the construction of a simplified model more difficult [97]. Thus, the $\lambda$ and $\lambda'$ couplings in equation (2.7) remain, where the effect of $\lambda'$ couplings has not been investigated in the case of prompt LSP decays by any ATLAS search until now. Sparticle production via the strong interaction is considered, because the cross-sections are much larger compared to electroweak production for $\mathcal{O}(\text{TeV})$ sparticle masses. Regarding the $\lambda$ couplings, constraints have already been set on a model with gluino pair production by the four-lepton search discussed in section 4.2.4, but only for a small fraction of possible LSP decays. This interpretation is extended in this thesis in order to cover all possible signatures.

Chapter 5 is divided into three sections. In section 5.1, three simplified RPV supersymmetric models are introduced and discussed in detail with emphasis on the associated LSP decays. These models are studied without detector simulation in section 5.2, to find which ATLAS searches for supersymmetry are potentially sensitive to them. Model-dependent systematic uncertainties are also considered. In the last section 5.3, two sensitive searches are used to derive constraints on the three signal models, using a fast simulation of the ATLAS detector.

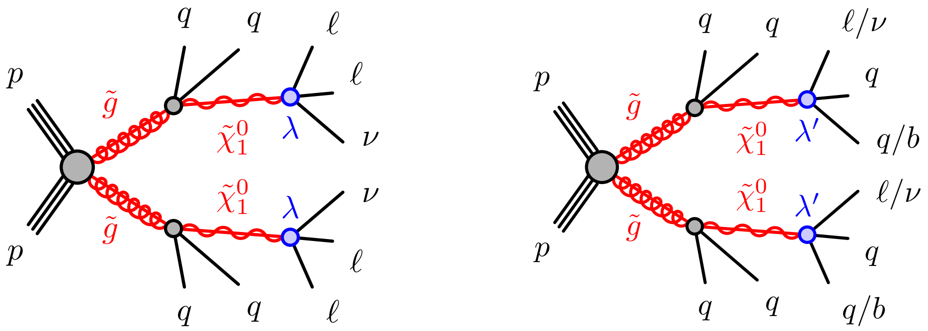

**(a)** Gluino model with $\lambda$ couplings

**(b)** Gluino model with $\lambda'$ couplings

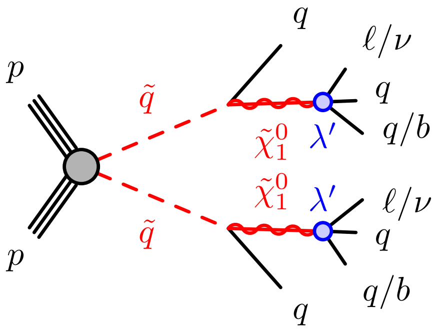

**(c)** Squark model with $\lambda'$ couplings

**Figure 5.1:** Diagrams of the production and decay processes of the three simplified RPV supersymmetric models with gluino and squark pair production studied in this thesis.

## 5.1 Production and Decay Modes

Three simplified models with RPV are investigated in this thesis. The production and decay modes are illustrated in figure 5.1. The supersymmetric particles are produced via the strong interaction and the LSP is a bino-like neutralino, i.e. it has no wino or higgsino components. In two of these models a pair of gluinos is produced, each of them decaying into a quark-anti-quark pair of the first or second generation and to a neutralino. In the third model, squarks are pair-produced and decay to their Standard Model partners and a neutralino. Only first and second generation squarks are included and are assumed to be degenerate in their masses. In the three models, all sparticles except the LSP and the next-to-lightest supersymmetric particle (NLSP) are decoupled at a mass scale of 4.5 TeV and cannot be pair-produced at a center-of-mass energy of 8 TeV. Third-generation (s)quarks are not produced in these models, because this would increase the sensitivity of the searches due to additional jets or leptons from top quark or $B$-hadron decays in the final state. More conservative limits are obtained by neglecting them.

Since R-parity is violated in these models, the LSP decays to Standard Model particles. The decays are assumed to be prompt with an LSP lifetime so short that the decay vertex and the primary interaction vertex cannot be resolved. In one of the gluino models the LSP decays via $\lambda$ couplings whereas in the other two models the LSP decays via $\lambda'$ couplings. In contrast to the interpretations of the four-lepton search discussed in section 4.2.1, the assumption of a single dominant coupling is given up and the LSP can decay via multiple couplings.

A squark model with $\lambda$ couplings has not been considered, because the four-lepton search is expected to have a very similar sensitivity to both squark and gluino production. This is due to the fact that the four-lepton search does not require any jets in the final state and, thus, its sensitivity does not depend on the number of jets produced in the NLSP decays.

### 5.1.1 LLE Decays

Neutralino decays mediated by $\lambda$ couplings are described by the superpotential term

$$\frac{1}{2}\lambda_{ijk}L_iL_j\overline{E}_k \tag{5.1}$$

from equation (2.7). According to table 2.1, the neutralino decays into a left-handed charged lepton $l_{i/j}$, a right-handed charged lepton $l_k$ and a neutrino $\nu_{j/i}$: $\tilde{\chi}_1^0 \to l_{i/j}l_k\nu_{j/i}$. In each event two LSPs are produced and, therefore, an event contains four leptons and two neutrinos. In the following, the three neutrino flavours are not differentiated as neutrinos escape undetected leading to $E_{\mathrm{T}}^{\mathrm{miss}}$.

The experimental signatures do not depend on the initial chirality of the leptons, and thus, left- and right-handed leptons cannot be distinguished. But the decay rates of the LSP into leptons depend on their chirality. This is due to the fact that the $SU(2)_L$ doublets $L$ participating in the interactions contain neutrinos as well as charged leptons while the $SU(2)_L$ singlets $E$ contain only charged leptons. In LSP decays mediated by a single $\lambda$ coupling with $k = 1$, therefore, always a right-handed electron is produced, while for $i = 1$ or $j = 1$ either an electron or an electron-neutrino is produced.

The branching ratios for LSP decays into a left-handed charged lepton or neutrino depend on the masses of the corresponding superpartners, because the decays are mediated by virtual sparticles (see figure 2.7). In this thesis, the same assumptions are made as in the four-lepton analysis [130], namely that $\mathrm{BR}\left(\tilde{\chi}_1^0 \to l_i\right) = \mathrm{BR}\left(\tilde{\chi}_1^0 \to \nu_i\right)$ leading to a maximal branching ratio of the LSP decay to a particular left-handed lepton $i = e$, $\mu$, $\tau$ of 50%. For a particular right-handed charged lepton the largest possible branching ratio is 100%. Since a left- and a right-handed charged lepton are always produced in the LSP decay, the sum of the branching ratios is 100% for each chirality separately.

Neutralino decays mediated by $\lambda$ couplings lead to six experimentally distinguishable decay modes that can be classified according to the lepton flavours involved:

- Two light leptons: $\tilde{\chi}_1^0 \to ee\nu$, $e\mu\nu$, $\mu\mu\nu$.
- One tau and one light lepton: $\tilde{\chi}_1^0 \to e\tau\nu$, $\mu\tau\nu$.
- Two taus: $\tilde{\chi}_1^0 \to \tau\tau\nu$.

In the gluino model with $\lambda$ couplings, all of these decay modes are allowed. The results of the four-lepton analysis indicate that the sensitivity to decay channels with electrons and muons is similar (see figure 4.3, for example). The sensitivity to final states with taus is much weaker due to the relatively low reconstruction efficiency of hadronically decaying taus. To reduce the vanity of the models to be considered, the branching ratios of the LSP decay to electrons and muons are therefore assumed to be equal. Only three distinct LSP decay modes then have to be considered: $\ell\ell\nu$, $\ell\tau\nu$ and $\tau\tau\nu$, where $\ell$ refers to electrons and muons with equal probability.

Under these assumptions, the parameter space of the LSP decay shown in figure 5.2 is two-dimensional. An LSP decay is defined by its branching ratios to left-handed ($y$-axis) and right-handed ($x$-axis) taus. The branching ratios to electrons and muons are given by $\mathrm{BR}\left(\tilde{\chi}_1^0 \to e_{L/R}\right) = \mathrm{BR}\left(\tilde{\chi}_1^0 \to \mu_{L/R}\right) = \frac{1}{2} \cdot \left(1 - \mathrm{BR}\left(\tilde{\chi}_1^0 \to \tau_{L/R}\right)\right)$. At the four corners of figure 5.2, the LSP decays via specific couplings (e.g. $\lambda_{121}$, $\lambda_{122}$ at the origin), which lead to either one or two possible decay modes. If two decay modes are allowed, then they are assumed to have equal branching ratio of 50%.

The branching ratios for the three decay modes can be derived as a function of $\mathrm{BR}\left(\tilde{\chi}_1^0 \to \tau_R\right) = x$ and $\mathrm{BR}\left(\tilde{\chi}_1^0 \to \tau_L\right) = y$ by using the boundary conditions at the four corners of figure 5.2. With the assumptions above, one obtains the following boundary conditions

- $\mathrm{BR}_{\ell\ell\nu}(0,0) = 1$, $\mathrm{BR}_{\ell\ell\nu}(1,0) = \mathrm{BR}_{\ell\ell\nu}(1,0.5) = 0$ and $\mathrm{BR}_{\ell\ell\nu}(0,0.5) = 0.5$ for the decay mode $\ell\ell\nu$,

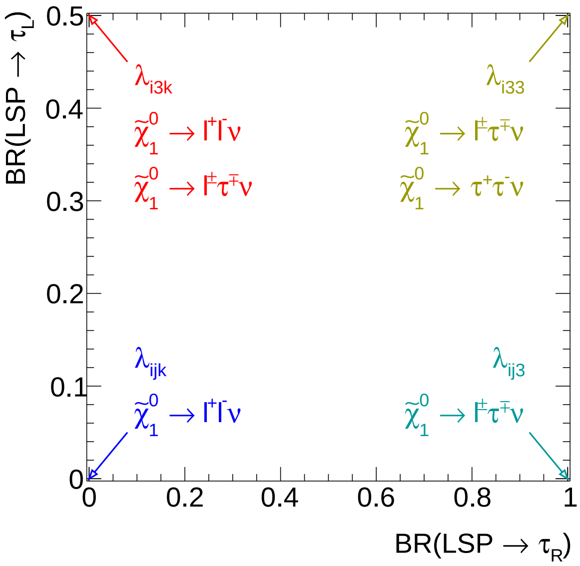

**Figure 5.2:** Two-dimensional scan of the branching ratios of RPV LSP decays in the case of $\lambda$ couplings. In each corner of the plot the corresponding decay modes are indicated with $i$, $j$ and $k = 1,2$. There are only nine different $\lambda$ couplings which are commonly denoted by $\lambda_{12k}$, $\lambda_{13k}$ and $\lambda_{23k}$ with $k = 1,2,3$. In this plot, $l$ refers only to electrons and muons.

- $\mathrm{BR}_{\ell\tau\nu}(0,0) = 0$, $\mathrm{BR}_{\ell\tau\nu}(1,0) = 1$ and $\mathrm{BR}_{\ell\tau\nu}(0,0.5) = \mathrm{BR}_{\ell\tau\nu}(1,0.5) = 0.5$ for the decay mode $\ell\tau\nu$ and
- $\mathrm{BR}_{\tau\tau\nu}(0,0) = \mathrm{BR}_{\tau\tau\nu}(1,0) = \mathrm{BR}_{\tau\tau\nu}(0,0.5) = 0$ and $\mathrm{BR}_{\tau\tau\nu}(1,0.5) = 0.5$ for the decay mode $\tau\tau\nu$.

The general branching ratios are then given by the interpolation formula

$$\begin{aligned}\mathrm{BR}_i(x,y) = 2\,[&(1-x)\cdot(0.5-y)\cdot\mathrm{BR}_i(0,0) + x\cdot(0.5-y)\cdot\mathrm{BR}_i(1,0)\\ &+(1-x)\cdot y\cdot\mathrm{BR}_i(0,0.5) + x\cdot y\cdot\mathrm{BR}_i(1,0.5)]\,.\end{aligned} \tag{5.2}$$

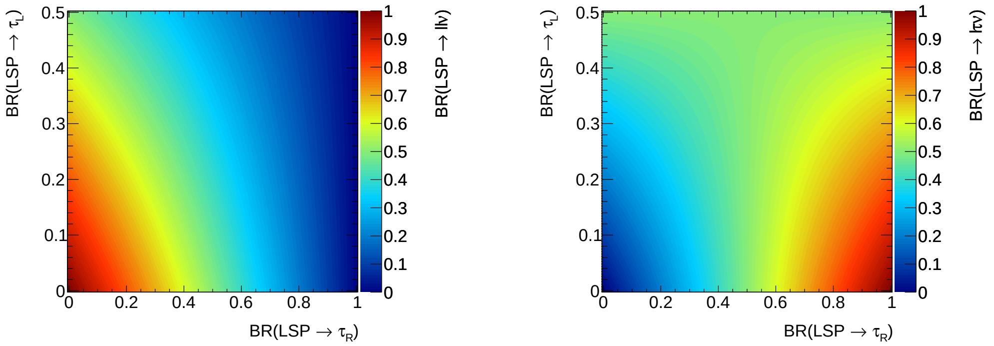

**(a)** $\ell\ell\nu$ **(b)** $\ell\tau\nu$

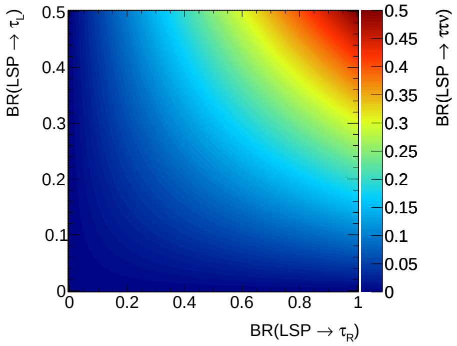

**(c)** $\tau\tau\nu$

**Figure 5.3:** Branching ratios of the three LSP decay modes in the case of $\lambda$ couplings in the plane illustrated in figure 5.2.

With the boundary conditions, the following expressions are obtained for the three decay modes:

$$\mathrm{BR}_{\ell\ell\nu}(x,y) = (1-x)\cdot(1-y)\,, \tag{5.3}$$

$$\mathrm{BR}_{\ell\tau\nu}(x,y) = y + x\cdot(1-2y)\,, \tag{5.4}$$

$$\mathrm{BR}_{\tau\tau\nu}(x,y) = x\cdot y. \tag{5.5}$$

They are illustrated in figure 5.3. The sum of the three branching ratios is 1 for all points in the square by construction.

To further illustrate the final states of the model, figure 5.4 shows the average numbers of either light charged leptons $\ell$ or taus originating from the two LSPs in an event. The

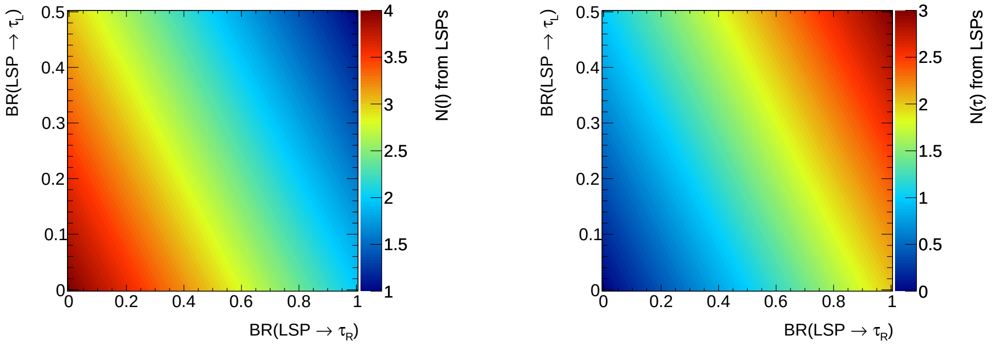

**(a)** $e$, $\mu$

**(b)** $\tau$

**Figure 5.4:** Average number of (a) light charged leptons and (b) taus originating from the decays of the two LSPs in an event in the gluino model with $\lambda$ couplings.

maximum number of four light leptons per event is achieved only at the origin. But even in the upper right corner there is still on average one light lepton per event from the LSP decays. The number of taus per event is $N(\tau) = 4 - N(\ell)$ and therefore shows the opposite trend. Figure 5.4a only accounts for light leptons originating directly from the LSP decay. Additional light leptons are produced in tau decays with $\mathrm{BR}\left(\tau^- \to \ell^- \bar{\nu}_\ell \nu_\tau\right) = 35\%$ [20]. The average numbers of light leptons in an event originating from taus are shown in figure 5.5a. Figure 5.5b shows the sum of both contributions to the light lepton yield. Across the entire square there are on average more than two light leptons per event, which clearly singles out these processes over the Standard Model background both for the trigger and event selection.

For the scan of the tau branching ratio $(x,y)$ range of the LSPs in figure 5.2, each $\tilde{\chi}_1^0$ decaying in a Monte Carlo generated event with branching ratio $\mathrm{BR}_{i\mathrm{gen}}$ into a final state $i = \ell\ell\nu$, $\ell\tau\nu$, $\tau\tau\nu$ is assigned a weight depending on the position $(x,y)$. The weight $w_{i\mathrm{LSP}}(x,y)$ is the branching ratio corresponding to the point $(x,y)$ relative to the generated branching ratio for the given decay mode $i$:

$$w_{i\mathrm{LSP}}(x,y) = \frac{\mathrm{BR}_i(x,y)}{\mathrm{BR}_{i\mathrm{gen}}}. \tag{5.6}$$

The event weight is the product of the weights of the two LSPs:

$$w(x,y) = w_{i\mathrm{LSP1}}(x,y) \cdot w_{j\mathrm{LSP2}}(x,y). \tag{5.7}$$

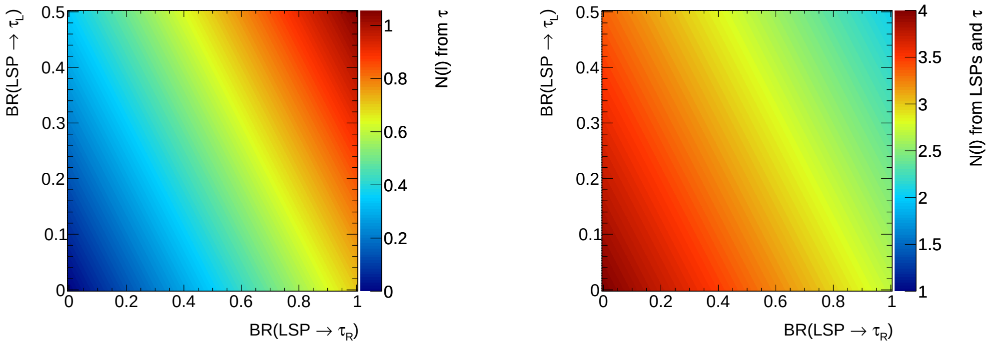

**(a)** $e$, $\mu$ from $\tau$ decays

**(b)** All $e$, $\mu$

**Figure 5.5:** Average number of light charged leptons per event originating (a) from tau decays and (b) from all sources in the gluino model with $\lambda$ couplings.

This event weight is used to reweight the Monte Carlo events in order to emulate the different branching ratio hypotheses.

### 5.1.2 LQD Decays

LSP decays mediated by $\lambda'$ couplings in the gluino and squark models are described by the superpotential term

$$\lambda'_{ijk} L_i Q_j \overline{D}_k. \tag{5.8}$$

According to table 2.1, one lepton and two quarks are produced in such neutralino decays: $\tilde{\chi}_1^0 \rightarrow l_i u_j d_k$ or $\tilde{\chi}_1^0 \rightarrow \nu_i d_j d_k$, where $u$ and $d$ stand for up- and down-type quarks, respectively, and $i$, $j$, $k = 1,2,3$ denote the fermion generations. Consequently, the decays of the two LSPs in an event produce up to two charged leptons $l_i$, four quarks and up to two neutrinos.

Regarding the index $i$, the same assumptions have been made as in the case of the $\lambda$ couplings in section 5.1.1, i.a. electrons and muons are produced with the same probability. The possible range of the branching ratio of the LSP decay to a tau is scanned up to a maximum value of 50% because the tau is left-handed. The remaining 50% of the decays involve a neutrino.

Jets formed by first- and second-generation quarks in general cannot be distinguished in the detector. Therefore, couplings with $j = 2$ or $k = 2$ are not considered, since the experimental signatures are similar to the $j = 1$ and $k = 1$ cases. The $D$ supermultiplet contains only down-type quarks and, thus, the LSP always decays to a bottom quark for

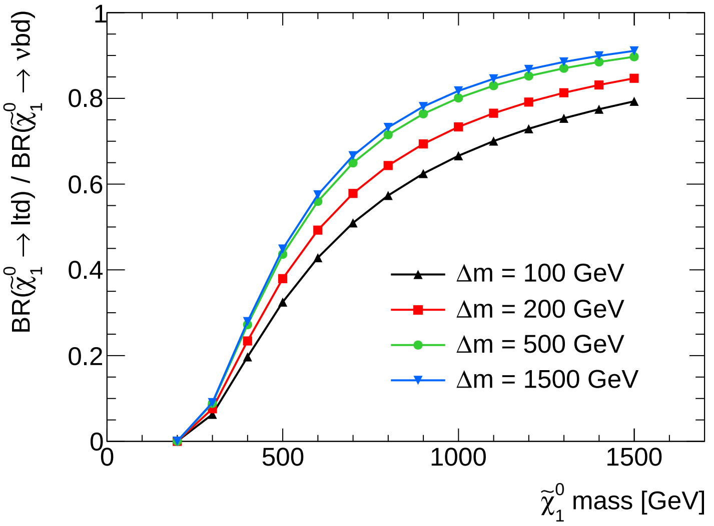

**Figure 5.6:** The ratio of the branching ratios of LSP decays into top and bottom quarks as a function of the $\tilde{\chi}_1^0$ mass in the pMSSM for different values of $\Delta m = m_{q3} - M_1$ (see text). All supersymmetric particles except $\tilde{\chi}_1^0$, $\tilde{b}_L$ and $\tilde{t}_L$ are decoupled with masses of 4.5 TeV.

$k = 3$, which is right-handed. Therefore, the largest possible branching ratio to a (right-handed) bottom quark is 100%. This is analogous to the $k = 3$ case for the $\lambda$ couplings where a right-handed tau is produced.

On the other hand, the supermultiplet $Q$ contains both up- and down-type (left-handed) quarks leading to the same situation as for the left-handed leptons. For $j = 1$ it is assumed that the branching ratios to up and down quarks are equal because of isospin symmetry and, consequently, $\mathrm{BR}\left(\tilde{\chi}_1^0 \to l_i u_j d_k\right) = \mathrm{BR}\left(\tilde{\chi}_1^0 \to \nu_i d_j d_k\right)$. For $j = 3$, i.e. the decays $\tilde{\chi}_1^0 \to l_i t d_k$ and $\tilde{\chi}_1^0 \to \nu_i b d_k$, this relation does not hold, because the bottom quark is much lighter than the top quark and thus the LSP decay to a bottom quark has a larger phase space. The effect has been studied with the ISAJET simulation program [134]. The results for the ratio of the branching ratios of $\tilde{\chi}_1^0$ decays to $t$ and $b$ quarks are shown in figure 5.6, calculated for $\lambda'_{i31}$ decays in the phenomenological MSSM (pMSSM) [135]. For $m\left(\tilde{\chi}_1^0\right) = 200$ GeV, close to the top mass, the ratio is zero, i.e. the decay to top quarks is fully suppressed. Above 200 GeV, the ratio increases rapidly, but the two decay rates are still not equal even for $m\left(\tilde{\chi}_1^0\right) = 1.5$ TeV. In addition, $\mathrm{BR}\left(\tilde{\chi}_1^0 \to l_i t d_k\right)$ and $\mathrm{BR}\left(\tilde{\chi}_1^0 \to \nu_i b d_k\right)$ depend on the masses of stop and sbottom, respectively, which are exchanged as intermediate virtual particles in the decays, analogous to figure 2.7. The latter effect is also shown in figure 5.6 in

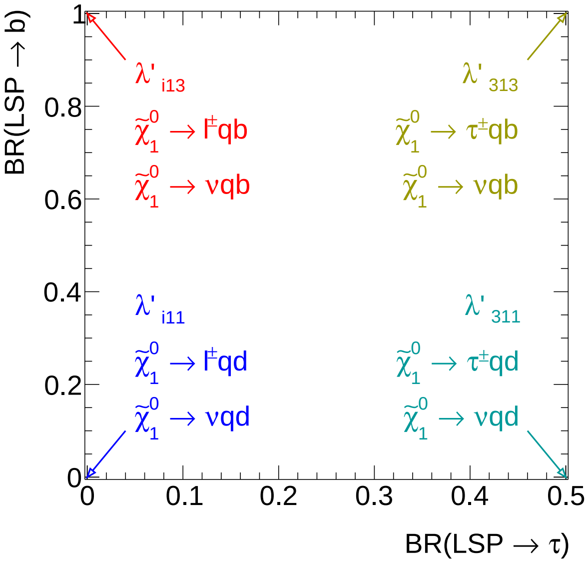

**Figure 5.7:** Two-dimensional scan of the branching ratios of RPV LSP decays in the case of $\lambda'$ couplings. In each corner the corresponding decay modes are indicated with $i = 1, 2$. In this plot, $l$ refers only to electrons and muons.

the dependence on $\Delta m = m_{q3} - M_1$ where $m_{q3}$ and $M_1$ are the masses of the third-generation left-handed squarks and of the bino at the GUT scale, respectively. It is difficult to fully account for the mass difference effects in a simplified model. Therefore, LSP decays to left-handed third-generation quarks are neglected in these models.

In conclusion, six $\lambda'_{i1k}$ couplings ($i = 1, 2, 3$, $j = 1$ and $k = 1, 3$) are considered for each of the two LQD models. The six experimentally distinguishable decay modes that result are: $\ell qd$, $\nu qd$, $\tau qd$, $\ell qb$, $\nu qb$ and $\tau qb$, where $\ell = e$ or $\mu$ and $q = u$ or $d$.

The two-dimensional parameter space used to describe the LSP branching ratios for the models with $\lambda'$ couplings is illustrated in figure 5.7. The $x$-axis denotes the branching ratio to a left-handed tau which is $\leq 50\%$ as discussed above. The $y$-axis denotes the branching ratio to a right-handed bottom quark which ranges up to $100\%$. In the same way as in figure 5.2, the LSP decays via specific couplings leading to two decay modes each with a branching ratio of $50\%$ at each of the four corners of the square. With interpolation functions analogous to equation 5.2, the following branching ratio functions are obtained for the six different LSP decay modes with $\lambda'$ couplings

$$\mathrm{BR}_{\ell qd}(x,y) = \frac{1}{2}\cdot(1-2x)\cdot(1-y)\,, \tag{5.9}$$

$$\mathrm{BR}_{\tau qd}(x,y) = x\cdot(1-y)\,, \tag{5.10}$$

$$\mathrm{BR}_{\nu qd}(x,y) = \frac{1}{2}\cdot(1-y)\,, \tag{5.11}$$

$$\mathrm{BR}_{\ell qb}(x,y) = \frac{1}{2}\cdot(1-2x)\cdot y, \tag{5.12}$$

$$\mathrm{BR}_{\tau qb}(x,y) = x\cdot y, \tag{5.13}$$

$$\mathrm{BR}_{\nu qb}(x,y) = \frac{1}{2}\cdot y. \tag{5.14}$$

The first three functions are shown in figure 5.8. The remaining three functions are simply the mirror images of the thirst three with respect to the line $\mathrm{BR}\left(\tilde{\chi}_1^0 \to b\right) = 0.5$. Each Monte Carlo event is reweighted using these six branching ratio functions according to equations (5.6) and (5.7).

### 5.1.3 Simulated Mass Grids

The generator Herwig++ [136] is used for all signal event generation. Signal samples are generated for three specific values of the mass ratio $r = m(\mathrm{LSP})/m(\mathrm{NLSP})$ of 0.1, 0.5 and 0.9. In the simplified models studied, the NLSP is either a gluino or a squark. The value of $r$ determines how the energy of the NLSP decay is distributed over the decay products. For $r = 0.9$, the decay products of the LSP are relatively energetic and the jets from the NLSP decay soft, whereas for $r = 0.1$ the opposite is the case. The masses of the supersymmetric particles used are given in table 5.1. Each combination of NLSP-LSP masses (e.g. $m(\tilde{g}) = 800$ GeV, $m\left(\tilde{\chi}_1^0\right) = 80$ GeV, later labelled as [800, 80]) is referred to as a ‘mass point’ in the NLSP-LSP mass grid.

The chosen ranges of gluino or squark masses and numbers of simulated events are based on the truth-level studies described in section 5.2. The number of events for each mass point was chosen such that at least 100 Monte Carlo events pass the criteria for at least one of the sensitive signal regions for every branching ratio hypothesis in most cases. For very low acceptances this requirement was reduced to 10 events.

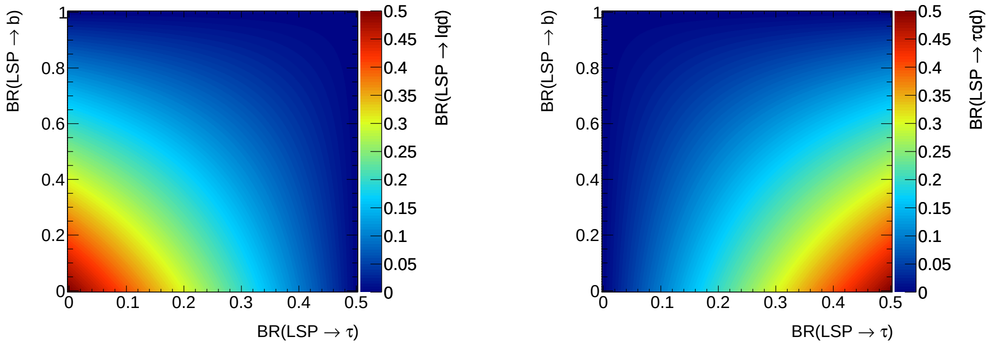

**(a)** $\ell qd$

**(b)** $\tau qd$

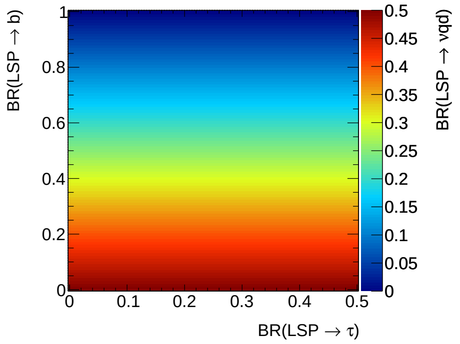

**(c)** $\nu qd$

**Figure 5.8:** Branching ratios of the three LSP decay modes without $b$-quarks in the case of $\lambda'$ couplings in the scheme of figure 5.7. The branching ratio functions for the three LSP decay modes with $b$-quarks are the mirror images with respect to the line $\mathrm{BR}\left(\tilde{\chi}_1^0 \to b\right) = 0.5$.

For each model, all combinations of decay modes of the two LSPs in an event were simulated, with equal branching ratios to electrons and muons, there will also be events with decays like $\tilde{\chi}_1^0\tilde{\chi}_1^0 \to e\tau\nu\mu\tau\nu$ which are not possible with a single dominant RPV coupling.

As the generated events are reweighted to scan the full range of LSP branching ratios, the originally simulated branching ratio can be freely chosen for each decay mode. In the case of the model with $\lambda$ couplings, the decay rates to final states with taus are artificially enhanced to compensate for the lower tau reconstruction efficiency. The model was simulated with $\mathrm{BR}(\ell\ell\nu) = 20\%$ and $\mathrm{BR}(\ell\tau\nu) = \mathrm{BR}(\tau\tau\nu) = 40\%$. This enhancement was not necessary for the models with $\lambda'$ couplings, because the sensitive analyses do not reconstruct taus explicitly but treat them as jets. Therefore, each of the six experimentally distinct decay modes was simulated with the same branching ratio of $1/6$.

### 5.1.4 Signal Cross-Sections

Signal cross-sections are calculated in general to next-to-leading order (NLO) in the strong coupling constant with resummation of soft gluon emission at next-to-leading logarithmic

**Table 5.1:** Numbers of simulated events (in thousands) for selected NLSP-LSP mass combinations in the three signal models

| | | Number of events | | |
|---|---|---|---|---|
| NLSP mass [GeV] | LSP mass [GeV] | Gluino - $\lambda$ | Gluino - $\lambda'$ | Squark - $\lambda'$ |
| 600 | 60 | - | 200 | 900 |
| 600 | 300 | - | - | 100 |
| 800 | 80 | 100 | 100 | 300 |
| 800 | 400 | - | 100 | 100 |
| 800 | 720 | - | 100 | 100 |
| 1000 | 100 | 100 | 100 | 100 |
| 1000 | 500 | 100 | 100 | 50 |
| 1000 | 900 | 100 | 100 | 50 |
| 1200 | 120 | 100 | 100 | - |
| 1200 | 600 | 100 | 100 | 50 |
| 1200 | 1080 | 100 | 100 | 50 |
| 1400 | 140 | 100 | 100 | - |
| 1400 | 700 | 100 | 100 | - |
| 1400 | 1260 | 100 | 100 | - |
| 1600 | 160 | 100 | - | - |
| 1600 | 800 | 100 | - | - |
| 1600 | 1440 | 100 | - | - |

**Table 5.2:** Cross-sections for gluino-gluino (NLO+NLL), squark-squark (NLO) and squark-antisquark (NLO+NLL) production from [137–141]

| NLSP mass [GeV] | $\sigma(\tilde{g}\tilde{g})$ [fb] | $\sigma(\tilde{q}\tilde{q}^{'})$ [fb] | $\sigma(\tilde{q}\bar{\tilde{q}})$ [fb] |
|---|---|---|---|
| 600 | $1282 \pm 225$ | $84 \pm 11$ | $201 \pm 33$ |
| 800 | $150 \pm 32$ | $23 \pm 2$ | $24 \pm 5$ |
| 1000 | $23 \pm 6$ | $7.7 \pm 0.8$ | $3.5 \pm 1.0$ |
| 1200 | $3.9 \pm 1.4$ | $2.6 \pm 0.4$ | $0.6 \pm 0.2$ |
| 1400 | $0.7 \pm 0.3$ | - | - |
| 1600 | $0.2 \pm 0.1$ | - | - |

(NLL) accuracy [137–141]. The nominal cross-section and the uncertainty are determined from an interval of cross-section predictions using different sets of parton distributions functions (PDF) and factorisation and renormalisation scales as described in reference [142]. The factorisation scale separates perturbative and non-perturbative QCD regimes, while renormalised coupling strengths for the processes considered are calculated at the renormalisation scale.

Table 5.2 shows the cross-section predictions and their uncertainties for the relevant supersymmetric production processes and masses. There are two possible production processes for squarks in which either a squark-antisquark ($\tilde{q}\bar{\tilde{q}}$) pair or two squarks ($\tilde{q}\tilde{q}'$) are produced. The cross-sections of both processes depend on the gluino mass. This dependence has been studied with the result that the cross-section decreases rapidly with increasing gluino mass. Therefore, a gluino mass of 4.5 TeV was chosen in order to obtain conservative limits. In the calculations of the signal yields the contributions from these two processes are added.

The cross-section for squark-squark production has a relative uncertainty of about 10-14%, which is nearly independent of the squark mass. This is due to the fact that this process can proceed at leading order only via a $t$-channel exchange of a gluino. The resummation of soft gluon emission at NLL order is not taken into account for this process. In contrast, gluino-gluino and squark-antisquark production are both dominated by $s$-channel gluon exchange and have large relative uncertainties growing with the NLSP mass which are related to uncertainties in the gluon PDF.

## 5.2 Truth-Level Monte Carlo Studies

Before simulating the three supersymmetric models in detail, a ‘truth-level’ simulation study without detector simulation was performed to assess the sensitivity of different existing ATLAS searches. At truth-level the reconstruction algorithms described in section 3.3 are not applied and different event selection criteria compared to reconstructed event samples are used. All particles produced in the collision except muons and neutrinos are used to form jets. As in the event reconstruction, the anti-$k_t$ algorithm is used with a distance parameter of $R = 0.4$. If a jet contains a $b$-quark and fulfils the kinematic criteria of an event selection, it is considered a $b$-jet.

Leptons selected in supersymmetry searches are usually isolated from hadronic activity. Therefore, truth-level charged leptons are required to originate either from supersymmetric particles or from $W$, $Z$ or Higgs boson decays. Electrons and muons from leptonically decaying taus are also taken into account. In the case of hadronically decaying taus, only the visible decay products are used to calculate their $p_{\mathrm{T}}$, as it is the case on reconstruction level in ATLAS. The same kinematic selection criteria as for reconstructed events are applied to the truth-level charged leptons except the isolation requirements. $E_{\mathrm{T}}^{\mathrm{miss}}$ is defined as the sum of the transverse momenta of the neutrinos in the event. All other steps of the event selection including the overlap removal remain unchanged. The fraction of events passing the selection requirements at truth-level is called acceptance. The number of signal events is given by $N = A \cdot \sigma \cdot L$, where $\sigma$ is the cross-section for the process and $L$ the integrated luminosity.

Truth-level studies have been performed for the three RPV signal models and all the ATLAS searches in table 4.1. Only for seven of these searches did events pass the selection criteria, namely for the four-lepton, the same-sign/three-lepton, the three-lepton, the one-lepton, the zero-lepton, the multijet and the stop $Z$ search. Studies of the electroweak three-lepton and the stop $Z$ search results revealed that these searches cannot constrain the signal models, because the expected signal yields are too far below the model-independent upper limits on non-Standard-Model event production. The reason for this is that the three-lepton search is optimised for electroweak production processes, while the three signal models are based on strong production. The stop $Z$ search requires SFOS lepton pairs compatible with the $Z$ mass which in general is not the case in the signal models. Therefore, these two searches are not discussed here. Truth-level results from the five remaining analyses are presented below.

### 5.2.1 Signal Acceptance and Sensitivity

#### 5.2.1.1 The Gluino Model with LLE Couplings

The acceptances of the various searches for the events of the gluino model with $\lambda$ couplings depend strongly on the energies of the particles that are produced in the gluino and LSP decays. For an LSP-NLSP mass ratio $r = 0.1$ the jets from the gluino decays are energetic and the transverse momenta of the LSP decay products suppressed, whereas for $r = 0.9$ the opposite is true. Figure 5.9 illustrates the impact of the mass ratio $r$ on kinematic variables like the lepton and jet $p_{\mathrm{T}}$ and on the expected numbers of selected leptons and jets. The transverse momenta of the light charged leptons increase significantly with the LSP mass. This is also true for $E_{\mathrm{T}}^{\mathrm{miss}}$ because it arises entirely from the LSP decays. $E_{\mathrm{T}}^{\mathrm{miss}}$ is very large in this model. It becomes greater than 1 TeV for $r = 0.9$ and $m(\tilde{g}) = 1.4$ TeV. In contrast, the average jet $p_{\mathrm{T}}$ decreases with increasing LSP mass. In the gluino model with $\lambda$ couplings, most jets originate from the gluino decays and their energies are largest for $r = 0.1$ and smallest for $r = 0.9$. This behaviour is also shown by the number of jets per event illustrated in figure 5.9d. The last two plots (e) and (f) display the numbers of light leptons per event for scenarios rich in light leptons or taus, respectively. In the first scenario, most events contain four light leptons, whereas in the second scenario the number of light leptons per event is strongly reduced and only a small fraction of events contains four light leptons. These two plots show further that the mass ratio $r$ has only little impact on the number of light leptons per event.

The **four-lepton analysis** has already demonstrated good sensitivity to the gluino model with $\lambda$ couplings (see section 4.2.4). Figure 5.10 shows the truth-level signal yields as a function of the LSP branching ratios to taus corresponding to 20.3 fb$^{-1}$ of $\sqrt{s} = 8$ TeV data for the three 'noZb' signal regions of the four-lepton analysis with two choices of gluino and LSP masses. These signal regions of the four-lepton analysis provide better sensitivity than the others. For both signal mass assumptions, the signal yields in 'SR0noZb' are largest at the origin of the plot, which is expected as 'SR0noZb' requires at least four light leptons in the final state and thus strongly favours the $\tilde{\chi}_1^0 \to \ell\ell\nu$ decay. As the branching ratios of the LSP decays into left- or right-handed taus increase, the signal yield in 'SR0noZb' decreases rapidly due to the decreasing average number of light leptons per event.

The signal yields in 'SR1noZb' show a broad maximum around the line between (0, 0.5) and (0.75, 0). The absolute maximum is located at $\mathrm{BR}(\tau_R) = 0.75$, where the neutralino pair most likely produces three light leptons including those from $\tau$ decays. Finally, the signal

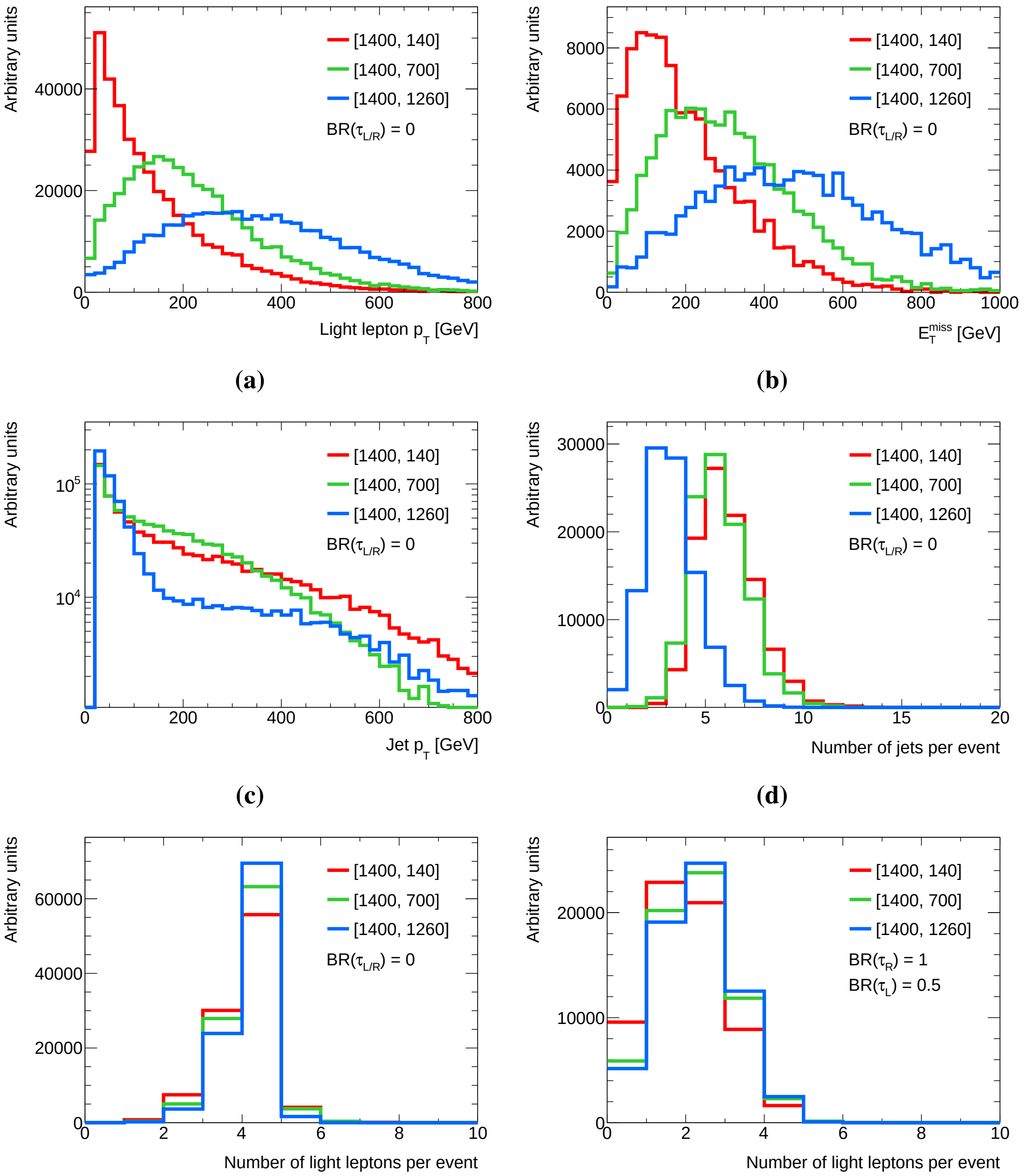

(a) (b)

(c) (d)

(e) (f)

**Figure 5.9:** Distributions of characteristic variables of events of the gluino model with $\lambda$ couplings for three mass points with $m(\tilde{g}) = 1.4$ TeV and different masses of the LSP which is assumed to decay only into light leptons (a-e), or with maximum rate into taus (f). In the $E_{\mathrm{T}}^{\mathrm{miss}}$ distribution (b) no cuts have been applied while for the remaining plots the selection criteria of the four-lepton analysis have been used, except for (d) where the cuts of the same-sign/three-lepton analysis for signal jets have been imposed.

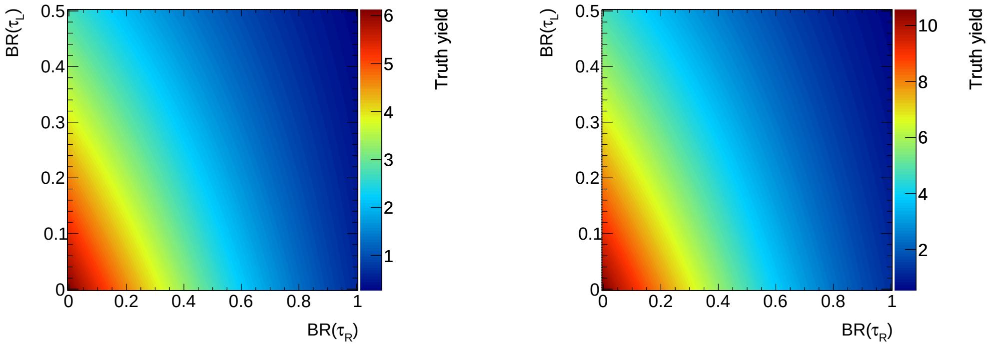

**(a)** [1400, 140], SR0noZb **(b)** [1400, 1260], SR0noZb

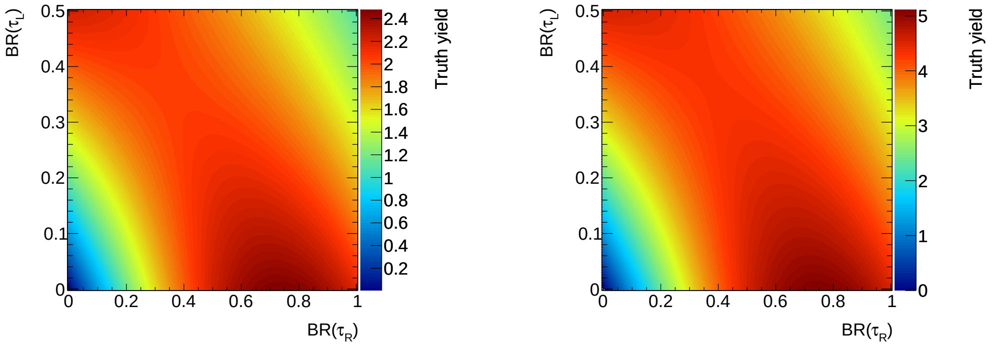

**(c)** [1400, 140], SR1noZb **(d)** [1400, 1260], SR1noZb

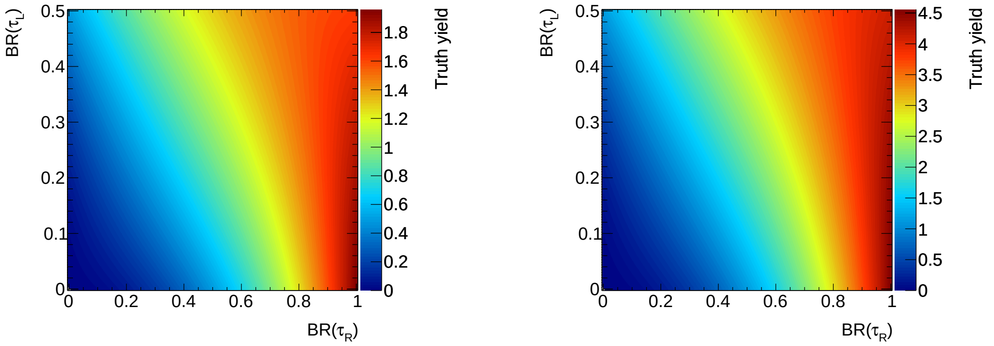

**(e)** [1400, 140], SR2noZb **(f)** [1400, 1260], SR2noZb

**Figure 5.10:** Expected numbers of signal events in the ‘noZb’ signal regions of the four-lepton analysis for the two extreme LSP masses of the gluino model with $\lambda$ couplings and $m(\tilde{g}) = 1.4$ TeV in figure 5.9 (see text).

yields in ‘SR2noZb’ peak at $\mathrm{BR}(\tau_R) = 1$, where at least two taus are produced per event, as required by the event selection.

The above dependences on the tau branching ratios do not depend on the LSP-gluino mass ratio. In contrast, the absolute signal yields of the four-lepton analysis do depend on the mass ratio, increasing significantly with $r$. As an estimate of the sensitivity the model-independent 95% CL upper limits on the signal yields listed in table 4.4 can be used: which are 3.7 events in ‘SR0noZb’, 3.5 events in ‘SR1noZb’, and 8.7 events in ‘SR2noZb’. These numbers indicate that the signal region ‘SR0noZb’ contributes most to the overall sensitivity since the signal yields in ‘SR0noZb’ are largest and the upper limit rather low.

The other analysis that may be sensitive to the gluino model with $\lambda$ couplings is the **same-sign/three-lepton search** [129]. Of the different signal regions in this search, the most sensitive one is ‘SR3Lhigh’, which requires at least three light leptons and at least four jets, each with $p_\mathrm{T} > 40$ GeV, in the final state as well as $E_\mathrm{T}^\mathrm{miss} > 150$ GeV and $m_\mathrm{eff} > 400$ GeV.

Figure 5.11 compares the signal yields in the signal regions ‘SR3Lhigh’ and ‘SR0noZb’ (from the four-lepton search) for three choices of the neutralino mass. The model-independent 95% CL upper limits on a non-Standard-Model contribution are similar for both signal regions, 4.6 and 3.7 events, respectively. As for ‘SR0noZb’, the signal yields in ‘SR3Lhigh’ are largest at the origin of the tau branching ratio square. However, the signal yields in ‘SR3Lhigh’ decrease much less steeply than those in ‘SR0noZb’ with increasing $\mathrm{BR}(\tau_{L/R})$. The reason is that only three light leptons are required for ‘SR3Lhigh’ and fewer events with four light leptons and more events with three light leptons are produced with increasing $\mathrm{BR}(\tau_{L/R})$ (see figure 5.9f). For mass ratios $r = 0.1$ and $r = 0.5$, the maximal signal yields in both signal regions are about the same, but the same-sign/three-lepton search has much higher sensitivity for large $\mathrm{BR}(\tau_{L/R})$. For $r = 0.9$, the signal yields in ‘SR3Lhigh’ are much smaller than in ‘SR0noZb’, because only a small fraction of events fulfils the requirement of ‘SR3Lhigh’ of at least four jets (see figure 5.9d) while ‘SR0noZb’ does not require any jets. Therefore, the four-lepton search shows higher sensitivity for $r = 0.9$ where the signal yields in ‘SR0noZb’ are largest.

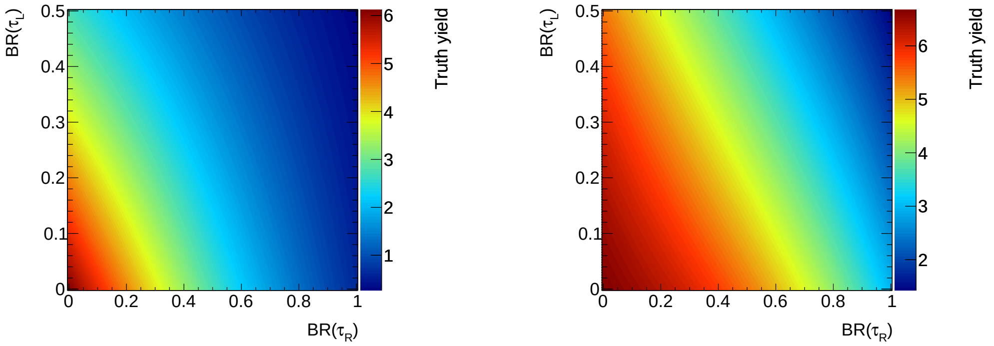

**(a)** [1400, 140], SR0noZb

**(b)** [1400, 140], SR3Lhigh

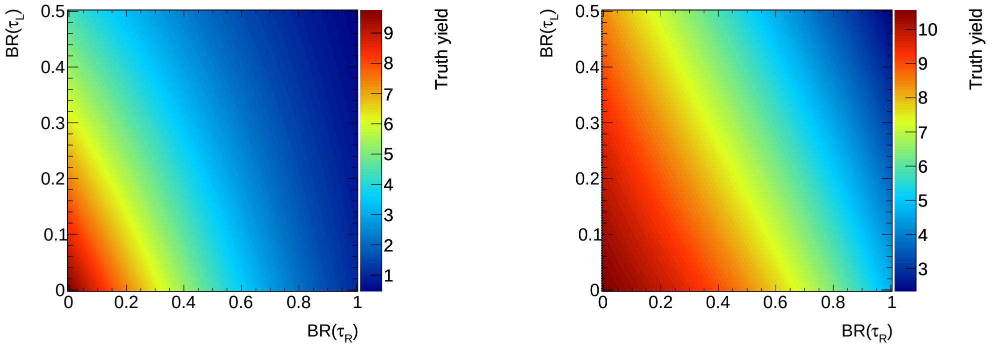

**(c)** [1400, 700], SR0noZb

**(d)** [1400, 700], SR3Lhigh

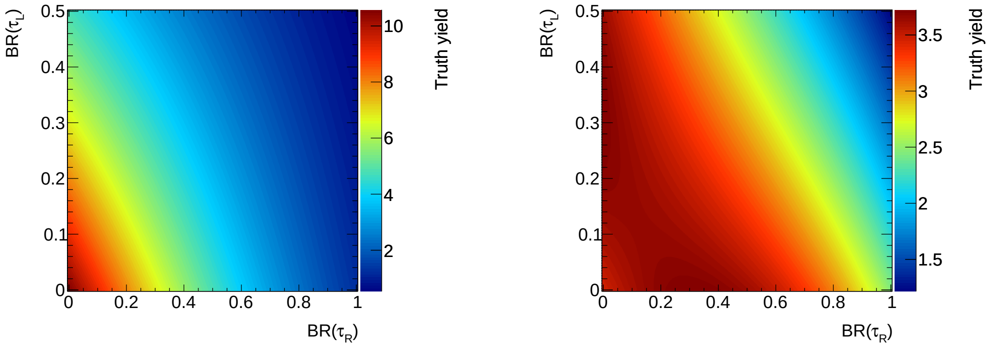

**(e)** [1400, 1260], SR0noZb

**(f)** [1400, 1260], SR3Lhigh

**Figure 5.11:** Expected numbers of signal events in the signal region 'SR0noZb' of the four-lepton analysis (left) compared to the signal yields in the signal region 'SR3Lhigh' of the same-sign/three-lepton analysis (right) for the three LSP masses of the gluino model with $\lambda$ couplings in figure 5.9 (see text).

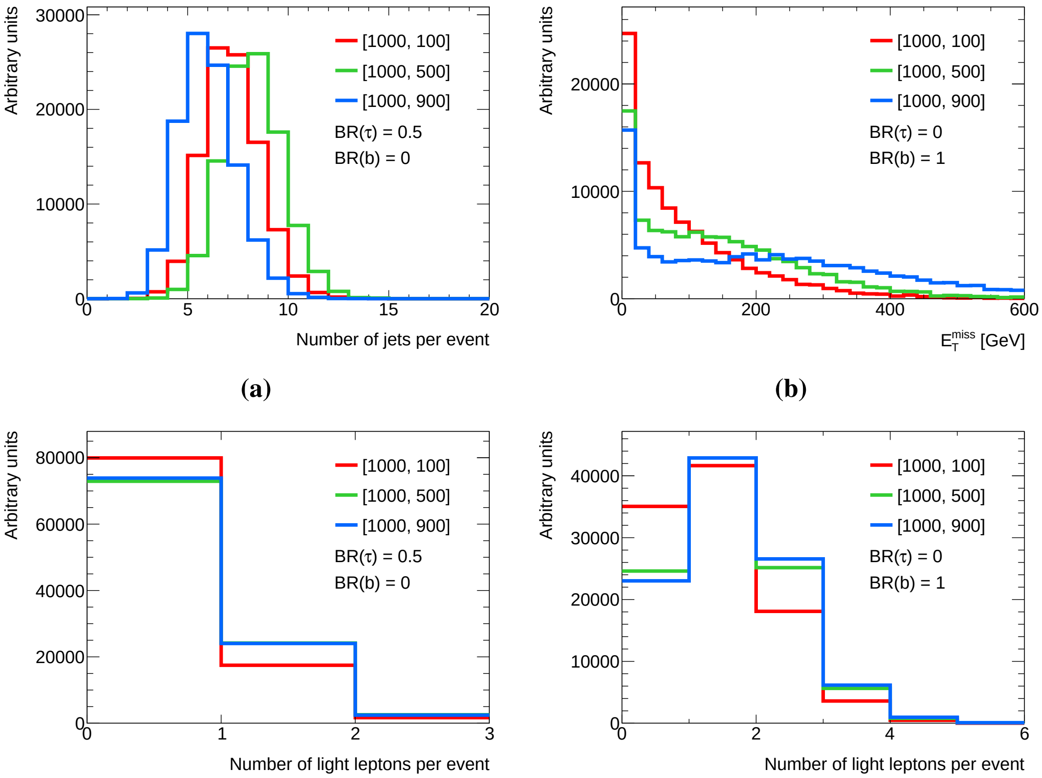

**(a)** **(b)**

**(c)** **(d)**

**Figure 5.12:** Distributions of characteristic variables for three mass points with $m(\tilde{g}) = 1.0$ TeV of the gluino model with $\lambda'$ couplings and different branching ratio hypotheses. In the $E_{\mathrm{T}}^{\mathrm{miss}}$ distribution (b) no cuts have been applied while for the remaining plots the selection criteria of the zero-lepton analysis have been used, including a cut of $p_{\mathrm{T}} > 60$ GeV in the jet transverse momentum.

#### 5.2.1.2 The Gluino Model with LQD Couplings

In the gluino model with $\lambda'$ couplings, four additional quarks are produced in the LSP decays leading to a high number of jets per event (see figure 5.12a). Events contain on average seven, eight or six jets with $p_{\mathrm{T}} > 60$ GeV for $r = 0.1$, $r = 0.5$ and $r = 0.9$, respectively, and $m(\tilde{g}) = 1.0$ TeV. Thus, considerably more high $p_{\mathrm{T}}$ jets are produced than in the gluino model with $\lambda$ couplings. The number of jets is largest for $r = 0.5$ because the jets both from LSP and gluino decays are energetic. Only the $\nu qq$ and $\tau qq$ LSP decay modes produce neutrinos; thus $E_{\mathrm{T}}^{\mathrm{miss}}$ depends on BR($\tau$). Examples of $E_{\mathrm{T}}^{\mathrm{miss}}$ distributions are shown in figure 5.12b. According to figure 5.12c and 5.12d, the average number of light leptons per event is relatively small. For $\mathrm{BR}(\tau) = 0.5$ most events contain no light lepton, whereas for $\mathrm{BR}(\tau) = 0$ there are more often two or three light leptons per event.

The one-lepton, the zero-lepton and the multijet analyses are potentially sensitive to the gluino model with $\lambda'$ couplings. The same-sign/three-lepton search has little sensitivity to this model, since the most sensitive signal regions require three light leptons and only few events contain three light leptons as shown in figure 5.12. Therefore, this search is not further discussed. The one-lepton analysis selects events, where one LSP decays to a light charged lepton and two quarks ($\ell qd$) and the other LSP to a neutrino and a quark pair ($\nu qd$) resulting in a high jet multiplicity and $E_{\mathrm{T}}^{\mathrm{miss}}$ due to the neutrino. The other two analyses are very sensitive to events where both LSPs decay to $\nu qd$, because they veto light leptons and also require large $E_{\mathrm{T}}^{\mathrm{miss}}$.

The **one-lepton analysis** [125] has two types of signal regions which are optimised either for the exclusion or the discovery of signal models. The exclusion signal regions exploit the expected shapes of the $E_{\mathrm{T}}^{\mathrm{miss}}$ or the $m_{\mathrm{eff}}$ distribution of signal events, which are not well described at truth-level. Thus, only the discovery signal regions are discussed in the following, which give a first impression how the sensitivity of the one-lepton analysis depends on the mass ratio $r$ and the LSP decay rates to bottom quarks and taus. They are categorised according to numbers of jets they require and the light lepton $p_{\mathrm{T}}$ cut. The truth-level studies indicate that the signal region requiring five jets and one light lepton with $p_{\mathrm{T}} > 25$ GeV is most sensitive (see figure 5.13). For this signal region different cuts on the jet $p_{\mathrm{T}}$ of 80, 50 GeV and 40 GeV are applied for the leading, second leading and third to fifth leading jet. Events with a second light lepton with $p_{\mathrm{T}} > 10$ GeV are vetoed. Furthermore, large $E_{\mathrm{T}}^{\mathrm{miss}}$ and $m_{\mathrm{eff}}$ of greater than 300 GeV and 1400 GeV, respectively, is required.

Figure 5.13 shows the signal yields in this signal region for three mass points. The signal yields are largest for $\mathrm{BR}(\tau) = 0$ and decrease with increasing $\mathrm{BR}(\tau)$, because the rate of events with one light lepton decreases as can be seen from figure 5.12c. The signal yields show little dependence on $\mathrm{BR}(b)$ as for this signal region $b$-jets are neither required nor vetoed. The signal yields increase strongly with the LSP mass. A potential reason is the high $E_{\mathrm{T}}^{\mathrm{miss}}$ cut, since $E_{\mathrm{T}}^{\mathrm{miss}}$ becomes larger for heavier LSPs. Figure 5.12b shows that for $r = 0.1$ only a tiny fraction of the events passes the $E_{\mathrm{T}}^{\mathrm{miss}}$ cut of 300 GeV. As the model-independent 95% CL upper limit on the beyond-Standard-Model event yield in this signal selection is 5.7,

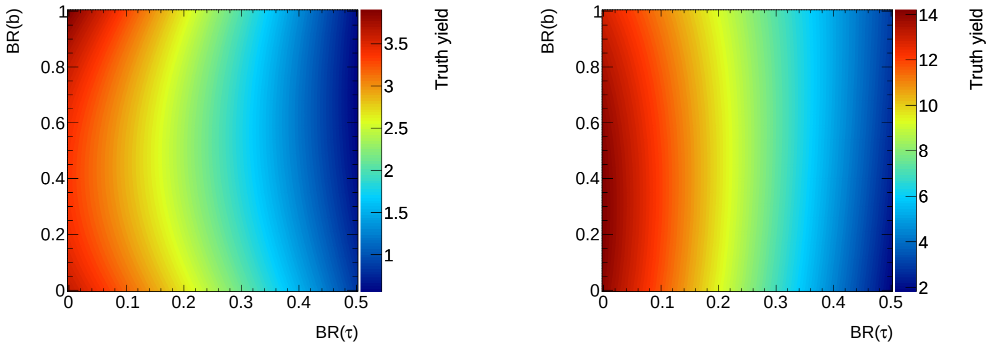

**(a)** [1000, 100] **(b)** [1000, 500]

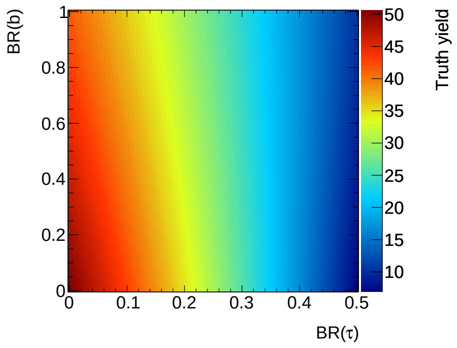

**(c)** [1000, 900]

**Figure 5.13:** Expected numbers of signal events in the discovery signal region of the one-lepton analysis requiring one energetic lepton and at least five jets for three NLSP-LSP mass points of the gluino model with $\lambda'$ couplings (see text).

the one-lepton analysis may be sensitive to all branching ratio combinations for the mass point [1000, 900] and to a large fraction of branching ratios for [1000, 500].

Regarding the **zero-lepton analysis**, the signal region ‘SR6jt+’ is found to be most sensitive to the gluino model with $\lambda'$ couplings for $m(\tilde{g}) \geq 1.0$ TeV due to its high signal acceptance and the very low Standard Model background (see section 4.3). In figure 5.14, the signal yields in ‘SR6jt+’ are shown for three choices of the neutralino mass. In all cases there is a maximum in the lower right corner where the LSP decays with equal probability to $\nu qd$ and $\tau qd$, and the signal yield decreases with decreasing $\mathrm{BR}(\tau)$ and increasing $\mathrm{BR}(b)$. The selection favours LSP decays to taus, since they are treated as jets and, therefore, not vetoed like electrons and muons. Jets from tau decays increase the jet multiplicity leading to

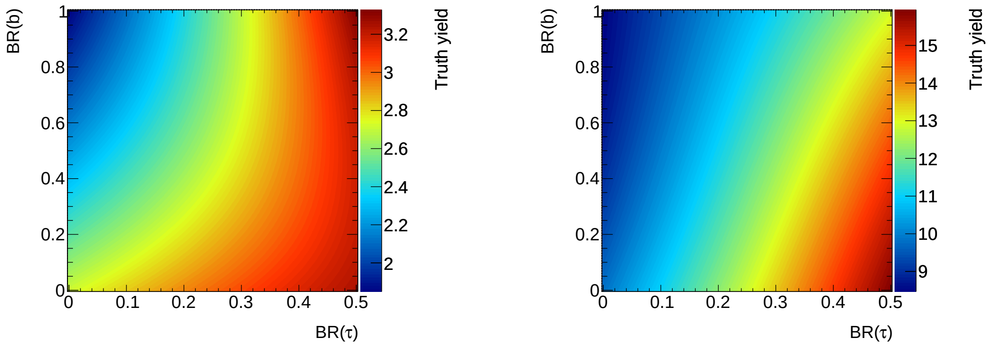

**(a)** [1000, 100] **(b)** [1000, 500]

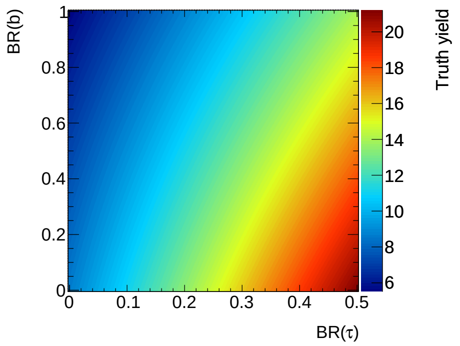

**(c)** [1000, 900]

**Figure 5.14:** Expected numbers of signal events in the signal region ‘SR6jt+’ of the zero-lepton analysis for three NLSP-LSP mass points of the gluino model with $\lambda'$ couplings (see text).

a higher probability that six jets survive the selection criteria in table 4.6. The sensitivity of the ‘SR6jt+’ selection is estimated from the model-independent 95% CL upper limit on beyond-Standard-Model events in the signal region of 7.9 which suggests that nearly the whole branching ratio square can be excluded for the mass points [1000, 500] and [1000, 900] while no constraints on the branching ratios seem possible for [1000, 100].

The signal yields in ‘SR6jt+’ are much smaller for the mass ratio of $r = 0.1$ than for the other two mass ratios. For large NLSP-LSP mass differences, the jets of the four quarks from the gluino decays are very energetic, while the momenta of the LSP decay products are small leading also to low $E_{\mathrm{T}}^{\mathrm{miss}}$. Figure 5.12b shows that many events indeed fail the $E_{\mathrm{T}}^{\mathrm{miss}}$

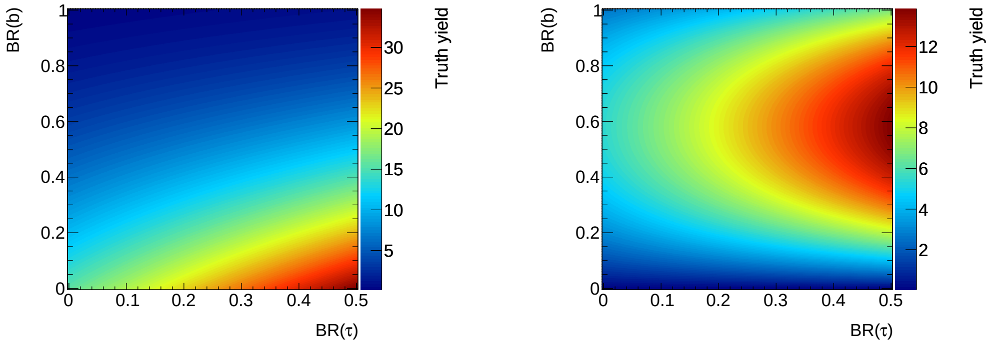

**(a)** $N(b\text{-jets}) = 0$ **(b)** $N(b\text{-jets}) = 1$

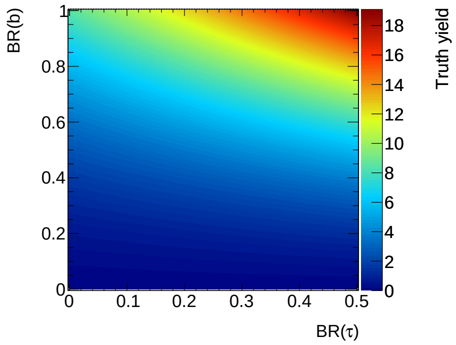

**(c)** $N(b\text{-jets}) \geq 2$

**Figure 5.15:** Expected numbers of signal events in three signal regions of the multijet analysis with increasing number of $b$-jets requiring at least eight jets with $p_T > 80$ GeV and the NLSP-LSP mass point [1000, 500] of the gluino model with $\lambda'$ couplings (see text).

cut of 160 GeV. Also the ratio $E_T^{\text{miss}}/m_{\text{eff}}(N_j = 6)$ defined in section 4.3.2 is rather small reducing the acceptance further.

There are no signal regions in the zero-lepton analysis that require or veto $b$-jets. Nevertheless, figure 5.14 shows that the signal yields in ‘SR6jt+’ tend to decrease with increasing $\text{BR}(b)$. An explanation can be semileptonic decays of $B$-hadrons into a $D$-meson, a charged lepton and a neutrino which reduces the visible jet $p_T$. Also the charged lepton from such a decay can cause the rejection of the event due to the $e/\mu$ veto which is applied to non-isolated leptons.

The third sensitive search to the gluino model with $\lambda'$ couplings is the **multijet analysis**. In some signal regions, cuts on the masses of so-called fat jets are applied. Fat jets have a

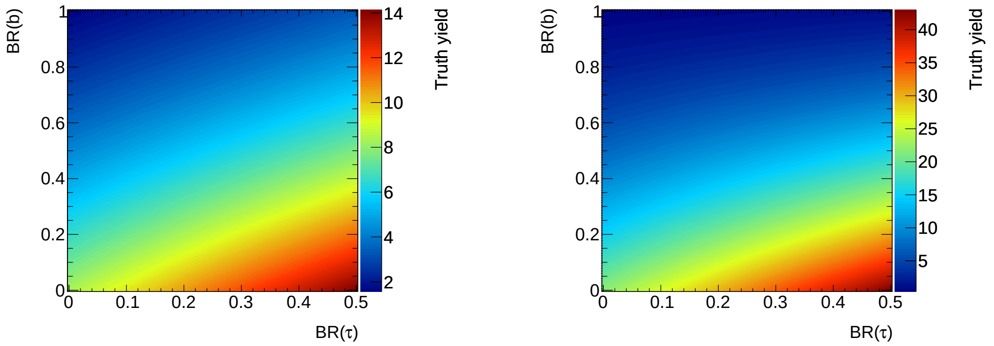

**(a)** [1000, 100] **(b)** [1000, 500]

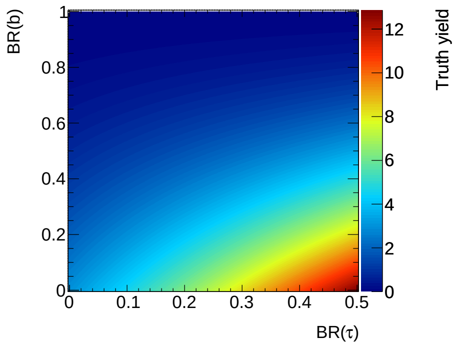

**(c)** [1000, 900]

**Figure 5.16:** Expected numbers of signal events in the signal region of the multijet analysis requiring exactly seven jets with $p_{\mathrm{T}} > 80$ GeV and zero $b$-jets for three NLSP-LSP mass points of the gluino model with $\lambda'$ couplings (see text).

larger cone radius $R = 1.0$ than standard jets with $R = 0.4$. Such signal regions are found to be less sensitive than the others and, therefore, are neglected in the following. The remaining signal regions are classified according to the numbers of jets and $b$-jets required. Furthermore, these signal regions are split into two classes, one requiring $p_{\mathrm{T}} > 50$ GeV and the other $p_{\mathrm{T}} > 80$ GeV for the jets. The 80 GeV regions are found to be more sensitive in most cases and, therefore, only results for them are presented in the following.

Figure 5.15 shows the signal yields in the three 80 GeV signal regions requiring at least eight jets including 0, 1 or $\geq 2$ $b$-jets for one choice of gluino and neutralino masses. In each case, the largest yield is obtained for $\mathrm{BR}(\tau) = 1$ and when the $b$-jet rate matches best the selection requirement. As for the zero-lepton analysis, regions with low $\mathrm{BR}(\tau)$ are

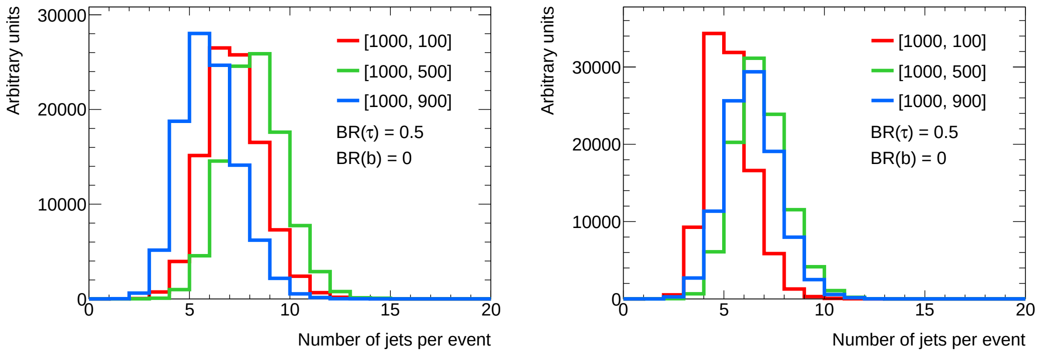

**(a)** Gluino model **(b)** Squark model

**Figure 5.17:** Multiplicity of jets with $p_\mathrm{T} > 60$ GeV in the two models with $\lambda'$ couplings for a NLSP mass of 1.0 TeV and different LSP masses.

disfavoured, because the multijet analysis treats taus as jets and vetoes events with electrons or muons.

Figure 5.16 shows the number of signal events in the 80 GeV signal region requiring exactly seven jets and zero $b$-jets for three choices of the neutralino mass. One can see that the signal yields of the multijet analysis are more than a factor of two higher for the mass ratio $r = 0.5$ than for the other two cases. This is expected, because the multijet analysis imposes the same $p_\mathrm{T}$ cut for all jets, such that more equal energies of jets from gluino and LSP decays lead to a higher acceptance.

The sensitivity is again estimated from the model-independent 95% CL upper limits on the number of non-Standard-Model events. In the case of the signal region of figure 5.16, the upper limit is 10 events. Thus, the multijet analysis can potentially exclude regions of the branching ratio square for gluino and LSP masses of 1000 and 100 GeV, respectively, which cannot be excluded by the zero-lepton analysis. For the same gluino mass and a LSP mass of 500 GeV, about 50% of the square may be excluded, whereas for a LSP mass of 900 GeV only a small fraction of the square is above the upper limit.

#### 5.2.1.3 The Squark Model with LQD Couplings

LSP decays mediated by $\lambda'$ couplings are also considered in the squark pair production model. Therefore, the one-lepton, zero-lepton and multijet analyses are expected to be sensitive like they are for the gluino model with $\lambda'$ couplings. The lepton and jet $p_\mathrm{T}$ as well

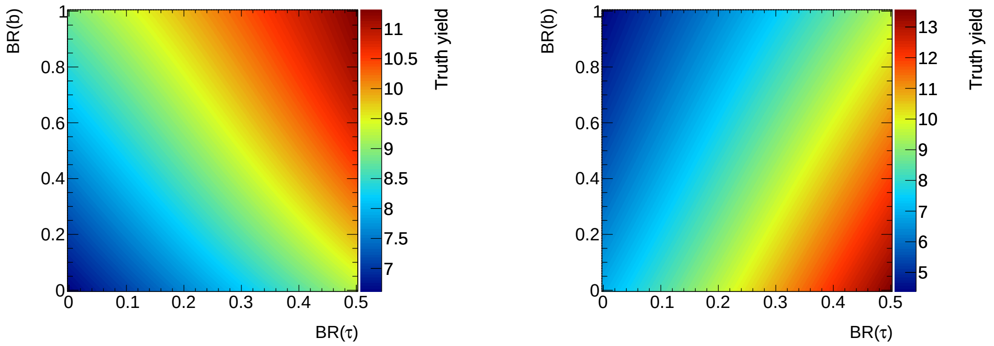

**(a)** [600, 60], SR5j **(b)** [800, 400], SR6jt+

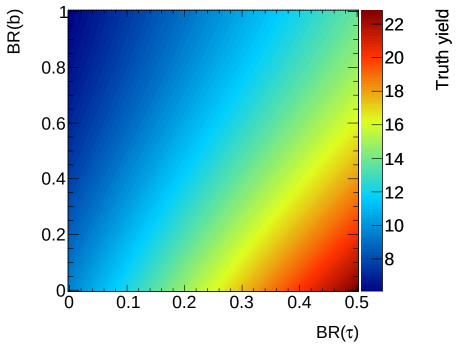

**(c)** [800, 720], SR6jt+

**Figure 5.18:** Expected numbers of signal events in the most promising signal regions of the zero-lepton analysis for three mass points of the squark model.

as $E_{\mathrm{T}}^{\mathrm{miss}}$ depend in a similar way on the LSP-NLSP mass ratio $r$ and $\mathrm{BR}(\tau)$ as in the gluino model with $\lambda'$ couplings. But the jet multiplicity is smaller in the squark model as shown in figure 5.17, because only two quarks instead of four quarks are produced in the NLSP decays. For $r = 0.9$, the number of high $p_{\mathrm{T}}$ jets can, nevertheless, be similar in both models since the jets from the NLSP decays are then low energetic and most high $p_{\mathrm{T}}$ jets originate from the LSP decays, which are the same in both models. The signal regions of the three analyses with the highest sensitivity are identically for both models in most cases. However, the acceptances of these signal regions are typically lower for the squark model compared to the gluino model, in particular for the multijet analysis which requires at least seven jets.

'SR6jt+' is the most sensitive signal region of the zero-lepton analysis for squark masses $m(\tilde{q}) \geq 800$ GeV, whereas for lower squark masses 'SR5j' and 'SR6jl' (see table 4.6) are

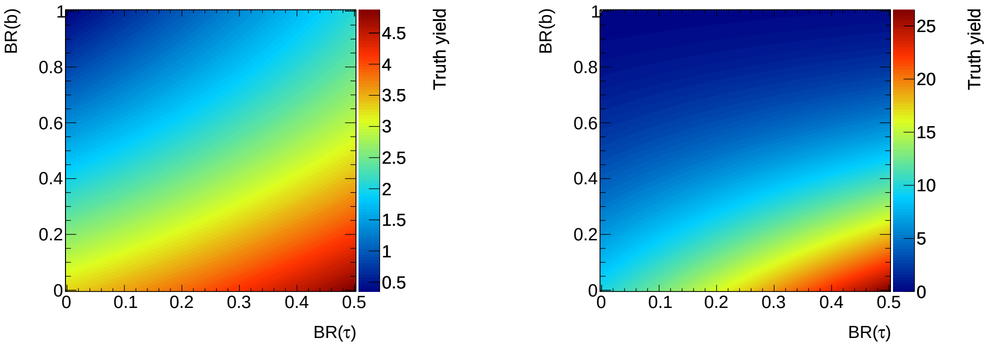

**(a)** [600, 60] **(b)** [800, 400]

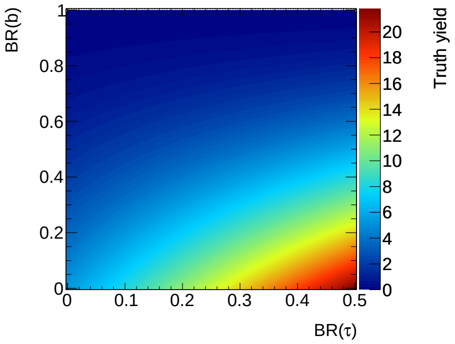

**(c)** [800, 720]

**Figure 5.19:** Expected numbers of signal events in the signal region of the multijet analysis requiring seven jets with $p_T > 80$ GeV and no $b$-jets for three mass points of the squark model.

in general better (see figure 5.18). For a squark mass of 800 GeV, the signal yields for the mass ratio $r = 0.5$ are about 50% lower than for $r = 0.9$. Nevertheless, about 50% and even 90% of the branching ratio square may be excluded by the zero-lepton search for $r = 0.5$ and $r = 0.9$, respectively. This dependence on the LSP mass is due to the fact that more jets originate from the LSP than from the squark decays. Thus, the zero-lepton analysis has no sensitivity to small mass ratios $r \approx 0.1$. Even for a squark mass of only 600 GeV the signal yield in the best signal region 'SR5j' is only one third of the model-independent upper limit of 35 events such that no exclusion is possible.

Figure 5.19 shows the numbers of signal events in the 80 GeV signal region of the multijet analysis requiring exactly seven jets and no $b$-jets for three mass points. No part of the

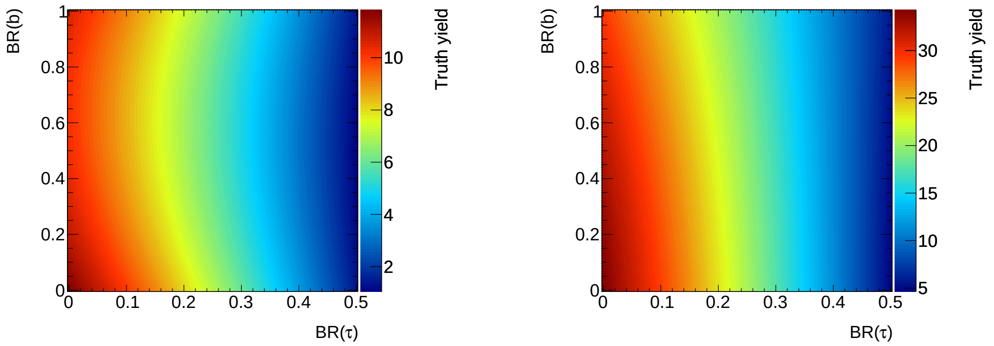

**(a)** [600, 60]

**(b)** [800, 400]

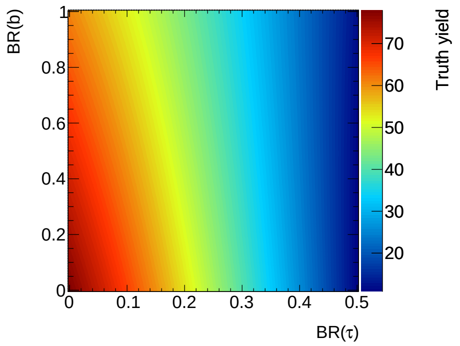

**(c)** [800, 720]

**Figure 5.20:** Expected numbers of signal events in the discovery signal region of the one-lepton analysis requiring one energetic lepton and at least five jets for three mass points of the squark model.

branching ratio square can be excluded for the mass point [600, 60] like for the zero-lepton analysis, because the largest signal yield is only about half of the model-independent upper limit of 10 events. For the other two mass ratios the signal yields are of about the same magnitude, in contrast to the gluino model where they are significantly larger for $r = 0.5$ than for $r = 0.9$. In both cases, triangles in the lower right corner covering $\leq 25\%$ of the square may be excluded by the multijet analysis.

The sensitivity of the one-lepton analysis is again estimated for the discovery signal region requiring five jets and one energetic light lepton. In figure 5.20 the expected numbers of signal events in this signal region are shown for three mass points. According to the model-independent upper limit of 5.7 events, the one-lepton analysis is sensitive to exclude about 50%, more than 95% and 100% of the square for the mass points [600, 60], [800, 400] and [800, 720], respectively. Therefore, the one-lepton analysis is the only search that may exclude mass points of the squark model with $r = 0.1$. Also for the other two mass ratios the one-lepton analysis seems to be sensitive to a larger branching ratio range than the other searches, especially at low $\mathrm{BR}(\tau)$.

### 5.2.2 Model-Dependent Systematic Uncertainties

The results of the reinterpretations of ATLAS supersymmetry searches discussed in the next section take into account all experimental systematic uncertainties in the signal yield from the corresponding publications as well as all systematic and statistical uncertainties in the background estimates. Systematic uncertainties specific for each signal model are also considered, namely from renormalisation and factorisation scale uncertainties and due to initial state radiation (ISR) and final state radiation (FSR) effects. ISR is emitted by the partons of the colliding protons before the sparticles are produced, whereas FSR is emitted by the sparticles and their decay products. Both ISR and FSR can lead to additional jets or leptons in the final state of an event.

The uncertainties due to these effects are determined by studying their impact on the signal acceptance at truth-level. For this purpose, the events were generated with the MadGraph 5 [143] and Pythia 6.4 [144] programs. MadGraph is used to generate the initial pair of sparticles and up to one additional ISR jet, while Pythia is used for all sparticle decays and the parton shower simulation.

The renormalisation and factorisation scales were varied independently by factors of $1/2$ and 2. The effect of ISR uncertainties was estimated by varying the scale of the strong interaction by factors of $1/2$ and 2. The matching scale relating matrix element radiation simulated by MadGraph and parton shower radiation in Pythia was varied by factors $1/2$ and 2 to estimate the effect of FSR uncertainty. Thus, for each systematic effect an up $(+)$ and a down $(-)$ variation was considered. The impact of a particular systematic variation v (scales, ISR, FSR) is described by the corresponding absolute deviation of the signal acceptance $A$ from the nominal value:

$$\Delta A_{\mathrm{v}^{+/-}} = |A_{\mathrm{v}^{+/-}} - A_{\mathrm{nom}}|. \tag{5.15}$$

For the following calculations, the larger one of the up and down variations is taken:

$$\Delta A_{\mathrm{v}} = \max(\Delta A_{\mathrm{v}^-}, \Delta A_{\mathrm{v}^+}). \tag{5.16}$$

These are summed in quadrature to obtain the total systematic uncertainty:

$$\Delta A = \sqrt{\sum_{\mathrm{v}} (\Delta A_{\mathrm{v}})^2}. \tag{5.17}$$

The statistical uncertainty of $\Delta A$ is calculated using Gaussian error propagation

$$\sigma(\Delta A) = \sqrt{\sum_{\mathrm{v}} \left[ \left( \frac{\partial \Delta A}{\partial A_{\mathrm{v}}} \right)^2 \cdot \sigma^2 (A_{\mathrm{v}}) \right] + \left( \frac{\partial \Delta A}{\partial A_{\mathrm{nom}}} \right)^2 \cdot \sigma^2 (A_{\mathrm{nom}})}, \tag{5.18}$$

where

$$\sigma(A_{\mathrm{v}}) = \sqrt{\frac{A_{\mathrm{v}} \cdot (1 - A_{\mathrm{v}})}{N_{\mathrm{v}}}} \tag{5.19}$$

and $\sigma(A_{\mathrm{nom}})$ are the statistical uncertainties in the varied and nominal signal acceptances $A_{\mathrm{v}}$ and $A_{\mathrm{nom}}$, and $N_{\mathrm{v}}$ is the number of generated events with variation v. The error in equation (5.17) is referred to as acceptance uncertainty.

For these studies it is important to ensure that sufficient statistical precision in the acceptance uncertainty determination is achieved. This means that the statistical uncertainty has to be much smaller than the effect of the different variations. A realistic goal for the statistical uncertainty was 5%. The acceptance uncertainties were only calculated at the four corners of each branching ratio square. The values for the other points are determined by linear interpolation with a formula analogous to equation 5.2. For each of the two signal models with $\lambda'$ couplings the number of Monte Carlo events required for the systematic studies of the acceptance of the most sensitive signal regions of the zero-lepton analysis was calculated separately for each corner of the square and each mass point.

Figure 5.21 shows the total relative uncertainty in the acceptance of the zero-lepton analysis for two mass points of the gluino model with $\lambda'$ couplings. The uncertainties are typically on the order of 10%, but can be as large as $\approx$ 30% for mass points with mass ratio $r = 0.1$ and gluino masses of $\leq 1$ TeV. As the statistical precision of the acceptance uncertainty determination is about 5%, the scale and ISR/FSR variations apparently have a significant impact on the acceptance. This is expected for analyses relying on jets and $E_{\mathrm{T}}^{\mathrm{miss}}$ for the signal region selection, whereas analyses requiring leptons are less sensitive to these variations.

Two examples for the squark model are shown in figure 5.22. Here the uncertainties are slightly larger than for the gluino model, typically in the range of 12-15%. Again, they reach

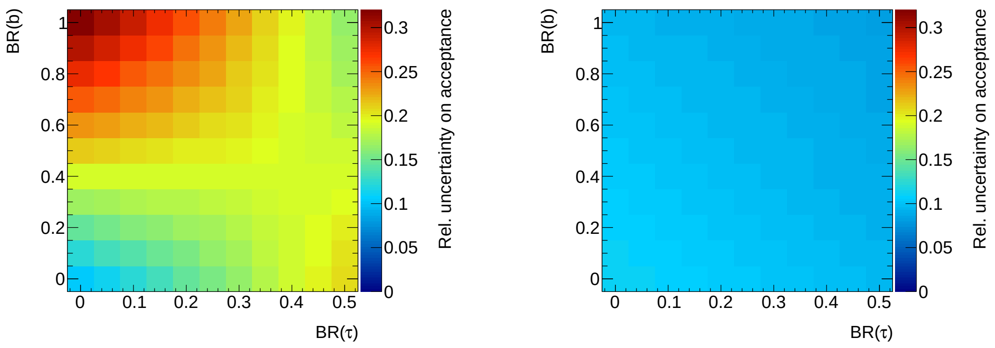

**(a)** [800, 80] **(b)** [1000, 900]

**Figure 5.21:** Relative uncertainty in the acceptance of the signal region 'SR6jt+' of the zero-lepton analysis for two mass points of the gluino model with $\lambda'$ couplings.

30% for a mass ratio of $r = 0.1$. For both models the acceptance uncertainty is the dominant systematic uncertainty in the signal prediction together with the cross-section uncertainty.

The acceptance uncertainties of the zero-lepton analysis for all mass points of the two models with $\lambda'$ couplings can be found in appendix A.

The systematic uncertainties in the acceptance for the four-lepton analysis reinterpretation of the gluino model with $\lambda$ couplings have already been determined in reference [130]. The four-lepton analysis in [130] considered LSP decays corresponding to the lower left and the upper right corner of the branching ratio square (see figure 4.3) where the systematic uncertainties in the acceptance are 2.1% and 6.1%, respectively. These acceptance uncertainties can also be used for the reinterpretation. For a conservative estimate, the larger of the two values is used for every Monte Carlo event in which at least one tau is produced in the LSP decays and the lower value if both LSPs decay to light leptons.

## 5.3 Results of the Reinterpretation

In this section, constraints on the three RPV supersymmetric models discussed in section 5.1 are presented, which have been derived with the four-lepton and zero-lepton searches using 20.3 $\text{fb}^{-1}$ of $\sqrt{s} = 8$ TeV data together with the existing background estimates of the two searches. Signal events have been generated with the simulation program Herwig++ in the same way as for the truth-level studies in section 5.2. Detector effects have been taken into account based on the fast ATLAS detector simulation described in section 3.4.

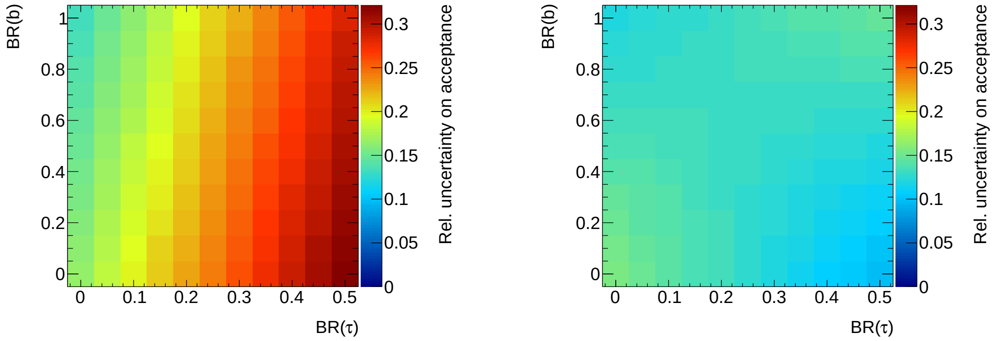

**(a)** [600, 60], SR5j

**(b)** [800, 720], SR6jt+

**Figure 5.22:** Relative uncertainty in the acceptance for two mass points of the squark model of the appropriate signal regions of the zero-lepton analysis.

In addition to the four-lepton and zero-lepton searches, three other ATLAS searches are sensitive to the signal models as shown by the truth-level studies. Reinterpretations of these three searches will be followed up in the context of an other ATLAS analysis project.

### 5.3.1 Statistical Procedure

The statistical analyses are performed with the software package HistFitter [132] which tests the compatibility of the selected data with the predictions of the Standard Model using a profile log likelihood ratio test [145]. The likelihood function $L$ for a signal region SR is the product of Poisson distributions evaluated for the event yields $n_S$ in the SR as well as $n_i$ in the associated background control regions $i$ and of additional distributions $C_{\text{syst}}$ implementing constraints on systematic uncertainties:

$$\begin{aligned}L(\vec{n},\vec{\theta}^0|\mu_{\text{sig}},\vec{b},\vec{\theta}) &= P_{\text{SR}} \times P_{\text{CR}} \times C_{\text{syst}} \\ &= P(n_S|\lambda_S(\mu_{\text{sig}},\vec{b},\vec{\theta})) \times \prod_{i\in\text{CR}} P(n_i|\lambda_i(\mu_{\text{sig}},\vec{b},\vec{\theta})) \times C_{\text{syst}}(\vec{\theta}^0,\vec{\theta}),\end{aligned} \tag{5.20}$$

where $\lambda_S$ and $\lambda_i$ are the mean values of the Poisson distributions which depend on the signal strength $\mu_{\text{sig}} = \sigma^{\text{fit}}_{\text{sig}}/\sigma^{\text{exp}}_{\text{sig}}$, a vector of all background contributions $\vec{b}$ and a vector of nuisance parameters $\vec{\theta}$ describing systematic uncertainties which are varied around their central values $\vec{\theta}^0$. For independent nuisance parameters, $C_{\text{syst}}$ is the product of Gaussian distributions of unit width around $\theta^0_j$ for each nuisance parameter $\theta_j$. Signals are also considered in the control regions leading to a dependence of $\lambda_i$ on $\mu_{\text{sig}}$ in order to account for signal contamination (see section 5.3.3.1). The signal strength $\mu_{\text{sig}}$ is a scale factor of the number of signal events relative to the model expectation with $\mu_{\text{sig}} = 0$ in the absence of a signal and $\mu_{\text{sig}} = 1$ if the number of signal events is equal to the prediction of the model considered.

A test statistic $q_{\mu_{\text{sig}}}$ is defined for signal hypotheses characterised by $\mu_{\text{sig}}$ using the logarithm of the profile likelihood ratio:

$$q_{\mu_{\text{sig}}} = -2\log\left(\frac{L(\mu_{\text{sig}}, \hat{\hat{\theta}})}{L(\hat{\mu}_{\text{sig}}, \hat{\theta})}\right), \tag{5.21}$$

where $\hat{\mu}_{\text{sig}}$ and $\hat{\theta}$ maximise the likelihood function simultaneously while $\hat{\hat{\theta}}$ maximises the likelihood function for a given value of $\mu_{\text{sig}}$. The signal hypotheses are tested over a range of $\mu_{\text{sig}}$ values, starting with $\mu_{\text{sig}} = 0$ and ending with a $\mu_{\text{sig}}$ value for which the $p$-value of the test becomes less than 5%. The $p$-value is calculated using asymptotic formulae of the distribution of the test statistic and gives the probability that the signal hypothesis is consistent with the data. The 95% CL upper limit on $\mu_{\text{sig}}$ is defined as the $\mu_{\text{sig}}$ value for which the $p$-value of the hypothesis test is 5%. The results of the hypothesis tests are linearly interpolated if necessary to calculate this upper limit.

The cross-section upper limit is defined as the product of the model cross-section and the 95% CL upper limit on $\mu_{\text{sig}}$. The lower limit on the NLSP mass in a given model is defined as the NLSP mass where the 95% CL upper limit on $\mu_{\text{sig}}$ becomes equal to 1.0. For this calculation $\log \mu_{\text{sig}}$ is linearly interpolated between the simulated mass points. As previously mentioned, according to convention, the mass limits are not based on the nominal cross-section, but on the nominal cross-section reduced by one standard deviation.

### 5.3.2 Four-Lepton Analysis Reinterpretation

The reinterpretation of the four-lepton analysis is relevant for the gluino model with $\lambda$ couplings. Model-dependent gluino mass limits are studied here taking into account detector effects on the signal yield and background estimates from data. The truth-level results of section 5.2 do not consider the reconstruction and identification efficiencies of the particles. Figure 5.23 compares the truth-level signal yields for the gluino model with $\lambda$ couplings at a particular mass point in the 'noZb' signal regions of the four-lepton search with those with fast detector simulation corresponding to 20.3 fb$^{-1}$ of data. In the case of 'SR0noZb', the

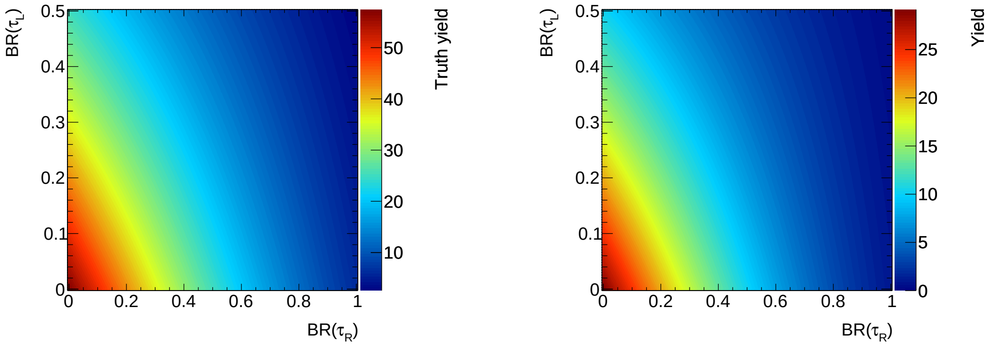

**(a)** SR0noZb, truth-level **(b)** SR0noZb, with detector simulation

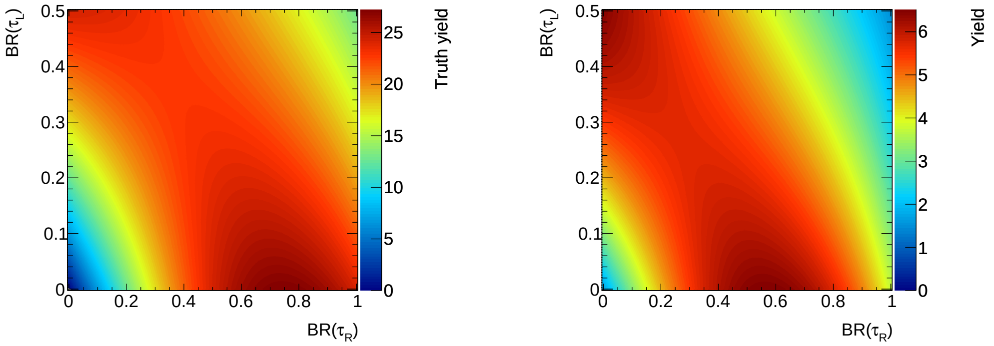

**(c)** SR1noZb, truth-level **(d)** SR1noZb, with detector simulation

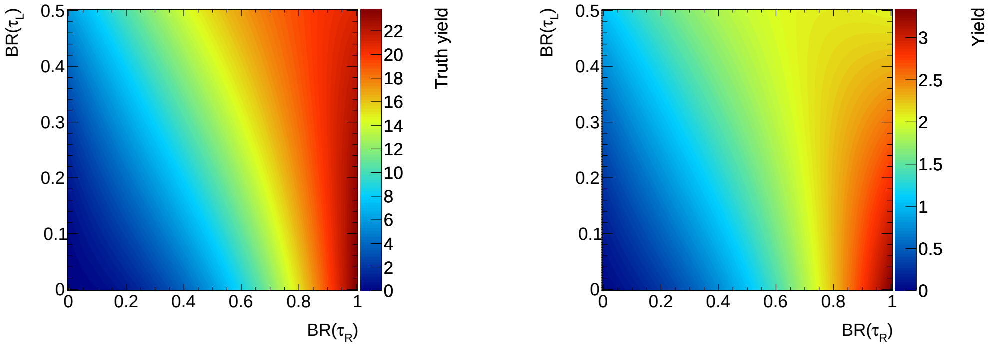

**(e)** SR2noZb, truth-level **(f)** SR2noZb, with detector simulation

**Figure 5.23:** Expected numbers of signal events in the 'noZb' signal regions of the four-lepton analysis at truth-level (left) and with detector simulation (right) for the mass point [1200, 1080] of the gluino model with $\lambda$ couplings corresponding to 20.3 $\text{fb}^{-1}$ of data.

reconstruction and identification efficiencies reduce the yield by about 50% with respect to the truth-level. The signal yields in 'SR1noZb' and 'SR2noZb' decrease by up to 80% due to the much lower tau reconstruction efficiency. The reconstruction efficiencies also have an impact on the sensitivity as a function of $\mathrm{BR}(\tau_{L/R})$. The largest signal yield in 'SR1noZb' is now at $\mathrm{BR}(\tau_R) = 0.55$ instead of 0.75 and the broad maximum is shifted to the left. In addition, after detector simulation the signal yield in 'SR1noZb' becomes non-zero at the origin of the branching ratio square due to jets misidentified as taus. Regarding 'SR2noZb', the yields for $\mathrm{BR}(\tau_R) = 1$ now decrease with increasing $\mathrm{BR}(\tau_L)$. In view of the much higher model-independent upper limit $N^{\mathrm{obs}}_{\mathrm{BSM}} = 8.7$ events in 'SR2noZb' compared to 3.7 events and 3.5 events in 'SR0noZb' and 'SR1noZb', respectively, the contribution of the 'SR2noZb' selection in most cases is negligible.

The signal contamination in the two control regions used to extract the reducible background (see section 4.2.3) was evaluated and is taken into account. The effect on the limits is below 2%.

The 'noZb' regions are used to derive upper limits on the cross-section, because they provide better sensitivity than the other four-lepton signal regions. The three 'noZb' signal regions are statistically independent since each event can only pass the selection criteria for one of the regions and therefore the results for them can be directly combined. Figures 5.24 to 5.26 show the cross-section upper limits obtained for 13 mass points of the gluino model with $\lambda$ couplings (see table 5.1). Lower values indicate better sensitivity. The trend is the same in all cases: the best limits are obtained at the origin and get worse with increasing $\mathrm{BR}(\tau_L)$ and $\mathrm{BR}(\tau_R)$. This is due to the fact that the most sensitive signal region 'SR0noZb' favours events where both LSPs decay to light leptons. The upper limits range from 0.4 fb up to 47 fb and are mostly in the range of 1 - 10 fb. In the case of $r = 0.1$ and large $\mathrm{BR}(\tau_{L/R})$, the upper limits are weak since both 'SR1noZb' and 'SR2noZb' contributing in this region contain less than 1% of the signal events. The fractions of events passing the selection criteria of the 'noZb' signal regions and, therefore, the upper limits do not depend on the gluino mass for $r = 0.5$ and $r = 0.9$.

The cross-section upper limits are used to obtain lower limits on the gluino mass for each LSP decay hypothesis and each LSP-NLSP mass ratio. These limits are shown in figure 5.27 for three mass ratios. The mass limits increase as the LSP mass increases, because then the leptons from the LSP decay become more energetic and also $E_{\mathrm{T}}^{\mathrm{miss}}$ larger. The limits range

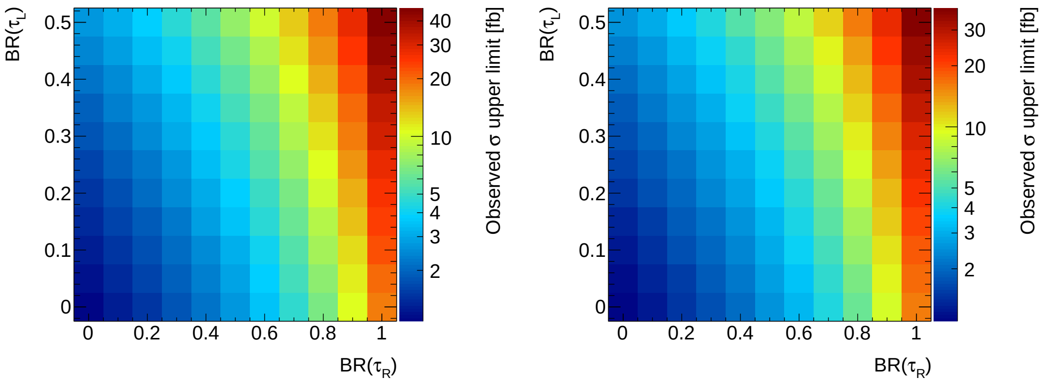

**(a)** [800, 80]

**(b)** [1000, 100]

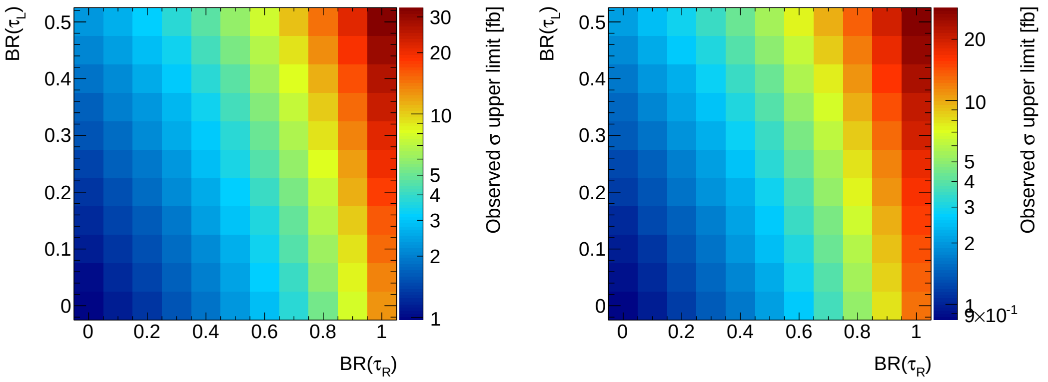

**(c)** [1200, 120]

**(d)** [1400, 140]

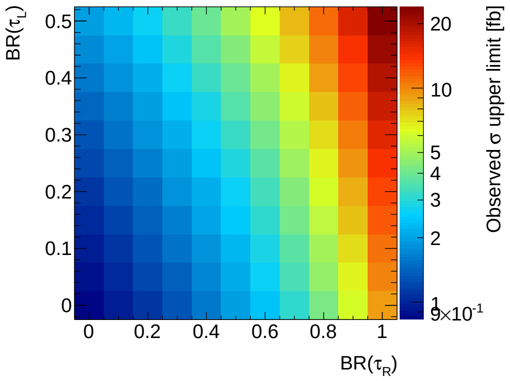

**(e)** [1600, 160]

**Figure 5.24:** Observed 95% CL upper limits on the signal cross-section of the gluino model with $\lambda$ couplings for the mass points with a ratio $r = 0.1$ from the reinterpretation of the four-lepton analysis.

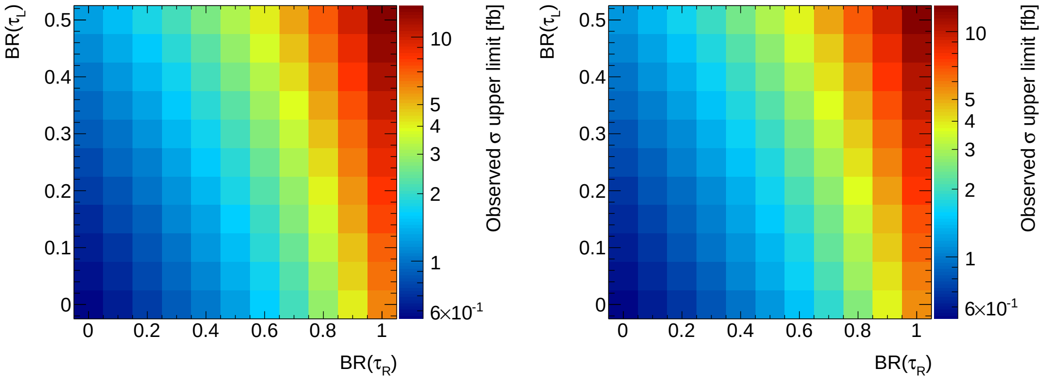

**(a)** [1000, 500]

**(b)** [1200, 600]

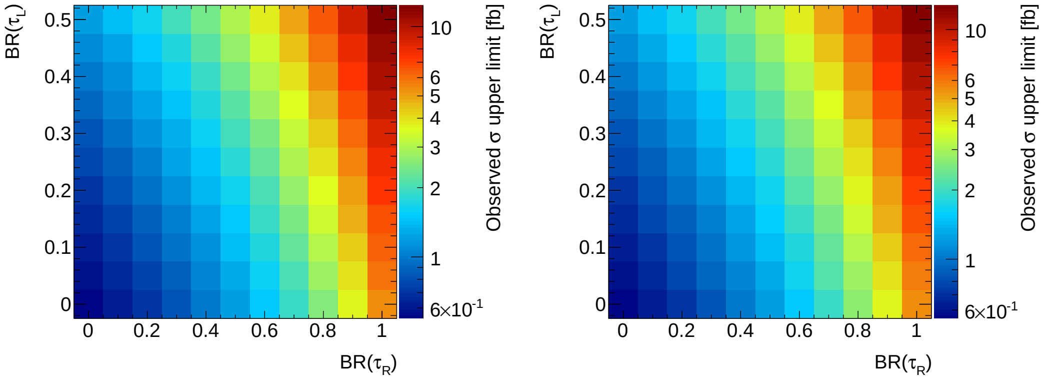

**(c)** [1400, 700]

**(d)** [1600, 800]

**Figure 5.25:** Observed 95% CL upper limits on the signal cross-section of the gluino model with $\lambda$ couplings for the mass points with a ratio $r = 0.5$ from the reinterpretation of the four-lepton analysis.

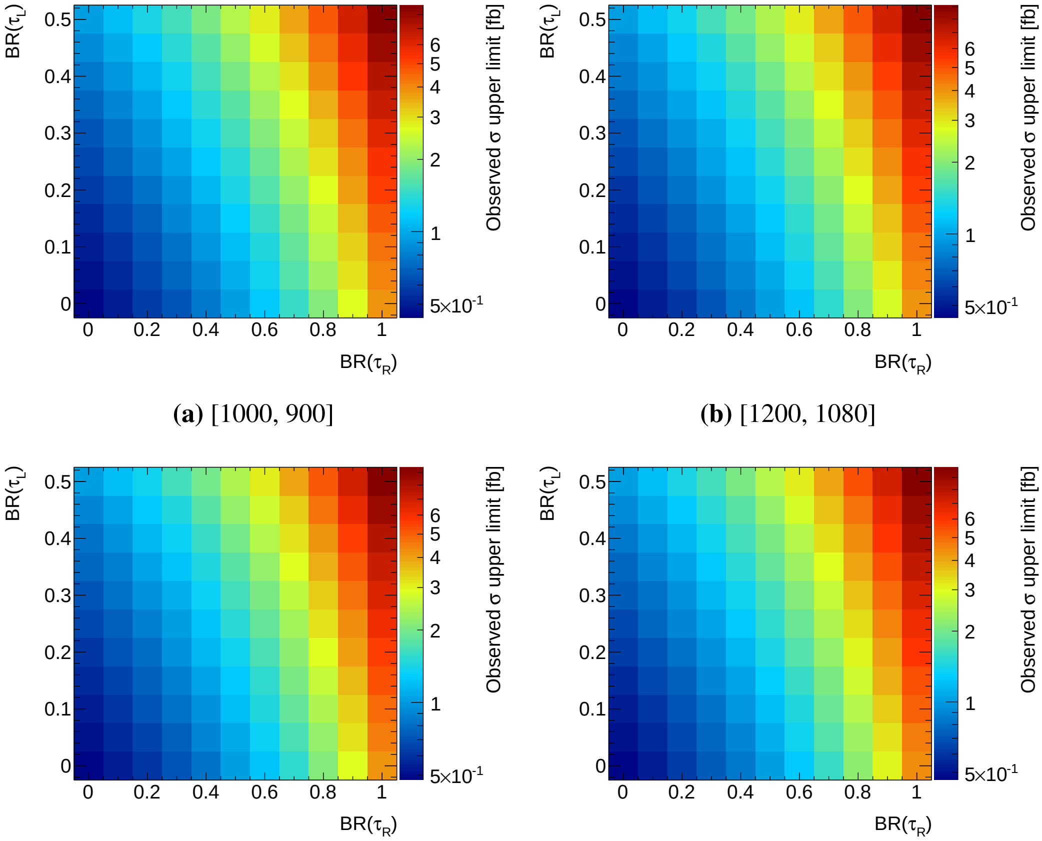

**(a)** [1000, 900]

**(b)** [1200, 1080]

**(c)** [1400, 1260]

**(d)** [1600, 1440]

**Figure 5.26:** Observed 95% CL upper limits on the signal cross-section of the gluino model with $\lambda$ couplings for the mass points with a ratio $r = 0.9$ from the reinterpretation of the four-lepton analysis.

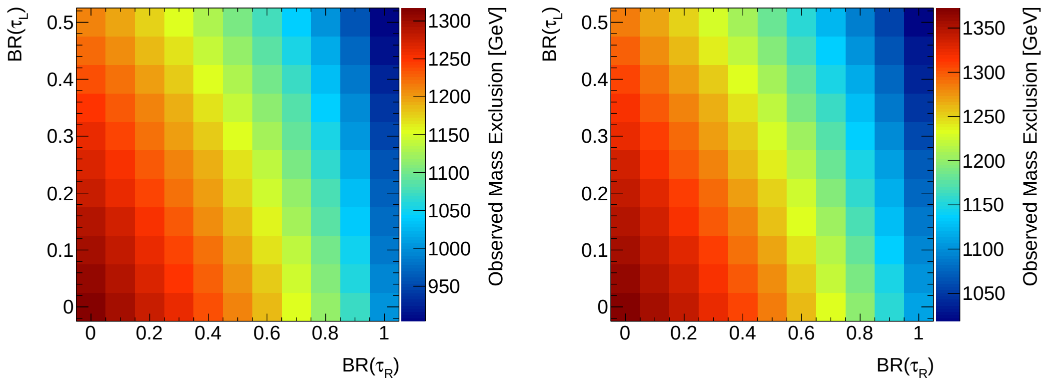

**(a)** $r = 0.1$

**(b)** $r = 0.5$

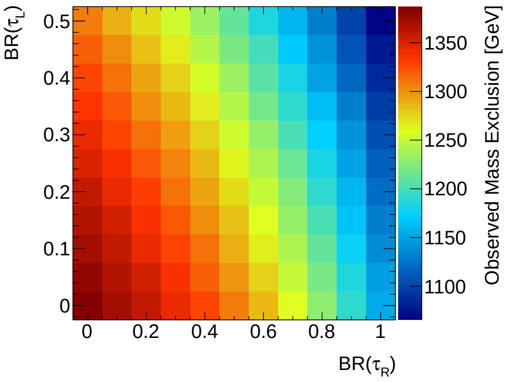

**(c)** $r = 0.9$

**Figure 5.27:** Observed 95% CL lower limits on the gluino mass of the gluino model with $\lambda$ couplings for the three mass ratios $r$ from the reinterpretation of the four-lepton analysis.

from 900 to 1320 GeV for $r = 0.1$, from 1020 to 1370 GeV for $r = 0.5$, and from 1070 to 1390 GeV for $r = 0.9$.

These results can be directly compared to those of the four-lepton analysis in [130] (see figure 4.3) which considered four different LSP decays, each mediated by a single RPV coupling. Neutralino decays via $\lambda_{121}$ and $\lambda_{122}$ couplings lead to final states consisting of four light leptons and $\lambda_{133}$ and $\lambda_{233}$ couplings to final states with at least two taus corresponding to the lower left and to the upper right corner of the branching ratio square, respectively (see figure 5.2). In the reinterpretation in this thesis, the branching ratios of the LSP to electrons and muons are assumed to be equal such that to first approximation the mass limit

**Table 5.3:** 95% CL lower limits on the gluino mass in GeV from the four-lepton analysis [146] in the gluino model for which the LSP decays only to light leptons (top) or frequently to taus (bottom). The fifth column shows the limits from the reinterpretation in this thesis. In the last column the relative difference between the average of the two four-lepton limits and the reinterpretation limit is shown.

| $r$ | $m_{\tilde{g}}(\lambda_{121})$ | $m_{\tilde{g}}(\lambda_{122})$ | Average | Reinterpretation | Difference |
|---|---|---|---|---|---|
| 0.1 | 1381 | 1385 | 1383 | 1384 | $+0.1\%$ |
| 0.5 | 1483 | 1437 | 1460 | 1439 | $-1.4\%$ |
| 0.9 | 1532 | 1445 | 1489 | 1456 | $-2.2\%$ |
| $r$ | $m_{\tilde{g}}(\lambda_{133})$ | $m_{\tilde{g}}(\lambda_{233})$ | Average | Reinterpretation | Difference |
| 0.1 | 905 | 935 | 920 | 937 | $+1.8\%$ |
| 0.5 | 1069 | 1044 | 1057 | 1058 | $+0.1\%$ |
| 0.9 | 1120 | 1097 | 1109 | 1105 | $-0.4\%$ |

corresponding to the lower left corner should be close to the average of the $\lambda_{121}$ and $\lambda_{122}$ mass limits of [130]. Similarly, the limit of the reinterpretation in the tau-rich scenario at the upper right corner should be close to the average of the individual $\lambda_{133}$ and $\lambda_{233}$ limits. Table 5.3 lists the lower limits on the gluino mass for the different couplings and different LSP-NLSP mass ratios $r$. In contrast to all other mass limits presented in this thesis, the values in this table were obtained using the nominal cross-section, because only for this case exact numbers have been uploaded by the ATLAS collaboration to HepData [146]. The mass limits obtained here agree with the existing limits of the lower left and upper right corners of the branching ratio square within 2%. In addition the mass limits are extended here to the full square.

### 5.3.3 Zero-Lepton Analysis Reinterpretation

The reinterpretation of the zero-lepton analysis is relevant for the gluino and squark models with $\lambda'$ couplings.

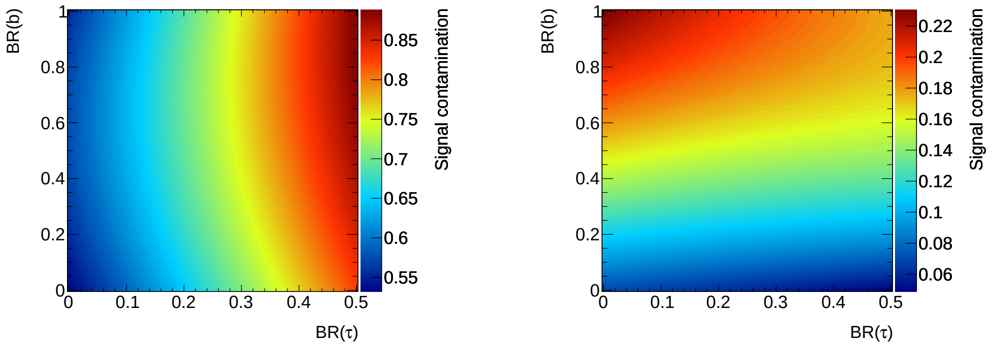

**(a)** [600, 60], CRQ of SR6jl

**(b)** [800, 400], CRT of SR6jm

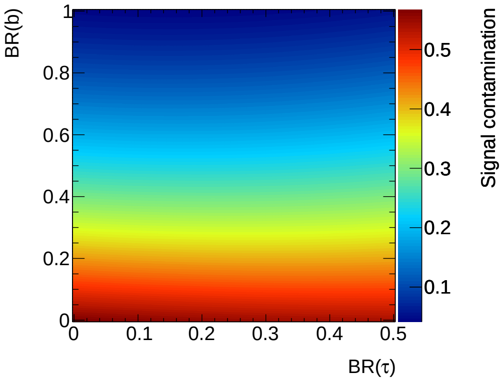

**(c)** [1000, 900], CRW of SR6jt+

**Figure 5.28:** The largest signal contamination (defined as the number of signal events expected in a control region divided by the total number of data events in the control region) of the control regions CRQ, CRT and CRW for different zero-lepton signal regions contributing in the final limits for three mass points of the gluino model with $\lambda'$ couplings.

#### 5.3.3.1 Signal Contamination in the Control Regions

In contrast to the results of section 5.3.2, the models with $\lambda'$ couplings were not considered previously by the zero-lepton analysis. Therefore it is important to clarify whether signal events can pass the selection requirements of the control regions used for background estimation. Such signal contaminations of the control regions bias the background estimates. They are taken into account in the likelihood fits for the signal evaluation. Nevertheless, they weaken the exclusion limits depending on the sizes of their background contributions. The signal contamination is defined as the number of signal events expected in a control region divided by the number of data events in the control region.

Four control regions (CR$\gamma$, CRQ, CRT and CRW) per signal region are defined in the zero-lepton analysis (see table 4.7). In nearly all cases, the signal contamination of CR$\gamma$ is smallest and always stays below 10%. The largest signal contaminations of the other three control regions for the gluino model with $\lambda'$ couplings are shown in figure 5.28, considering only signal regions contributing to the final results.

For low mass points like [600, 60], the signal contamination of CRQ can become very large with values up to 90%. The contamination is largest if $\mathrm{BR}(\tau) = 1$, because in this control region $E_{\mathrm{T}}^{\mathrm{miss}}$ is required to be azimuthally aligned with a jet. In tau-rich events, a significant part of $E_{\mathrm{T}}^{\mathrm{miss}}$ is contributed from the neutrinos from tau decays which point in the same directions as the jets from the same tau decays.

The signal contamination of CRT is lowest (below 5%) for the mass points [600, 60] and [800, 80], highest (up to 23%) for [800, 400] and stays below 20% for all other mass points. For CRT at least one $b$-jet is required and, therefore, the signal contamination increases with $\mathrm{BR}(b)$.

For $m(\tilde{g}) \leq 1.0$ TeV and $\mathrm{BR}(b) \lessapprox 0.6$ the signal contamination of CRW is in general large with values up to 60%. Since for CRW $b$-jets are vetoed, the signal contamination is largest for $\mathrm{BR}(b) = 0$.

The contaminations of the control regions from signals of the squark model show the same overall behaviour and similar values as for the gluino model with $\lambda'$ couplings except for CRQ where the contamination is significantly lower for mass points with $m(\tilde{q}) \leq 800$ GeV with values only up to 20%. The largest signal contamination for the squark model is about 65%.

#### 5.3.3.2 The Gluino Model with LQD Couplings

As in the four-lepton reinterpretation in section 5.3.2, the lepton reconstruction and identification efficiencies have a significant impact on the signal yields of the zero-lepton analysis. Figure 5.29 compares the truth-level signal yields with those after detector simulation for the signal region ‘SR6jt+’ and three representative mass points. Unlike for the four-lepton analysis, the signal yields of the zero-lepton analysis increase with taking into account the detector effects. An explanation is that not all electrons or muons in the model events are reconstructed due to detector efficiencies and therefore fewer events are discarded by

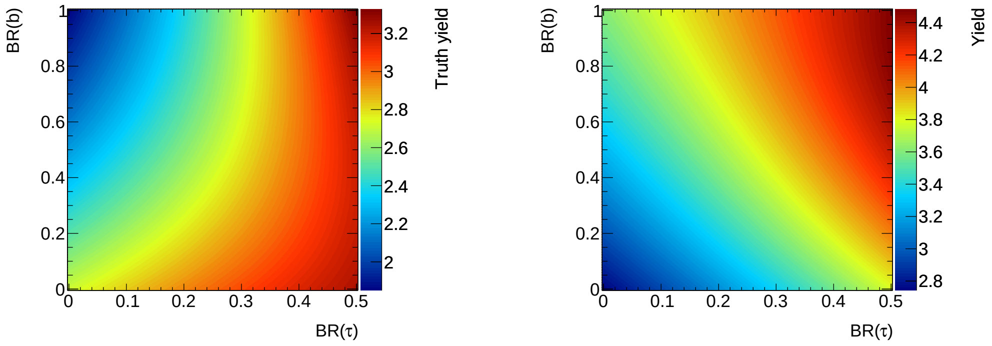

**(a)** [1000, 100], truth-level

**(b)** [1000, 100], with detector simulation

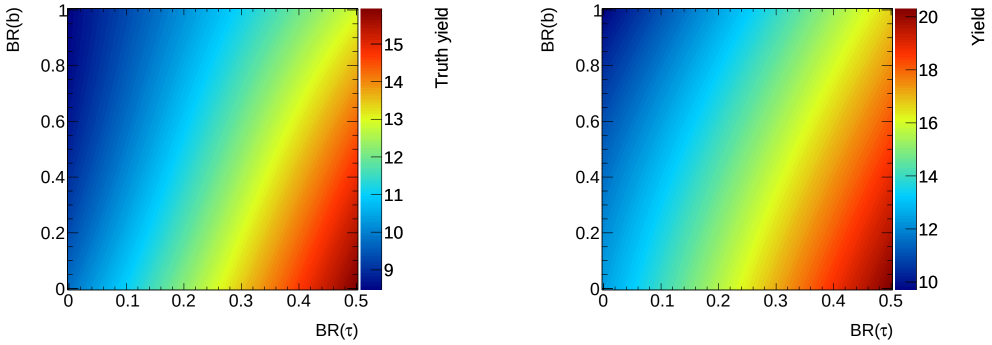

**(c)** [1000, 500], truth-level

**(d)** [1000, 500], with detector simulation

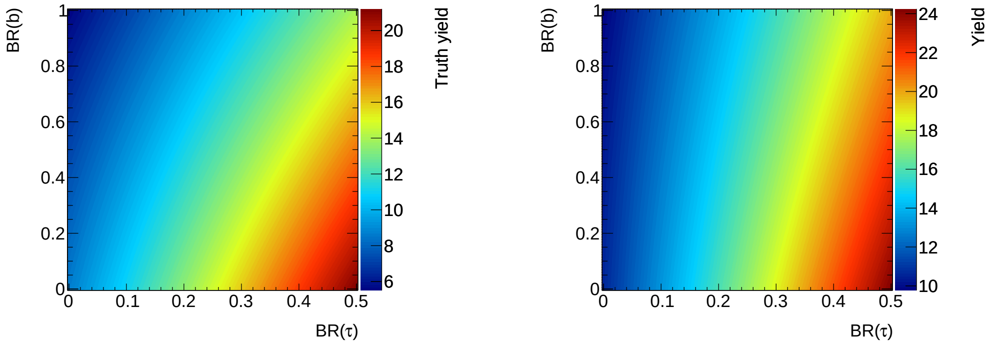

**(e)** [1000, 900], truth-level

**(f)** [1000, 900], with detector simulation

**Figure 5.29:** Expected numbers of signal events in the signal region ‘SR6jt+’ of the zero-lepton analysis at truth-level (left) and with detector simulation (right) for three mass points of the gluino model with $\lambda'$ couplings.

the lepton veto. The relative increase in yield ranges between 10% and 70%. Figure 5.29 also shows that the dependence of the signal yields on $\mathrm{BR}(b)$ is different before and after detector simulation in some cases. For the mass ratio $r = 0.1$ high values of $\mathrm{BR}(b)$ are clearly favoured after detector simulation. Signal yields with detector simulation for the other mass points of the gluino model with $\lambda'$ couplings can be found in appendix A.

The signal regions of the zero-lepton search are correlated and cannot be directly combined. Therefore, only the signal region with highest sensitivity is used separately for each point in the branching ratio square and each mass point to set limits. In order to avoid bias due to statistical fluctuations in the data, the signal regions are selected based on the expected limits instead of observed limits. All following results are derived from observed limits with the exception of the signal region selection.

The signal region 'SR6jt+' shows the highest sensitivity for almost the whole explored parameter space. At lower NLSP and LSP masses, other signal regions are preferred. 'SR6jl' is best for the [600, 60] mass point, 'SR6jm' for [800, 400] and 'SR5j' for [800, 720]. 'SR5j' is also preferred in the corner of the branching ratio square for [800, 80] with $\mathrm{BR}(b) = 0$ and $\mathrm{BR}(\tau) \leq 0.05$. One of the main differences between the various signal regions is the $m_{\mathrm{eff}}$ cut (see table 4.6). The impact of this cut is smaller for larger gluino masses as then $m_{\mathrm{eff}}$ is also larger. For $m(\tilde{g}) \geq 1.0$ TeV the signal yields in 'SR6jl' and 'SR6jm', which are distinguished only by the $m_{\mathrm{eff}}$ cut, differ only by few per cent. 'SR5j' prevails against 'SR6jl' and 'SR6jm' for [800, 720], because for $r = 0.9$ there are many events with five jets (see figure 5.12a). 'SR6jt+' has the best sensitivity for high masses because the lowest cut on the ratio $E_{\mathrm{T}}^{\mathrm{miss}}/m_{\mathrm{eff}}(N_j)$ is imposed and also has very low Standard Model background (see table 4.8). This argument is supported by the observation that 'SR6jt' is irrelevant for the gluino model with $\lambda'$ couplings even though it implies a lower $m_{\mathrm{eff}}$ cut than for 'SR6jt+' and the Standard Model background is of similar magnitude, but a much larger value for the ratio $E_{\mathrm{T}}^{\mathrm{miss}}/m_{\mathrm{eff}}(N_j)$ is required.

Figures 5.30 to 5.32 show the observed 95% CL cross-section upper limits for the 13 mass points considered. In the case of $r = 0.1$, the sensitivity across the branching ratio square varies significantly with NLSP mass. Most of the dependences on the branching ratios can be explained by the corresponding signal yields (see appendix A), but there are noticeable differences in few cases due to the acceptance uncertainty which is the dominant systematic uncertainty in this scenario. For the mass point [800, 80] in figure 5.30b, there is a small local maximum in the upper left corner of the branching ratio square which is

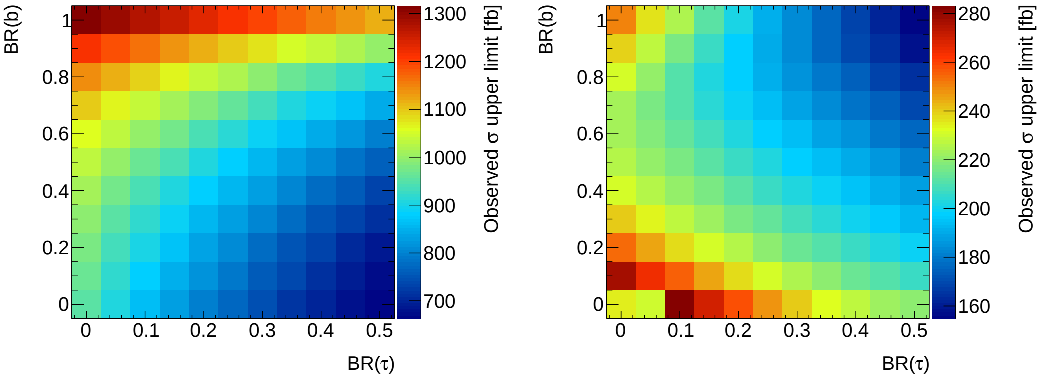

**(a)** [600, 60], SR6jl

**(b)** [800, 80], SR6jt+ and SR5j

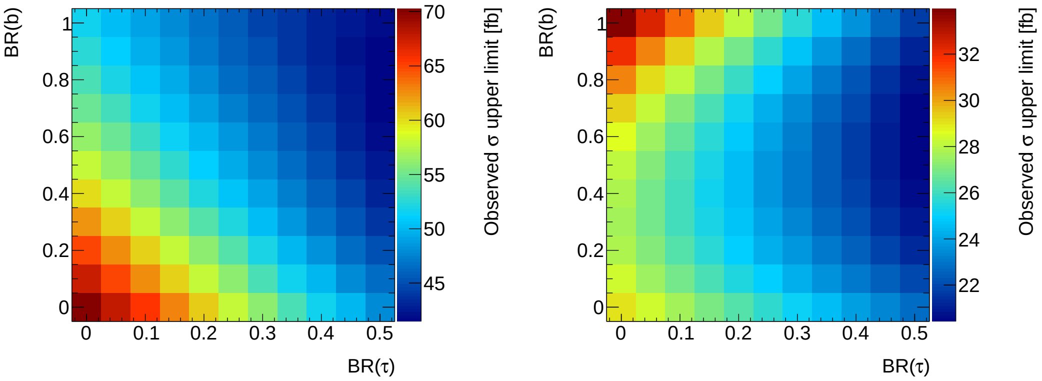

**(c)** [1000, 100], SR6jt+

**(d)** [1200, 120], SR6jt+

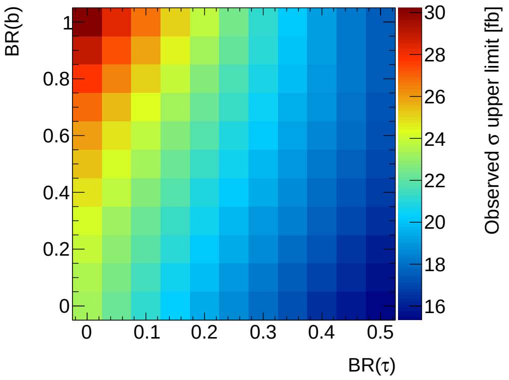

**(e)** [1400, 140], SR6jt+

**Figure 5.30:** Observed 95% CL upper limits on the signal cross-section of the gluino model with $\lambda'$ couplings for the mass points with a ratio $r = 0.1$ from the reinterpretation of the zero-lepton analysis.

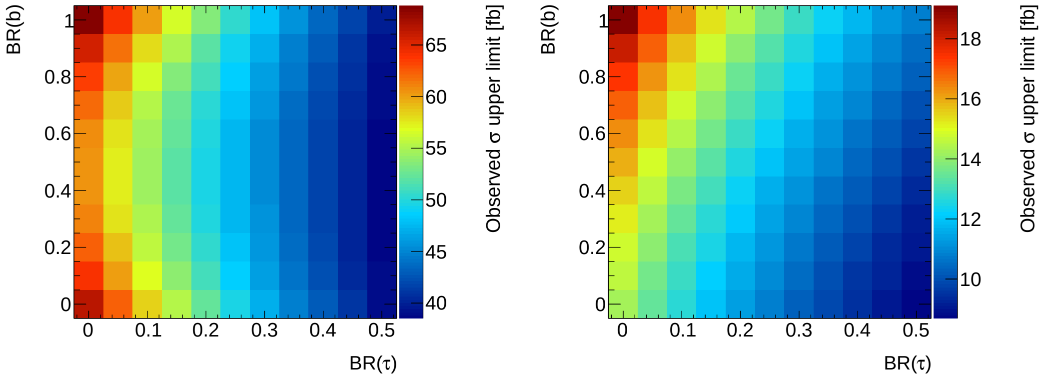

**(a)** [800, 400], SR6jm

**(b)** [1000, 500], SR6jt+

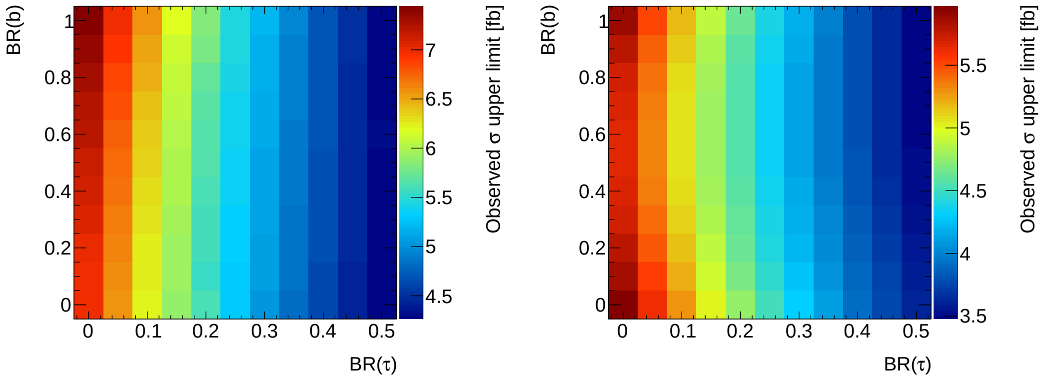

**(c)** [1200, 600], SR6jt+

**(d)** [1400, 700], SR6jt+

**Figure 5.31:** Observed 95% CL upper limits on the signal cross-section of the gluino model with $\lambda'$ couplings for the mass points with a ratio $r = 0.5$ from the reinterpretation of the zero-lepton analysis.

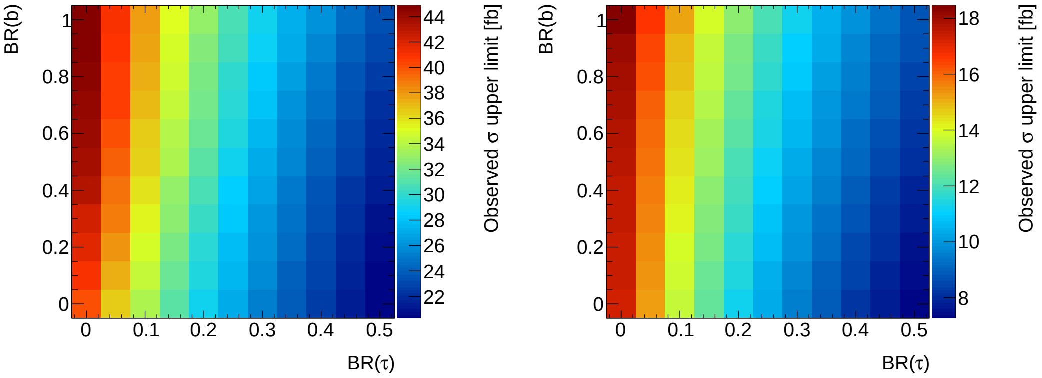

**(a)** [800, 720], SR5j

**(b)** [1000, 900], SR6jt+

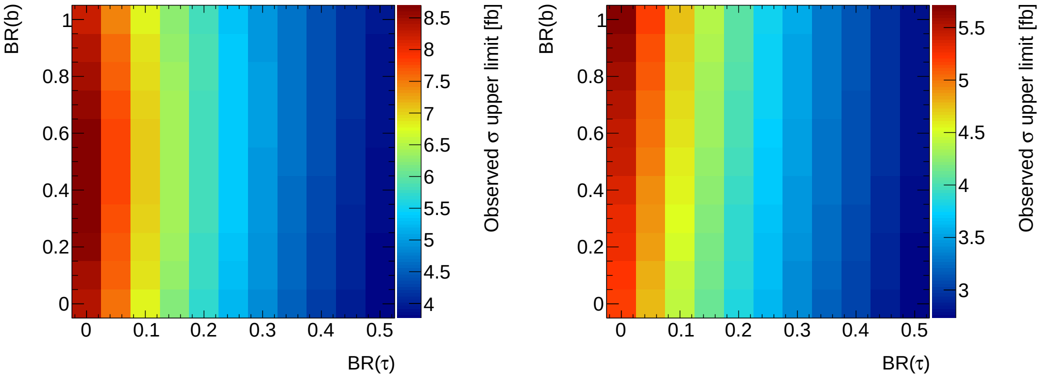

**(c)** [1200, 1080], SR6jt+

**(d)** [1400, 1260], SR6jt+

**Figure 5.32:** Observed 95% CL upper limits on the signal cross-section of the gluino model with $\lambda'$ couplings for the mass points with a ratio $r = 0.9$ from the reinterpretation of the zero-lepton analysis.

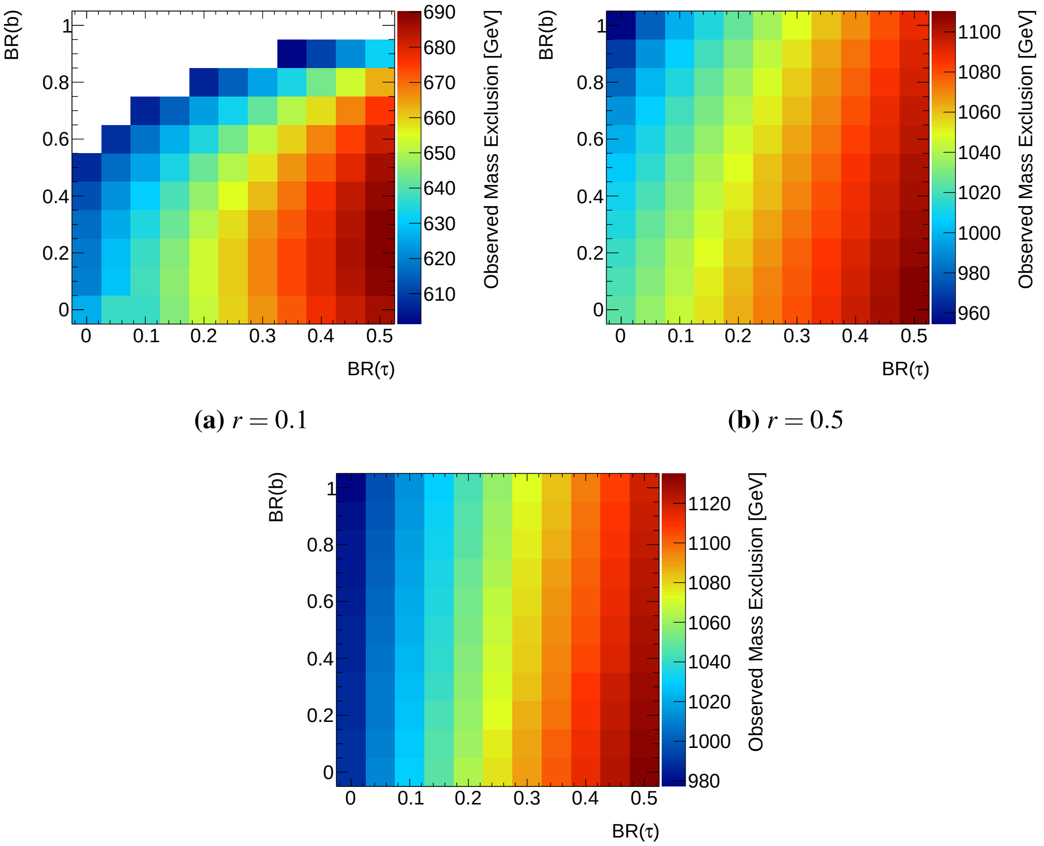

**(a)** $r = 0.1$

**(b)** $r = 0.5$

**(c)** $r = 0.9$

**Figure 5.33:** Observed 95% CL lower limits on the gluino mass of the gluino model with $\lambda'$ couplings for the three mass ratios $r$ from the reinterpretation of the zero-lepton analysis. The white areas in (a) indicate regions of the parameter space where the mass limit is below 600 GeV (see text).

due to the maximum of the acceptance uncertainty in the same region (see figure A.2b). Furthermore, there is a discontinuity in the observed upper limit at the origin of the square for this mass point which is due to the use of 'SR5j' in this region of parameter space as mentioned above. A small excess was measured in 'SR6jt+', but not in 'SR5j', leading to the observed discontinuity.

The observed cross-section upper limits for $r = 0.1$ improve substantially with increasing gluino mass. For $m(\tilde{g}) = 600$ GeV the best upper limit is 660 fb while for $m(\tilde{g}) = 1400$ GeV cross-sections down to 16 fb are excluded. The best upper limits are always obtained for $\mathrm{BR}(\tau) = 0.5$, but they depend strongly on $\mathrm{BR}(b)$ for $r = 0.1$. Also the limits at lower $\mathrm{BR}(\tau)$ depend strongly on $\mathrm{BR}(b)$. For the mass ratio $r = 0.5$ (see figure 5.31) the upper limits are substantially better and cross-sections down to 3.5 fb are excluded. The dependence on $\mathrm{BR}(b)$ is less strong than for $r = 0.1$, especially for $m(\tilde{g}) \geq 1200$ GeV. For $r = 0.9$ (see figure 5.32), however, the dependence on $\mathrm{BR}(b)$ is very weak. Cross-sections down to 2.7 fb are excluded. The cross-section limits for $r = 0.5$ and $r = 0.9$ decrease approximately with increasing $m(\tilde{g})$ in the range $m(\tilde{g}) \leq 1200$ GeV.

Figure 5.33 shows the observed 95% CL lower limits on the gluino mass for three mass ratios. The limits for $r = 0.5$ and $r = 0.9$ are similar, while they are much weaker, less than 690 GeV, for $r = 0.1$. This is related to the weaker cross-section limits in figure 5.30, and has a number of potential causes, discussed in section 5.2.1.2. In the white regions of the plots no explicit gluino mass exclusion limits can be set, because they would be below 600 GeV where no simulations have been performed as the truth-level studies in section 5.2.1.2 indicated that the multijet analysis [123] has a better sensitivity for $r = 0.1$. For $r = 0.5$ the limits range between 950 GeV and 1110 GeV and for $r = 0.9$ between 980 GeV and 1140 GeV. For all three mass ratios the best limits are obtained for $\mathrm{BR}(\tau) = 0.5$, because in this case the lepton veto is less efficient and the average number of jets per event is higher due to the hadronically decaying taus.

#### 5.3.3.3 The Squark Model with LQD Couplings

The analysis procedure for the squark model is the same as for the gluino model with $\lambda'$ couplings. Also in the squark model the signal yields of the zero-lepton analysis mostly increase after detector simulation (see figure 5.34) and depend less on $\mathrm{BR}(b)$ than the yields at truth-level. Signal yields with detector simulation for all mass points of the squark model can be found in appendix A.

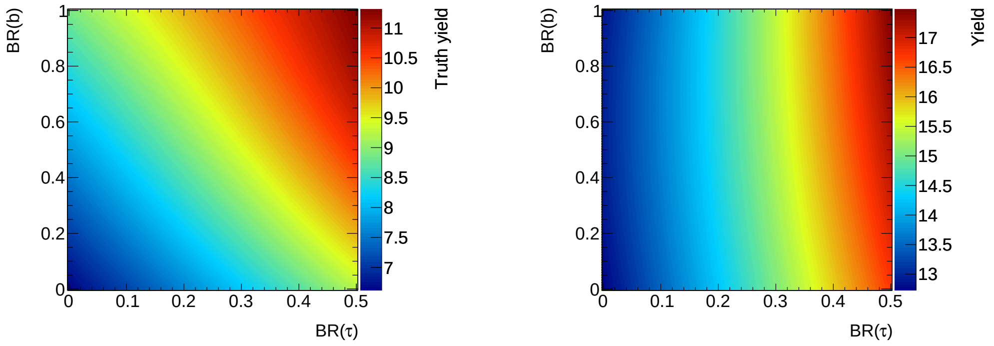

**(a)** [600, 60], SR5j, truth-level

**(b)** [600, 60], SR5j, with detector simulation

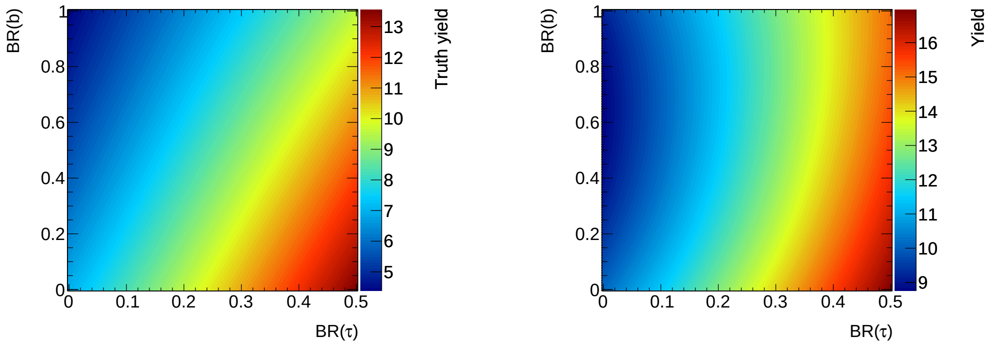

**(c)** [800, 400], SR6jt+, truth-level

**(d)** [800, 400], SR6jt+, with detector simulation

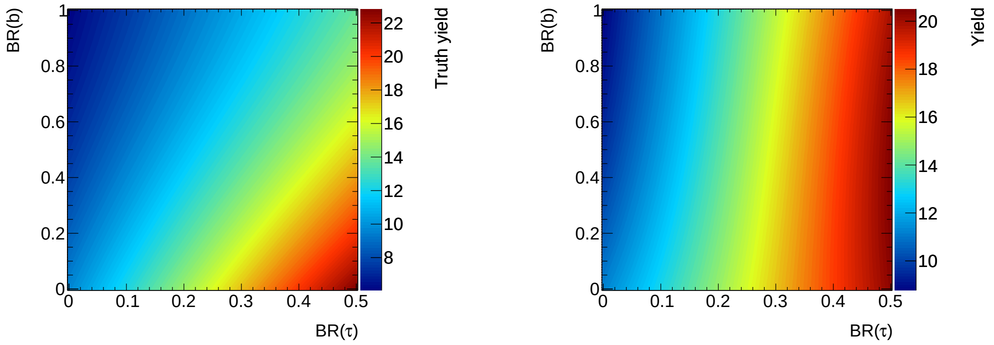

**(e)** [800, 720], SR6jt+, truth-level

**(f)** [800, 720], SR6jt+, with detector simulation

**Figure 5.34:** Expected numbers of signal events in the signal regions 'SR5j' and 'SR6jt+' of the zero-lepton analysis contributing to the final results at truth-level (left) and with detector simulation (right) for three mass points of the squark model.

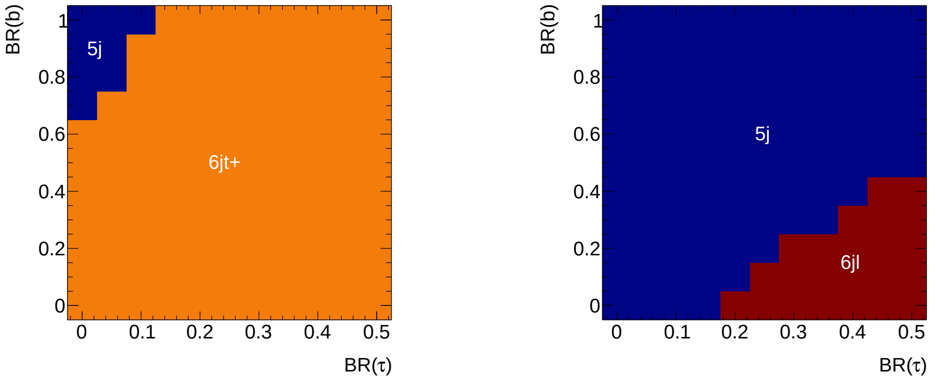

**(a)** [800, 720] **(b)** [600, 300]

**Figure 5.35:** The most sensitive signal regions of the zero-lepton analysis for two mass points of the squark model.

Again, the most sensitive signal region is individually selected for each point of the branching ratio square and each mass point. The discussion of the most sensitive signal regions for the gluino model with $\lambda'$ couplings in section 5.3.3.2 applies also here. For squark masses above 800 GeV, 'SR6jt+' provides the best sensitivity except for certain branching ratio choices at the mass points [800, 80] and [800, 720]. For [800, 80], 'SR5j' is better only at the origin of the branching ratio square, whereas for [800, 720] 'SR5j' provides better limits in a larger branching ratio range as shown in figure 5.35a. In the case of [600, 60], 'SR5j' is the most sensitive signal region over the whole square. The highest sensitivity for the mass point [600, 300] is split between the signal regions 'SR5j' and 'SR6jl' (see figure 5.35b) due to the fact that 'SR5j' and 'SR6jl' have similar signal yields over the whole square as well as a similar amount of Standard Model background. 'SR5j' is more relevant for the squark model than for the gluino model, because squark decays produce fewer jets than gluino decays.

Figures 5.36 to 5.38 show the observed 95% CL cross-section upper limits for three mass ratios. The plots for the mass points [600, 300] and [800, 720] show discontinuities due to the changes in the optimum signal region shown in figure 5.35. The limits for the squark model show similar behaviour as for the gluino model. The limits are again best for $\mathrm{BR}(\tau) = 0.5$ and worst for $\mathrm{BR}(\tau) = 0$. Furthermore, they improve substantially with increasing squark (NLSP) and neutralino (LSP) masses and depend less on $\mathrm{BR}(b)$ with increasing neutralino mass. For the mass point [1200, 1080] cross-sections down to 2.8 fb are excluded, while

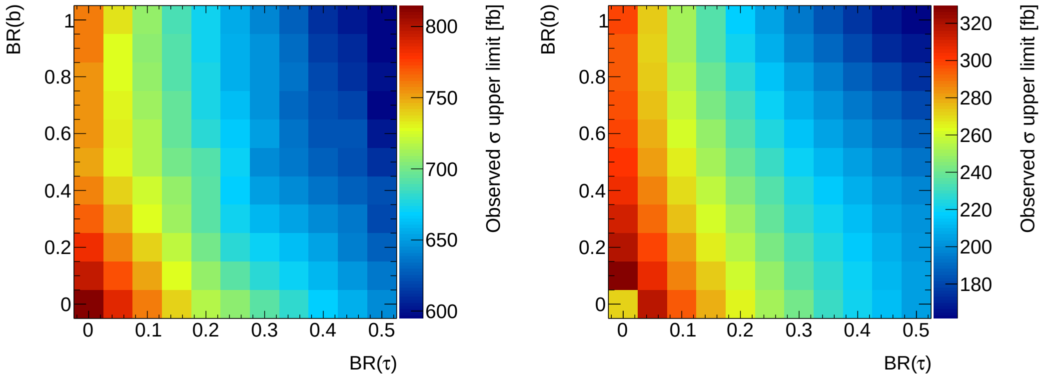

**(a)** [600, 60], SR5j **(b)** [800, 80], SR6jt+ and SR5j

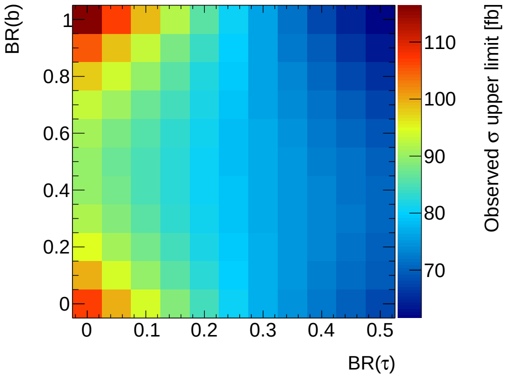

**(c)** [1000, 100], SR6jt+

**Figure 5.36:** Observed 95% CL upper limits on the signal cross-section of the squark model with $\lambda'$ couplings for the mass points with a ratio $r = 0.1$ from the reinterpretation of the zero-lepton analysis.

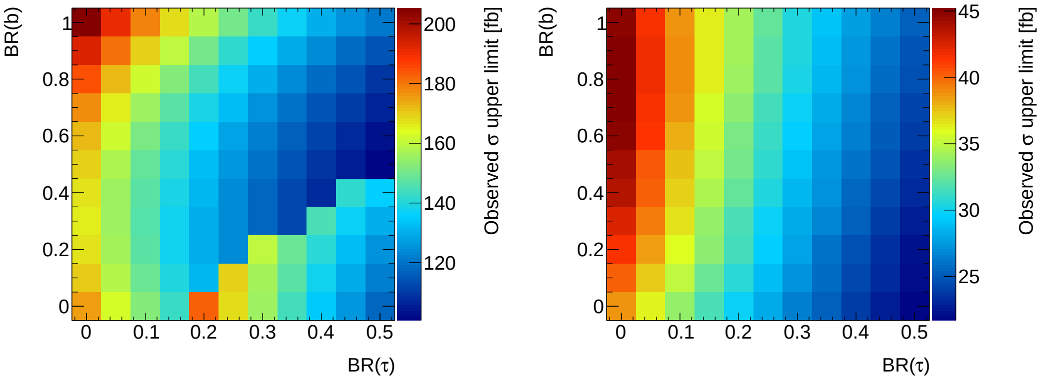

**(a)** [600, 300], SR5j and SR6jl

**(b)** [800, 400], SR6jt+

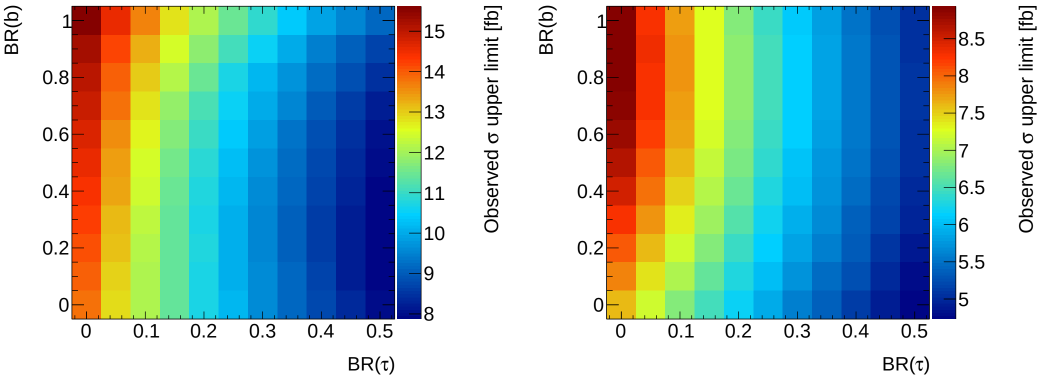

**(c)** [1000, 500], SR6jt+

**(d)** [1200, 600], SR6jt+

**Figure 5.37:** Observed 95% CL upper limits on the signal cross-section of the squark model with $\lambda'$ couplings for the mass points with a ratio $r = 0.5$ from the reinterpretation of the zero-lepton analysis.

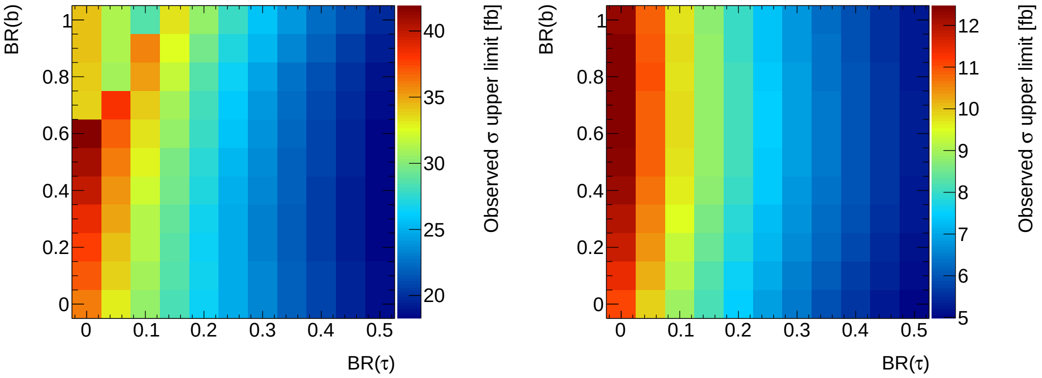

**(a)** [800, 720], SR6jt+ and SR5j

**(b)** [1000, 900], SR6jt+

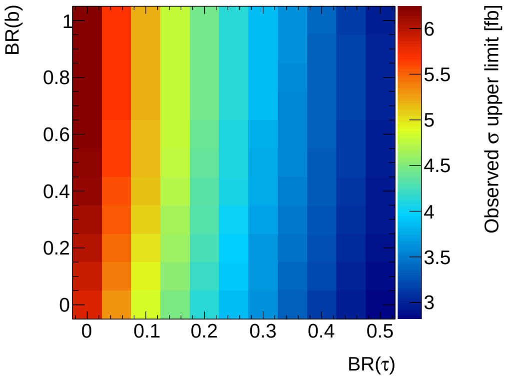

**(c)** [1200, 1080], SR6jt+

**Figure 5.38:** Observed 95% CL upper limits on the signal cross-section of the squark model with $\lambda'$ couplings for the mass points with a ratio $r = 0.9$ from the reinterpretation of the zero-lepton analysis.

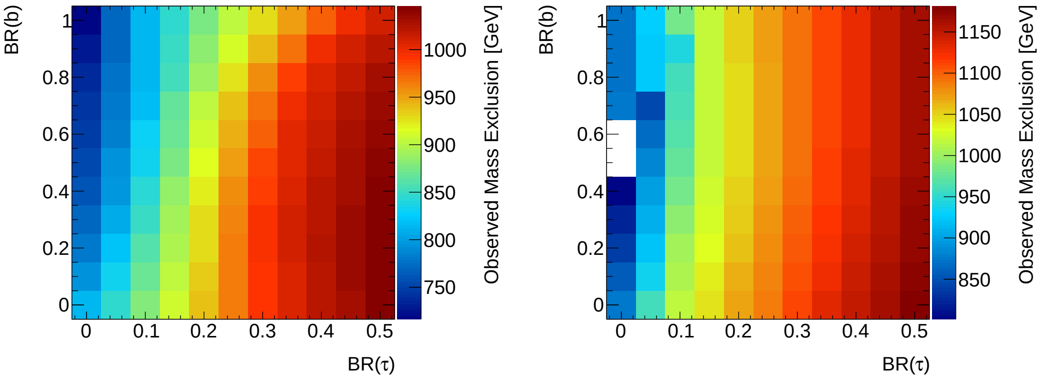

**(a)** $r = 0.5$

**(b)** $r = 0.9$

**Figure 5.39:** Observed 95% CL lower limits on the first and second generation squark masses of the squark model with $\lambda'$ couplings for the three mass ratios $r$ from the reinterpretation of the zero-lepton analysis. The white areas in (b) indicate regions of the parameter space where the mass limit is below 800 GeV (see text).

for [600, 60] only upper limits of 600 and 810 fb can be set at the upper right and lower left corners of the branching ratio square, respectively.

The zero-lepton analysis cannot set lower limits on the squark mass for $r = 0.1$ what is indicated by the fact that the signal yields in each signal region are far below the model-independent upper limits on the beyond-Standard-Model event yield in all cases. Figure 5.34b shows the number of signal events in ‘SR5j’ for the lowest mass point with $r = 0.1$. ‘SR5j’ is the most sensitive signal region at this mass point. The signal yields are $\leq 18$ events and thus much smaller than the model-independent upper limit of 35 events.

The constraints on the squark masses for the other two mass ratios are shown in figure 5.39. For $r = 0.5$ the limits range from 720 GeV to 1050 GeV, whereas for $r = 0.9$ they are significantly better, ranging from 800 GeV to 1180 GeV. Thus, the differences between the worst and best mass limits are more than twice as large as for the gluino model with $\lambda'$ couplings, where they are about 160 GeV. Since the dependence of the cross-section upper limits on $\mathrm{BR}(\tau)$ is similar for both models, this is due to a different dependence of the signal cross-sections and their upper limits on the NLSP masses. In the white regions of figure 5.39b no exclusion limits can be set, because the mass limit drops below 800 GeV. Mass points below that value were not simulated, since the truth-level studies in section 5.2.1.3 indicated that the one-lepton analysis has better sensitivity for low $\mathrm{BR}(\tau)$.

# Chapter 6

# Summary

In this thesis, three supersymmetric models with R-parity violation (RPV) have been investigated in which the lightest supersymmetric particle (LSP) decays via lepton-number violating $\lambda$ or $\lambda'$ couplings. In two of the models gluino pairs and in the third model first- and second-generation squarks with degenerate masses are produced. In contrast to most existing searches for RPV supersymmetry the assumption of a single dominant coupling was dropped and multiple simultaneous LSP decay channels were considered defined by a two-dimensional parameter space of the LSP decay branching ratios which has been completely scanned. The models were constrained by reinterpreting existing ATLAS searches for supersymmetry. Generator-level simulation studies identified five searches sensitive to the three signal models. Two of them have been used in this thesis to constrain the models.

Limits on the gluino model with $\lambda$ couplings were set using the four-lepton analysis. Gluino masses up to 1390 GeV are excluded at 95% CL, and cross-section upper limits down to 0.4 fb are placed. The two models with $\lambda'$ couplings were constrained using the zero-lepton analysis. In the gluino model with $\lambda'$ couplings, gluino masses up to 1140 GeV are excluded at 95% CL and cross-section upper limits down to 2.7 fb are placed. In the squark model with $\lambda'$ couplings, squark masses up to 1180 GeV are excluded, and cross-section upper limits down to 2.8 fb are placed.

One of the goals of the reinterpretation was to find holes in the coverage of the supersymmetry parameter space by the existing analyses. The studies of the two models with $\lambda'$ couplings revealed that small LSP masses are challenging. In the case of the squark model, no limits could be set for LSP masses below one-tenth of the squark mass. For the first time, RPV supersymmetric models with prompt LSP decays mediated by $\lambda'$ couplings have been constrained with ATLAS data. The studies show that searches optimised for R-parity conserving models, e.g. the zero-lepton analysis, can provide also excellent sensitivity to models with RPV.

# Appendix A

# Signal Yields and Acceptance Uncertainties

This chapter contains the numbers of signal events with detector simulation and the relative uncertainties in the acceptance of the zero-lepton search for all NLSP-LSP mass points of the two model with $\lambda'$ couplings. For each mass point, one signal region is considered which contributes to the final limits.

Signal yields in the ‘noZb’ signal regions of the four-lepton search for the gluino model with $\lambda$ couplings are not shown, because for each ‘noZb’ signal region, the dependences of its signal yields on the branching ratios of the LSP decay to left- and right-handed taus are very similar for all NLSP and LSP masses.

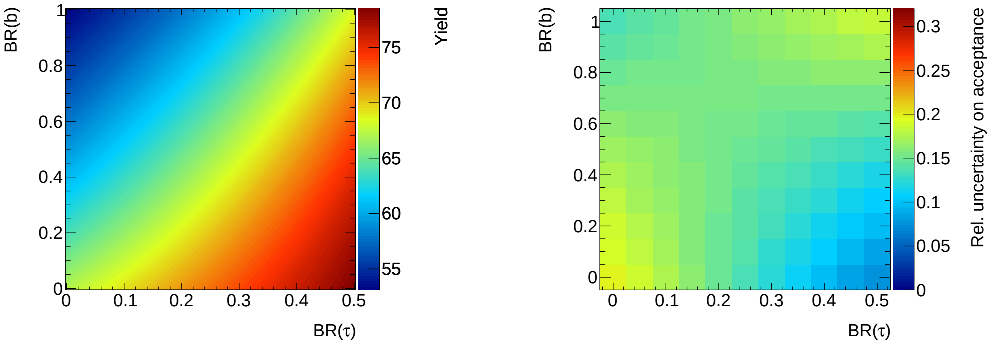

**(a)** [600, 60], SR6jl

**(b)** [600, 60], SR6jl

**Figure A.1:** Expected numbers of signal events with detector simulation (left) and relative uncertainty in the acceptance (right) of the signal region ‘SR6jl’ of the zero-lepton analysis for one mass point of the gluino model with $\lambda'$ couplings.

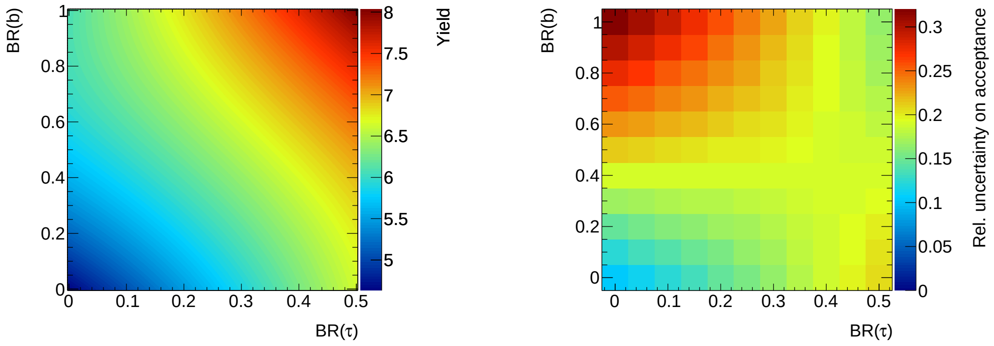

**(a)** [800, 80], SR6jt+

**(b)** [800, 80], SR6jt+

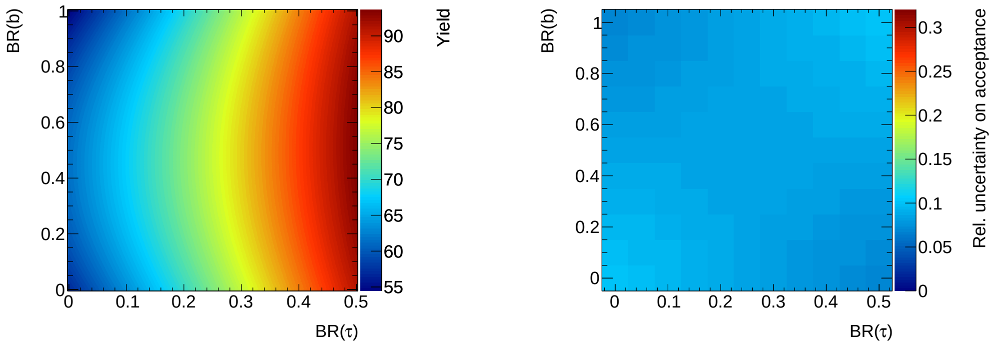

**(c)** [800, 400], SR6jm

**(d)** [800, 400], SR6jm

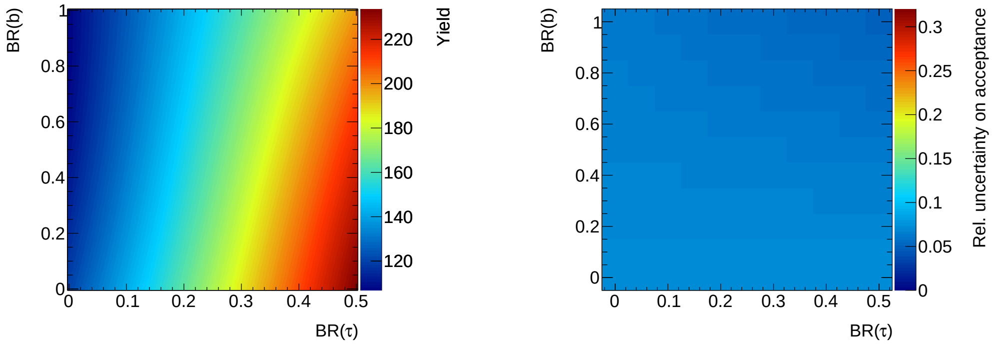

**(e)** [800, 720], SR5j

**(f)** [800, 720], SR5j

**Figure A.2:** Expected numbers of signal events with detector simulation (left) and relative uncertainty in the acceptance (right) of the most sensitive signal regions of the zero-lepton analysis for mass points with $m(\tilde{g}) = 800$ GeV of the gluino model with $\lambda'$ couplings.

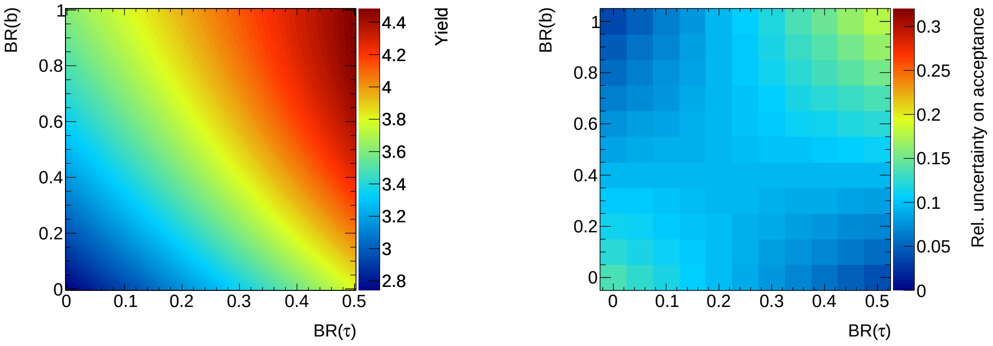

**(a)** [1000, 100], SR6jt+

**(b)** [1000, 100], SR6jt+

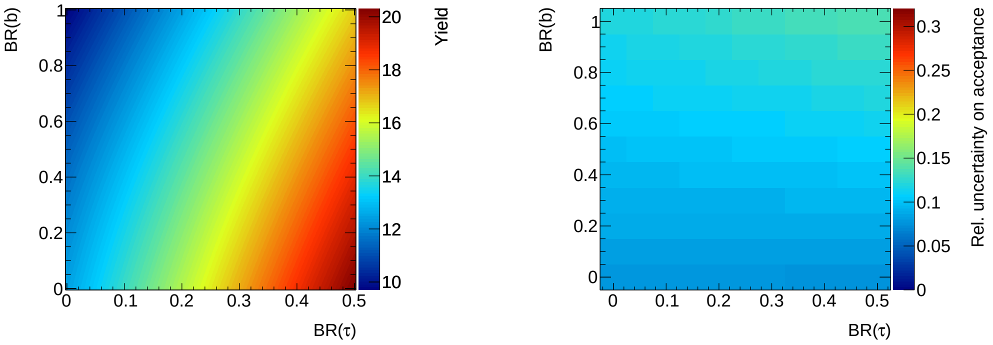

**(c)** [1000, 500], SR6jt+

**(d)** [1000, 500], SR6jt+

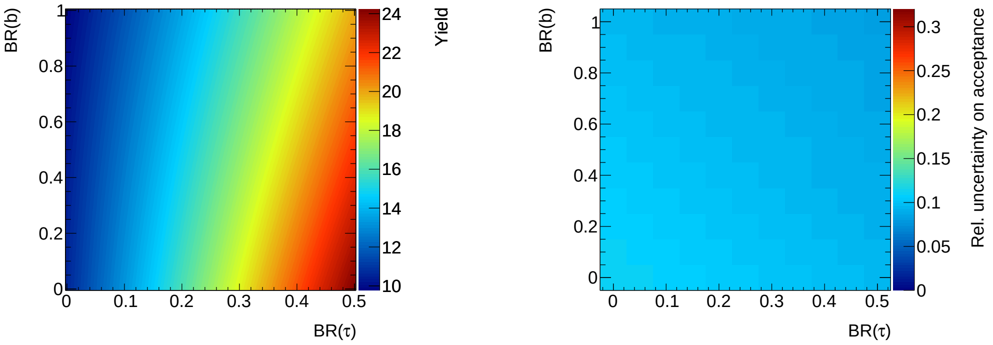

**(e)** [1000, 900], SR6jt+

**(f)** [1000, 900], SR6jt+

**Figure A.3:** Expected numbers of signal events with detector simulation (left) and relative uncertainty in the acceptance (right) of the signal region ‘SR6jt+’ of the zero-lepton analysis for mass points with $m(\tilde{g}) = 1.0$ TeV of the gluino model with $\lambda'$ couplings.

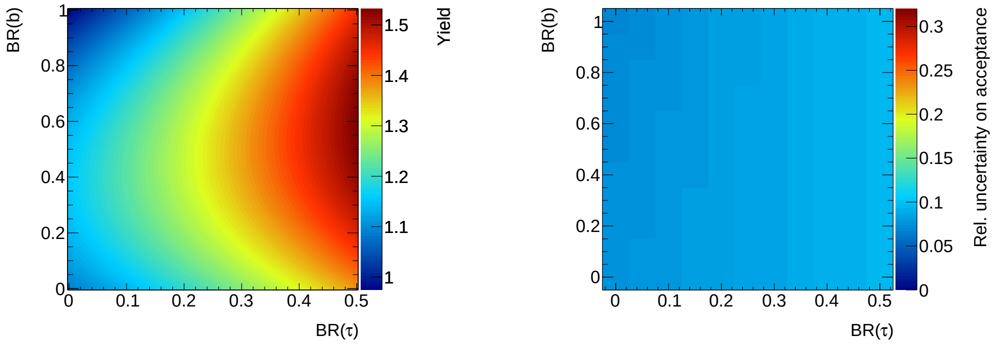

**(a)** [1200, 120], SR6jt+ **(b)** [1200, 120], SR6jt+

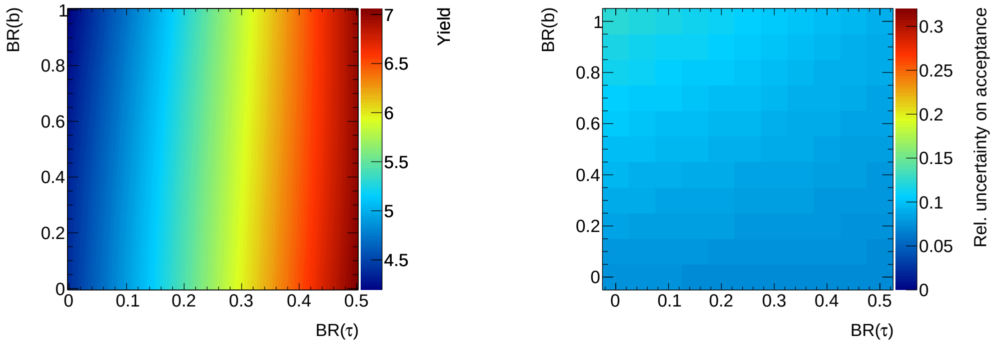

**(c)** [1200, 600], SR6jt+ **(d)** [1200, 600], SR6jt+

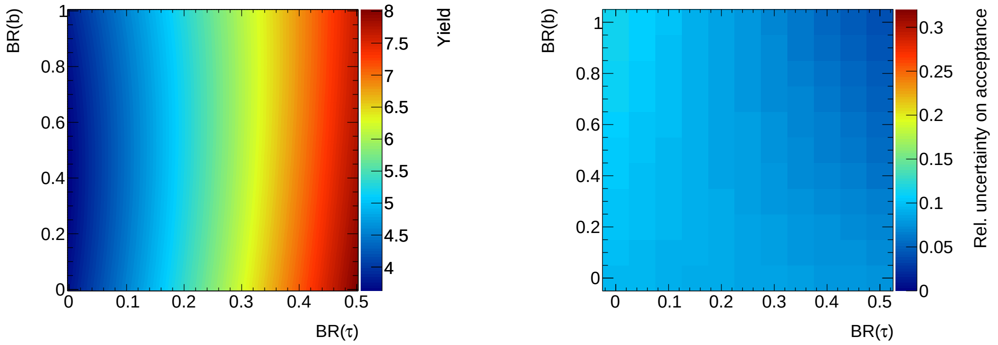

**(e)** [1200, 1080], SR6jt+ **(f)** [1200, 1080], SR6jt+

**Figure A.4:** Expected numbers of signal events with detector simulation (left) and relative uncertainty in the acceptance (right) of the signal region ‘SR6jt+’ of the zero-lepton analysis for mass points with $m(\tilde{g}) = 1.2$ TeV of the gluino model with $\lambda'$ couplings.

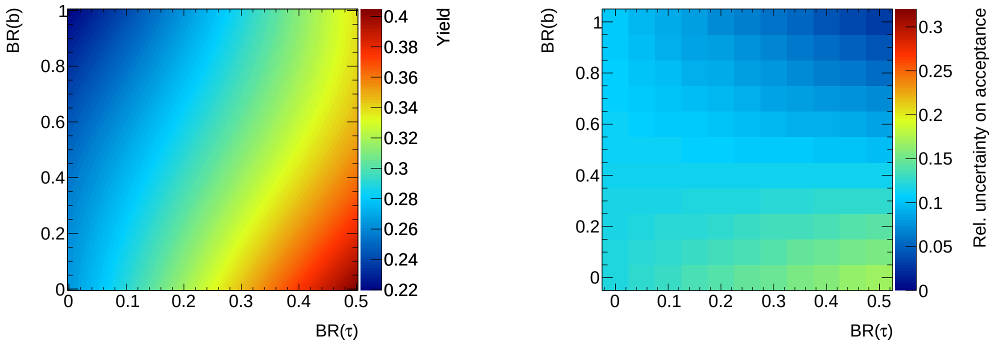

**(a)** [1400, 140], SR6jt+ **(b)** [1400, 140], SR6jt+

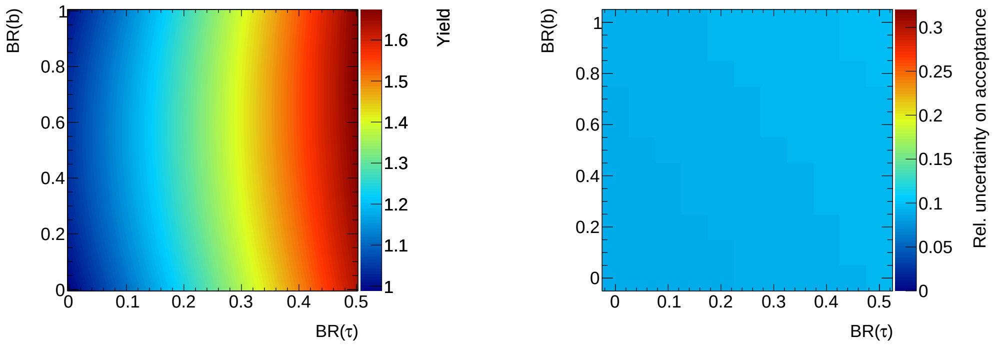

**(c)** [1400, 700], SR6jt+ **(d)** [1400, 700], SR6jt+

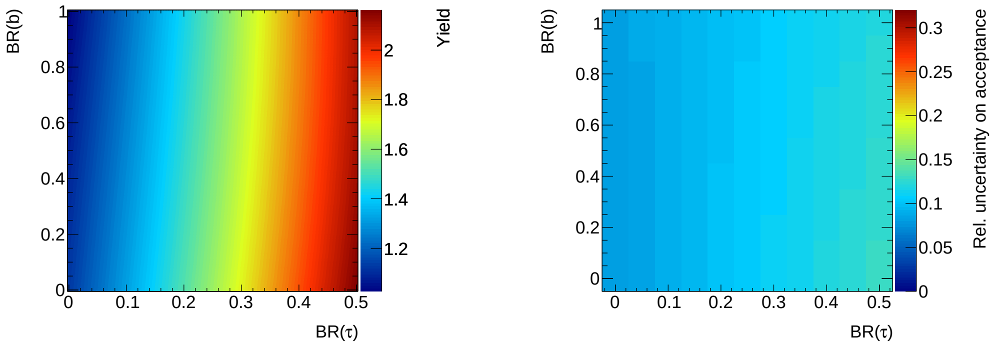

**(e)** [1400, 1260], SR6jt+ **(f)** [1400, 1260], SR6jt+

**Figure A.5:** Expected numbers of signal events with detector simulation (left) and relative uncertainty in the acceptance (right) of the signal region ‘SR6jt+’ of the zero-lepton analysis for mass points with $m(\tilde{g}) = 1.4$ TeV of the gluino model with $\lambda'$ couplings.

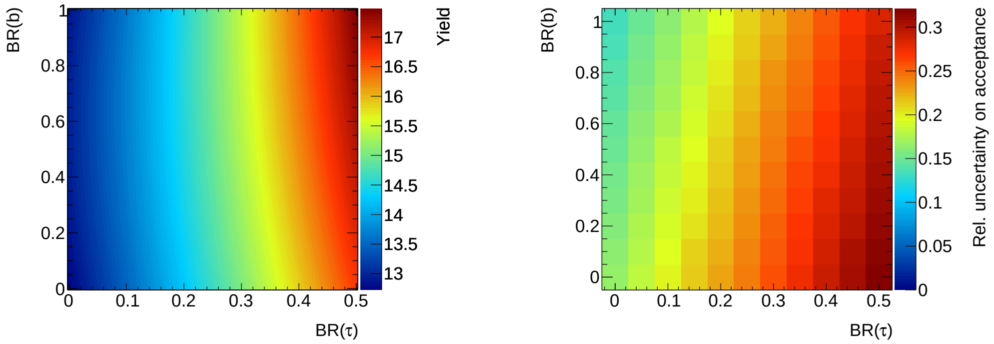

**(a)** [600, 60], SR5j **(b)** [600, 60], SR5j

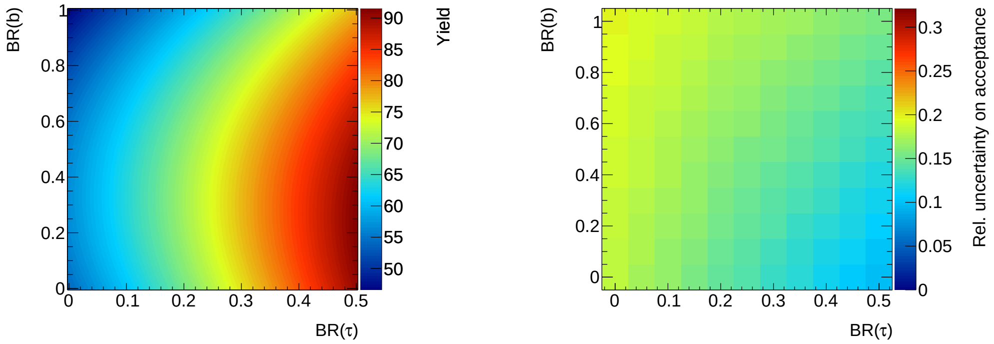

**(c)** [600, 300], SR5j **(d)** [600, 300], SR5j

**Figure A.6:** Expected numbers of signal events with detector simulation (left) and relative uncertainty in the acceptance (right) of the signal region ‘SR5j’ of the zero-lepton analysis for mass points with $m(\tilde{q}) = 600$ GeV of the squark model with $\lambda'$ couplings.

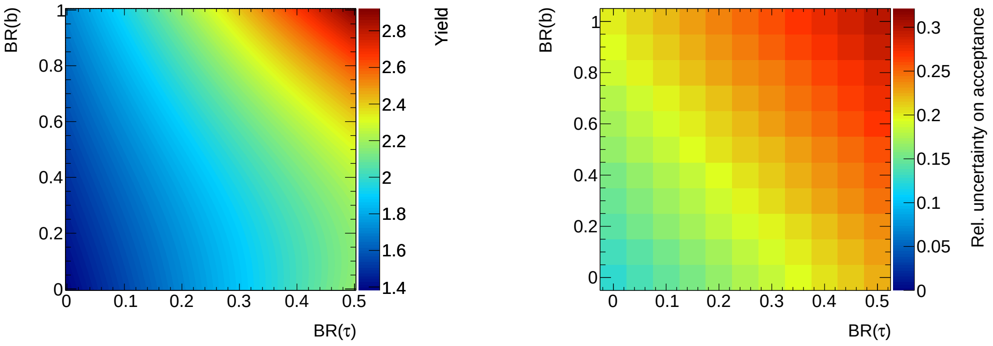

**(a)** [800, 80], SR6jt+ **(b)** [800, 80], SR6jt+

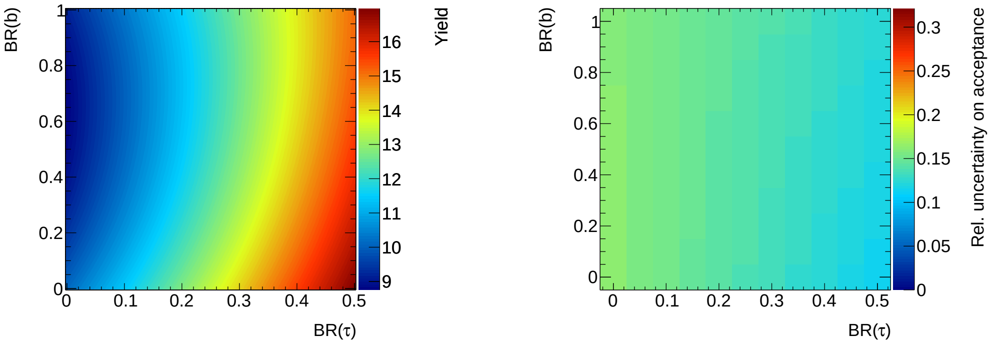

**(c)** [800, 400], SR6jt+ **(d)** [800, 400], SR6jt+

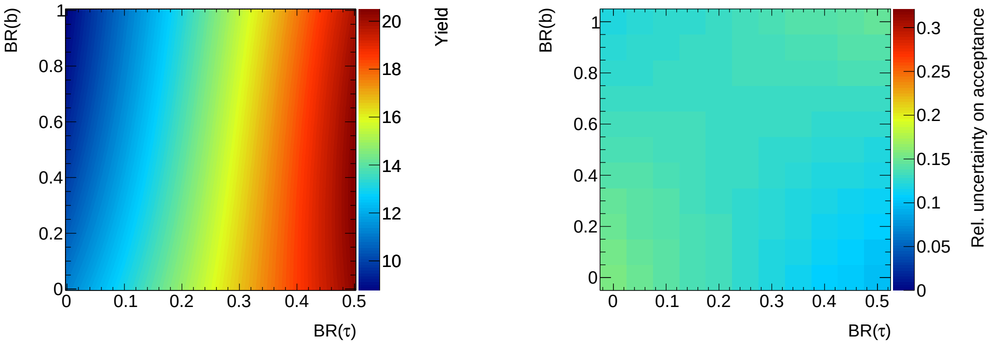

**(e)** [800, 720], SR6jt+ **(f)** [800, 720], SR6jt+

**Figure A.7:** Expected numbers of signal events with detector simulation (left) and relative uncertainty in the acceptance (right) of the signal region ‘SR6jt+’ of the zero-lepton analysis for mass points with $m(\tilde{q}) = 800$ GeV of the squark model with $\lambda'$ couplings.

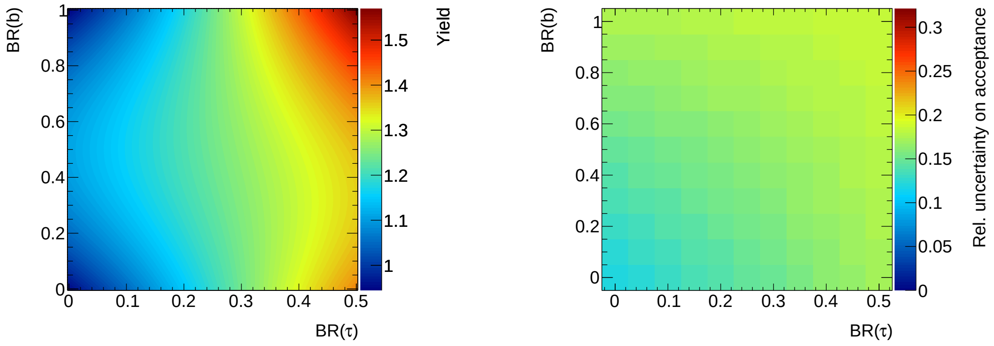

**(a)** [1000, 100], SR6jt+ **(b)** [1000, 100], SR6jt+

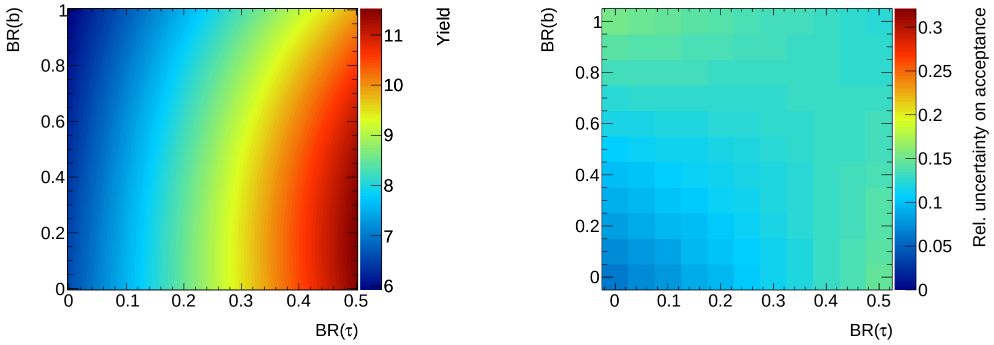

**(c)** [1000, 500], SR6jt+ **(d)** [1000, 500], SR6jt+

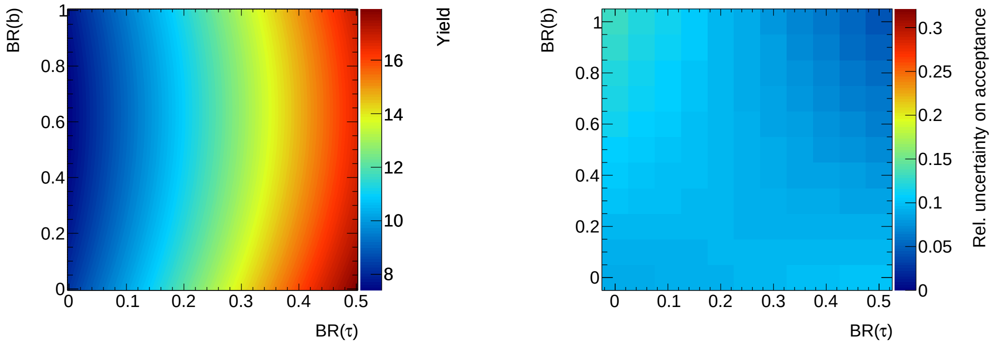

**(e)** [1000, 900], SR6jt+ **(f)** [1000, 900], SR6jt+

**Figure A.8:** Expected numbers of signal events with detector simulation (left) and relative uncertainty in the acceptance (right) of the signal region ‘SR6jt+’ of the zero-lepton analysis for mass points with $m(\tilde{q}) = 1.0$ TeV of the squark model with $\lambda'$ couplings.

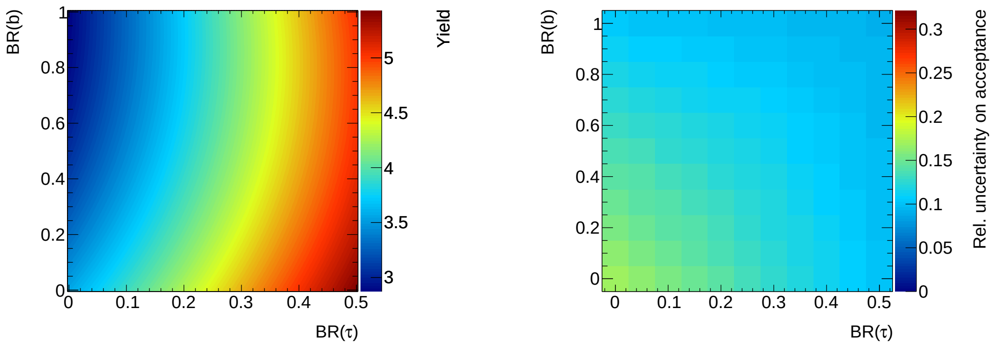

**(a)** [1200, 600], SR6jt+

**(b)** [1200, 600], SR6jt+

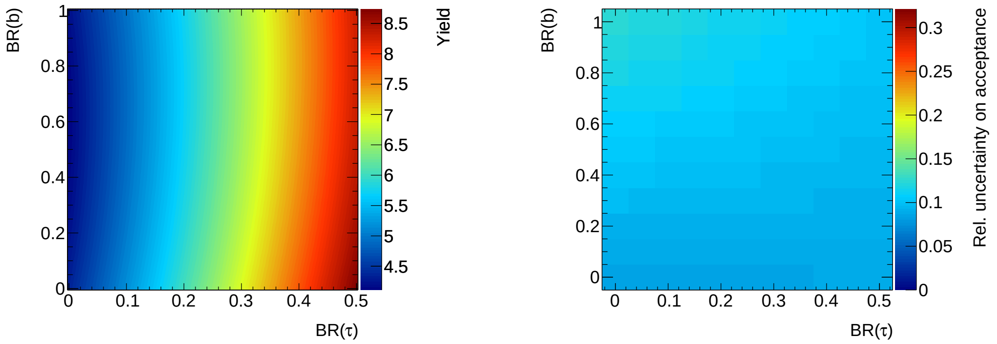

**(c)** [1200, 1080], SR6jt+

**(d)** [1200, 1080], SR6jt+

**Figure A.9:** Expected numbers of signal events with detector simulation (left) and relative uncertainty in the acceptance (right) of the signal region 'SR6jt+' of the zero-lepton analysis for each mass point with $m(\tilde{q}) = 1.2$ TeV of the squark model with $\lambda'$ couplings.

# Bibliography

[1] ATLAS Collaboration, *Observation of a new particle in the search for the Standard Model Higgs boson with the ATLAS detector at the LHC*, Phys. Lett. **B716** (2012) 1–29, `arXiv:1207.7214 [hep-ex]`.

[2] CMS Collaboration, *Observation of a new boson at a mass of 125 GeV with the CMS experiment at the LHC*, Phys. Lett. **B716** (2012) 30–61, `arXiv:1207.7235 [hep-ex]`.

[3] S. Weinberg, *The making of the Standard Model*, Eur. Phys. J. **C34** (2004) 5–13, `arXiv:hep-ph/0401010`.

[4] D. Hanneke, S. Fogwell, and G. Gabrielse, *New measurement of the electron magnetic moment and the fine structure constant*, Phys. Rev. Lett. **100** (2008) 120801, `arXiv:0801.1134 [physics.atom-ph]`.

[5] Wikipedia, *Standard Model*, `http://en.wikipedia.org/wiki/Standard_Model`.

[6] O. Eberhardt, G. Herbert, H. Lacker, A. Lenz, A. Menzel, et al., *Impact of a Higgs boson at a mass of 126 GeV on the Standard Model with three and four fermion generations*, Phys. Rev. Lett. **109** (2012) 241802, `arXiv:1209.1101 [hep-ph]`.

[7] ATLAS Collaboration, CDF Collaboration, CMS Collaboration, D0 Collaboration, *First combination of Tevatron and LHC measurements of the top-quark mass*, `arXiv:1403.4427 [hep-ex]`.

[8] R. Alkofer and J. Greensite, *Quark confinement: The hard problem of hadron physics*, J. Phys. **G34** (2007) S3, `arXiv:hep-ph/0610365`.

[9] P. W. Higgs, *Broken symmetries, massless particles and gauge fields*, Phys. Lett. **12** (1964) 132–133.

[10] P. W. Higgs, *Broken symmetries and the masses of gauge bosons*, Phys. Rev. Lett. **13** (1964) 508–509.

[11] F. Englert and R. Brout, *Broken symmetry and the mass of gauge vector mesons*, Phys. Rev. Lett. **13** (1964) 321–323.

[12] G. S. Guralnik, C. R. Hagen, and T. W. B. Kibble, *Global conservation laws and massless particles*, Phys. Rev. Lett. **13** (1964) 585–587.

[13] ATLAS Collaboration, *Measurement of the Higgs boson mass from the* $H \to \gamma\gamma$ *and* $H \to ZZ^* \to 4\ell$ *channels with the ATLAS detector using 25* $fb^{-1}$ *of pp collision data*, Phys. Rev. **D90** (2014) 052004, `arXiv:1406.3827 [hep-ex]`.

[14] CMS Collaboration, *Precise determination of the mass of the Higgs boson and tests of compatibility of its couplings with the Standard Model predictions using proton collisions at 7 and 8 TeV*, `arXiv:1412.8662 [hep-ex]`.

[15] R. Davis, D. S. Harmer, and K. C. Hoffman, *Search for neutrinos from the sun*, Phys. Rev. Lett. **20** (1968) 1205–1209.

[16] SNO Collaboration, *Measurement of the rate of* $\nu_e + d \to p + p + e^-$ *interactions produced by* $^8B$ *solar neutrinos at the Sudbury Neutrino Observatory*, Phys. Rev. Lett. **87** (2001) 071301, `arXiv:nucl-ex/0106015`.

[17] Super-Kamiokande Collaboration, *Evidence for oscillation of atmospheric neutrinos*, Phys. Rev. Lett. **81** (1998) 1562–1567, `arXiv:hep-ex/9807003`.

[18] KamLAND Collaboration, *First results from KamLAND: Evidence for reactor anti-neutrino disappearance*, Phys. Rev. Lett. **90** (2003) 021802, `arXiv:hep-ex/0212021`.

[19] K2K Collaboration, *Measurement of neutrino oscillation by the K2K experiment*, Phys. Rev. **D74** (2006) 072003, `arXiv:hep-ex/0606032`.

[20] Particle Data Group, *Review of particle physics*, Chin. Phys. **C38** (2014) 090001.

[21] F. Zwicky, *Die Rotverschiebung von extragalaktischen Nebeln*, Helv. Phys. Acta **6** (1933) 110–127.

[22] Planck Collaboration, *Planck 2013 results. I. Overview of products and scientific results*, Astron. Astrophys. **571** (2014) A1, `arXiv:1303.5062 [astro-ph.CO]`.

[23] LUX Collaboration, *First results from the LUX dark matter experiment at the Sanford underground research facility*, Phys. Rev. Lett. **112** (2014) 091303, `arXiv:1310.8214 [astro-ph.CO]`.

[24] XENON100 Collaboration, *Dark matter results from 225 live days of XENON100 data*, Phys. Rev. Lett. **109** (2012) 181301, `arXiv:1207.5988 [astro-ph.CO]`.

[25] SuperCDMS Collaboration, *Search for low-mass WIMPs with SuperCDMS*, Phys. Rev. Lett. **112** (2014) 241302, `arXiv:1402.7137 [hep-ex]`.

[26] M. Cirelli, *Indirect searches for dark matter: A status review*, Pramana **79** (2012) 1021–1043, `arXiv:1202.1454 [hep-ph]`.

[27] AMS Collaboration, *Electron and positron fluxes in primary cosmic rays measured with the Alpha Magnetic Spectrometer on the International Space Station*, Phys. Rev. Lett. **113** (2014) 121102.

[28] ATLAS Collaboration, *Search for new phenomena in final states with an energetic jet and large missing transverse momentum in pp collisions at $\sqrt{s} = 8$ TeV with the ATLAS detector*, `arXiv:1502.01518 [hep-ex]`.

[29] ATLAS Collaboration, *Search for new phenomena in events with a photon and missing transverse momentum in pp collisions at $\sqrt{s} = 8$ TeV with the ATLAS detector*, Phys. Rev. **D91** (2015) 012008, `arXiv:1411.1559 [hep-ex]`.

[30] ATLAS Collaboration, *Search for new particles in events with one lepton and missing transverse momentum in pp collisions at $\sqrt{s} = 8$ TeV with the ATLAS detector*, JHEP **1409** (2014) 037, `arXiv:1407.7494 [hep-ex]`.

[31] CMS Collaboration, *Search for dark matter, extra dimensions, and unparticles in monojet events in proton-proton collisions at $\sqrt{s} = 8$ TeV*, `arXiv:1408.3583 [hep-ex]`.

[32] CMS Collaboration, *Search for new phenomena in monophoton final states in proton-proton collisions at $\sqrt{s} = 8$ TeV*, `arXiv:1410.8812 [hep-ex]`.

[33] CMS Collaboration, *Search for physics beyond the standard model in final states with a lepton and missing transverse energy in proton-proton collisions at* $\sqrt{s} = 8$ *TeV*, arXiv:1408.2745 [hep-ex].

[34] M. S. Turner, *Dark matter and energy in the universe*, Phys. Scripta **T85** (2000) 210–220, arXiv:astro-ph/9901109.

[35] Supernova Search Team Collaboration, A. G. Riess et al., *Observational evidence from supernovae for an accelerating universe and a cosmological constant*, Astron. J. **116** (1998) 1009–1038, arXiv:astro-ph/9805201.

[36] Supernova Cosmology Project Collaboration, S. Perlmutter et al., *Measurements of* $\Omega$ *and* $\Lambda$ *from 42 high redshift supernovae*, Astrophys. J. **517** (1999) 565–586, arXiv:astro-ph/9812133.

[37] A. Einstein, *Die Grundlage der allgemeinen Relativitätstheorie*, Ann. Phys. (Berlin) **354** (1916) 769–822.

[38] R. P. Woodard, *How far are we from the quantum theory of gravity?*, Rept. Prog. Phys. **72** (2009) 126002, arXiv:0907.4238 [gr-qc].

[39] S. Weinberg, *Implications of dynamical symmetry breaking*, Phys. Rev. **D13** (1976) 974–996.

[40] E. Gildener, *Gauge symmetry hierarchies*, Phys. Rev. **D14** (1976) 1667.

[41] S. Weinberg, *Implications of dynamical symmetry breaking: An addendum*, Phys. Rev. **D19** (1979) 1277–1280.

[42] L. Susskind, *Dynamics of spontaneous symmetry breaking in the Weinberg- Salam theory*, Phys. Rev. **D20** (1979) 2619–2625.

[43] D. B. Kaplan and H. Georgi, *SU(2) x U(1) breaking by vacuum misalignment*, Phys. Lett. **B136** (1984) 183.

[44] D. B. Kaplan, H. Georgi, and S. Dimopoulos, *Composite higgs scalars*, Phys. Lett. **B136** (1984) 187.

[45] N. Arkani-Hamed, S. Dimopoulos, and G. R. Dvali, *The Hierarchy problem and new dimensions at a millimeter*, Phys. Lett. **B429** (1998) 263–272, `arXiv:hep-ph/9803315`.

[46] S. Dimopoulos and H. Georgi, *Softly broken supersymmetry and SU(5)*, Nucl. Phys. **B193** (1981) 150.

[47] E. Witten, *Dynamical breaking of supersymmetry*, Nucl. Phys. **B188** (1981) 513.

[48] M. Dine, W. Fischler, and M. Srednicki, *Supersymmetric technicolor*, Nucl. Phys. **B189** (1981) 575–593.

[49] S. Dimopoulos and S. Raby, *Supercolor*, Nucl. Phys. **B192** (1981) 353.

[50] N. Sakai, *Naturalness in supersymmetric GUTs*, Zeit. Phys. **C11** (1981) 153.

[51] R. K. Kaul and P. Majumdar, *Cancellation of quadratically divergent mass corrections in globally supersymmetric spontaneously broken gauge theories*, Nucl. Phys. **B199** (1982) 36.

[52] H. Miyazawa, *Baryon number changing currents*, Prog. Theor. Phys. **36 (6)** (1966) 1266–1276.

[53] P. Ramond, *Dual theory for free fermions*, Phys. Rev. **D3** (1971) 2415–2418.

[54] Y. A. Gol'fand and E. P. Likhtman, *Extension of the algebra of Poincare group generators and violation of P invariance*, JETP Lett. **13** (1971) 323–326, [Pisma Zh. Eksp. Teor. Fiz. 13 (1971) 452-455].

[55] A. Neveu and J. H. Schwarz, *Factorizable dual model of pions*, Nucl. Phys. **B31** (1971) 86–112.

[56] A. Neveu and J. H. Schwarz, *Quark model of dual pions*, Phys. Rev. **D4** (1971) 1109–1111.

[57] J. L. Gervais and B. Sakita, *Field theory interpretation of supergauges in dual models*, Nucl. Phys. **B34** (1971) 632–639.

[58] D. V. Volkov and V. P. Akulov, *Is the neutrino a goldstone particle?*, Phys. Lett. **B46** (1973) 109–110.

[59] J. Wess and B. Zumino, *A Lagrangian model invariant under supergauge transformations*, Phys. Lett. **B49** (1974) 52.

[60] J. Wess and B. Zumino, *Supergauge transformations in four-dimensions*, Nucl. Phys. **B70** (1974) 39–50.

[61] R. Haag, J. T. Lopuszanski, and M. Sohnius, *All possible generators of supersymmetries of the S-matrix*, Nucl. Phys. **B88** (1975) 257.

[62] A. H. Chamseddine, R. L. Arnowitt, and P. Nath, *Locally supersymmetric grand unification*, Phys. Rev. Lett. **49** (1982) 970.

[63] R. Barbieri, S. Ferrara, and C. A. Savoy, *Gauge models with spontaneously broken local supersymmetry*, Phys. Lett. **B119** (1982) 343.

[64] L. E. Ibanez, *Locally supersymmetric SU(5) grand unification*, Phys. Lett. **B118** (1982) 73.

[65] L. J. Hall, J. D. Lykken, and S. Weinberg, *Supergravity as the messenger of supersymmetry breaking*, Phys. Rev. **D27** (1983) 2359–2378.

[66] N. Ohta, *Grand unified theories based on local supersymmetry*, Prog. Theor. Phys. **70** (1983) 542.

[67] G. L. Kane, C. F. Kolda, L. Roszkowski, and J. D. Wells, *Study of constrained minimal supersymmetry*, Phys. Rev. **D49** (1994) 6173–6210.

[68] P. Fayet, *Supersymmetry and weak, electromagnetic and strong interactions*, Phys. Lett. **B64** (1976) 159.

[69] P. Fayet, *Spontaneously broken supersymmetric theories of weak, electromagnetic and strong interactions*, Phys. Lett. **B69** (1977) 489.

[70] G. R. Farrar and P. Fayet, *Phenomenology of the production, decay, and detection of new hadronic states associated with supersymmetry*, Phys. Lett. **B76** (1978) 575–579.

[71] P. Fayet, *Relations between the masses of the superpartners of leptons and quarks, the goldstino couplings and the neutral currents*, Phys. Lett. **B84** (1979) 416.

[72] Michael Flowerdew, *Personal communication*.

[73] C. S. Wu, E. Ambler, R. W. Hayward, D. D. Hoppes, and R. P. Hudson, *Experimental test of parity conservation in beta decay*, Phys. Rev. **105** (1957) 1413–1414.

[74] R. L. Garwin, L. M. Lederman, and M. Weinrich, *Observations of the failure of conservation of parity and charge conjugation in meson decays: The magnetic moment of the free muon*, Phys. Rev. **105** (1957) 1415–1417.

[75] S. Dimopoulos, S. Raby, and F. Wilczek, *Supersymmetry and the scale of unification*, Phys. Rev. **D24** (1981) 1681–1683.

[76] L. E. Ibanez and G. G. Ross, *Low-energy predictions in supersymmetric grand unified theories*, Phys. Lett. **B105** (1981) 439.

[77] M. B. Einhorn and D. R. T. Jones, *The weak mixing angle and unification mass in supersymmetric SU(5)*, Nucl. Phys. **B196** (1982) 475.

[78] W. J. Marciano and G. Senjanovic, *Predictions of supersymmetric grand unified theories*, Phys. Rev. **D25** (1982) 3092.

[79] C. Giunti, C. W. Kim, and U. W. Lee, *Running coupling constants and grand unification models*, Mod. Phys. Lett. **A6** (1991) 1745–1755.

[80] J. R. Ellis, S. Kelley, and D. V. Nanopoulos, *Probing the desert using gauge coupling unification*, Phys. Lett. **B260** (1991) 131–137.

[81] U. Amaldi, W. de Boer, and H. Furstenau, *Comparison of grand unified theories with electroweak and strong coupling constants measured at LEP*, Phys. Lett. **B260** (1991) 447–455.

[82] P. Langacker and M.-X. Luo, *Implications of precision electroweak experiments for* $M(t)$*,* $\rho(0)$*,* $\sin^2\theta_W$ *and grand unification*, Phys. Rev. **D44** (1991) 817–822.

[83] D. I. Kazakov, *Beyond the standard model: In search of supersymmetry*, `arXiv:hep-ph/0012288`.

[84] Super-Kamiokande Collaboration, *Search for proton decay via* $p \to e^+\pi^0$ *and* $p \to \mu^+\pi^0$ *in a large water Cherenkov detector*, Phys. Rev. Lett. **102** (2009) 141801, `arXiv:0903.0676 [hep-ex]`.

[85] H. Goldberg, *Constraint on the photino mass from cosmology*, Phys. Rev. Lett. **50** (1983) 1419.

[86] J. R. Ellis, J. S. Hagelin, D. V. Nanopoulos, K. A. Olive, and M. Srednicki, *Supersymmetric relics from the big bang*, Nucl. Phys. **B238** (1984) 453–476.

[87] M. L. Perl, P. C. Kim, V. Halyo, E. R. Lee, I. T. Lee, et al., *The search for stable, massive, elementary particles*, Int. J. Mod. Phys. **A16** (2001) 2137–2164, `arXiv:hep-ex/0102033`.

[88] S. P. Ahlen, F. T. Avignone, R. L. Brodzinski, A. K. Drukier, G. Gelmini, et al., *Limits on cold dark matter candidates from an ultralow background germanium spectrometer*, Phys. Lett. **B195** (1987) 603–608.

[89] D. O. Caldwell, R. M. Eisberg, D. M. Grumm, M. S. Witherell, B. Sadoulet, et al., *Laboratory limits on galactic cold dark matter*, Phys. Rev. Lett. **61** (1988) 510.

[90] M. Beck, F. Bensch, J. Bockholt, G. Heusser, H. V. Klapdor-Kleingrothaus, et al., *Searching for dark matter with the enriched detectors of the Heidelberg - Moscow double beta decay experiment*, Phys. Lett. **B336** (1994) 141–146.

[91] R. Barbier, C. Berat, M. Besancon, M. Chemtob, A. Deandrea, et al., *R-parity violating supersymmetry*, Phys. Rept. **420** (2005) 1–202, `arXiv:hep-ph/0406039`.

[92] A. D. Sakharov, *Violation of CP invariance, C asymmetry, and baryon asymmetry of the universe*, Pisma Zh. Eksp. Teor. Fiz. **5** (1967) 32–35.

[93] L. E. Ibanez and G. G. Ross, *Discrete gauge symmetry anomalies*, Phys. Lett. **B260** (1991) 291–295.

[94] L. E. Ibanez and G. G. Ross, *Discrete gauge symmetries and the origin of baryon and lepton number conservation in supersymmetric versions of the standard model*, Nucl. Phys. **B368** (1992) 3–37.

[95] H. K. Dreiner, M. Hanussek, J.-S. Kim, and C. H. Kom, *Neutrino masses and mixings in the baryon triality constrained minimal supersymmetric standard model*, Phys. Rev. **D84** (2011) 113005, `arXiv:1106.4338 [hep-ph]`.

[96] W. Porod, M. Hirsch, J. Romao, and J. W. F. Valle, *Testing neutrino mixing at future collider experiments*, Phys. Rev. **D63** (2001) 115004, `arXiv:hep-ph/0011248`.

[97] M. A. Diaz, M. Hirsch, W. Porod, J. C. Romao, and J. W. F. Valle, *Solar neutrino masses and mixing from bilinear R parity broken supersymmetry: Analytical versus numerical results*, Phys. Rev. **D68** (2003) 013009, `arXiv:hep-ph/0302021`.

[98] R. D. Peccei and H. R. Quinn, *CP conservation in the presence of pseudoparticles*, Phys. Rev. Lett. **38** (1977) 1440–1443.

[99] R. D. Peccei and H. R. Quinn, *Constraints imposed by CP conservation in the presence of pseudoparticles*, Phys. Rev. **16** (1977) 1791–1797.

[100] S. Weinberg, *A new light boson?*, Phys. Rev. Lett. **40** (1978) 223–226.

[101] ATLAS Collaboration, *Search for long-lived, heavy particles in final states with a muon and a multi-track displaced vertex in proton-proton collisions at* $\sqrt{s} = 8$ *TeV with the ATLAS detector.*, `https://cds.cern.ch/record/1595755`.

[102] CMS Collaboration, *Search for long-lived particles that decay into final states containing two electrons or two muons in proton-proton collisions at* $\sqrt{s} = 8$ *TeV*, `arXiv:1411.6977 [hep-ex]`.

[103] Y. Kao and T. Takeuchi, *Single-coupling bounds on R-parity violating supersymmetry, an update*, `arXiv:0910.4980 [hep-ph]`.

[104] ATLAS Collaboration. `https://twiki.cern.ch/twiki/bin/view/AtlasPublic/LuminosityPublicResults`.

[105] ATLAS Collaboration, *Luminosity determination in pp collisions at* $\sqrt{s} = 7$ *TeV using the ATLAS detector at the LHC*, Eur. Phys. J. **C71** (2011) 1630, `arXiv:1101.2185 [hep-ex]`.

[106] ATLAS Collaboration, *The ATLAS experiment at the CERN Large Hadron Collider*, JINST **3** (2008) S08003.

[107] ATLAS Collaboration. `http://www.atlas.ch/photos/full-detector-cgi.html`.

[108] F. Kohn, A. Quadt, and C. Hensel, *Measurement of the charge asymmetry in top quark pair production in pp collision data at* $\sqrt{s} = 7$ *TeV using the ATLAS detector*. PhD thesis, Göttingen U., 2012. `arXiv:1204.0952 [hep-ex]`. CERN-THESIS-2012-024.

[109] ATLAS Collaboration, *ATLAS: Detector and physics performance technical design report. Volume 1*, `https://cds.cern.ch/record/391176`.

[110] ATLAS Collaboration, *Electron efficiency measurements with the ATLAS detector using the 2012 LHC proton-proton collision data*, `https://cds.cern.ch/record/1706245`.

[111] ATLAS Collaboration, *Measurement of the muon reconstruction performance of the ATLAS detector using 2011 and 2012 LHC proton-proton collision data*, Eur. Phys. J. **C74** no. 11, (2014) 3130, `arXiv:1407.3935 [hep-ex]`.

[112] ATLAS Collaboration, *Jet energy measurement and its systematic uncertainty in proton-proton collisions at* $\sqrt{s} = 7$ *TeV with the ATLAS detector*, Eur. Phys. J. **C75** (2015) 17, `arXiv:1406.0076 [hep-ex]`.

[113] M. Cacciari, G. P. Salam, and G. Soyez, *The anti-*$k_t$ *jet clustering algorithm*, JHEP **0804** (2008) 063, `arXiv:0802.1189 [hep-ph]`.

[114] ATLAS Collaboration, *Calibration of b-tagging using dileptonic top pair events in a combinatorial likelihood approach with the ATLAS experiment*, `https://cds.cern.ch/record/1664335`.

[115] ATLAS Collaboration, *Identification and energy calibration of hadronically decaying tau leptons with the ATLAS experiment in pp collisions at* $\sqrt{s} = 8$ *TeV*, `arXiv:1412.7086 [hep-ex]`.

[116] ATLAS Collaboration, *Performance of missing transverse momentum reconstruction in proton-proton collisions at 7 TeV with ATLAS*, Eur. Phys. J. **C72** (2012) 1844, `arXiv:1108.5602 [hep-ex]`.

[117] N. Metropolis and S. M. Ulam, *The Monte Carlo method*, J. Amer. Stat. Assoc. **44** (1949) 335–341.

[118] B. R. Webber, *A QCD model for jet fragmentation including soft gluon interference*, Nucl. Phys. **B238** (1984) 492.

[119] GEANT4 Collaboration, *GEANT4: A simulation toolkit*, Nucl. Instrum. Meth. **A506** (2003) 250–303.

[120] ATLAS Collaboration, *The ATLAS simulation infrastructure*, Eur. Phys. J. **C70** (2010) 823–874, `arXiv:1005.4568 [physics.ins-det]`.

[121] ATLAS Collaboration, *The simulation principle and performance of the ATLAS fast calorimeter simulation FastCaloSim*, `https://cds.cern.ch/record/1300517`.

[122] ATLAS Collaboration, *Search for squarks and gluinos with the ATLAS detector in final states with jets and missing transverse momentum using $\sqrt{s} = 8$ TeV proton-proton collision data*, JHEP **1409** (2014) 176, `arXiv:1405.7875 [hep-ex]`.

[123] ATLAS Collaboration, *Search for new phenomena in final states with large jet multiplicities and missing transverse momentum at $\sqrt{s} = 8$ TeV proton-proton collisions using the ATLAS experiment*, JHEP **1310** (2013) 130, `arXiv:1308.1841 [hep-ex]`.

[124] ATLAS Collaboration, *Search for direct third-generation squark pair production in final states with missing transverse momentum and two b-jets in $\sqrt{s} = 8$ TeV pp collisions with the ATLAS detector*, JHEP **1310** (2013) 189, `arXiv:1308.2631 [hep-ex]`.

[125] ATLAS Collaboration, *Search for squarks and gluinos in events with isolated leptons, jets and missing transverse momentum at $\sqrt{s} = 8$ TeV with the ATLAS detector*, `arXiv:1501.03555 [hep-ex]`.

[126] ATLAS Collaboration, *Search for direct production of charginos, neutralinos and sleptons in final states with two leptons and missing transverse momentum in pp collisions at $\sqrt{s} = 8$ TeV with the ATLAS detector*, JHEP **1405** (2014) 071, `arXiv:1403.5294 [hep-ex]`.

[127] ATLAS Collaboration, *Search for direct top squark pair production in events with a Z boson, b-jets and missing transverse momentum in $\sqrt{s} = 8$ TeV pp collisions with the ATLAS detector*, Eur. Phys. J. **C74** (2014) 2883, `arXiv:1403.5222 [hep-ex]`.

[128] ATLAS Collaboration, *Search for direct production of charginos and neutralinos in events with three leptons and missing transverse momentum in $\sqrt{s}$ = 8 TeV pp collisions with the ATLAS detector*, JHEP **1404** (2014) 169, `arXiv:1402.7029 [hep-ex]`.

[129] ATLAS Collaboration, *Search for supersymmetry at $\sqrt{s}$ = 8 TeV in final states with jets and two same-sign leptons or three leptons with the ATLAS detector*, JHEP **1406** (2014) 035, `arXiv:1404.2500 [hep-ex]`.

[130] ATLAS Collaboration, *Search for supersymmetry in events with four or more leptons in $\sqrt{s}$ = 8 TeV pp collisions with the ATLAS detector*, Phys. Rev. **D90** (2014) 052001, `arXiv:1405.5086 [hep-ex]`.

[131] S. D. Drell and T.-M. Yan, *Massive lepton pair production in hadron-hadron collisions at high-energies*, Phys. Rev. Lett. **25** (1970) 316–320.

[132] M. Baak, G. J. Besjes, D. Cote, A. Koutsman, J. Lorenz, et al., *HistFitter software framework for statistical data analysis*, `arXiv:1410.1280 [hep-ex]`.

[133] ATLAS Collaboration, *Search for massive supersymmetric particles decaying to many jets using the ATLAS detector in pp collisions at $\sqrt{s}$ = 8 TeV*, `arXiv:1502.05686 [hep-ex]`.

[134] F. E. Paige, S. D. Protopopescu, H. Baer, and X. Tata, *ISAJET 7.69: A Monte Carlo event generator for pp, $\bar{p}p$, and $e^+e^-$ reactions*, `arXiv:hep-ph/0312045`.

[135] MSSM Working Group Collaboration, A. Djouadi et al., *The minimal supersymmetric Standard Model: Group summary report*, `arXiv:hep-ph/9901246`.

[136] M. Bahr, S. Gieseke, M. A. Gigg, D. Grellscheid, K. Hamilton, et al., *Herwig++ physics and manual*, Eur. Phys. J. **C58** (2008) 639–707, `arXiv:0803.0883 [hep-ph]`.

[137] W. Beenakker, R. Hopker, M. Spira, and P. M. Zerwas, *Squark and gluino production at hadron colliders*, Nucl. Phys. **B492** (1997) 51–103, `arXiv:hep-ph/9610490`.

[138] A. Kulesza and L. Motyka, *Threshold resummation for squark-antisquark and gluino-pair production at the LHC*, Phys. Rev. Lett. **102** (2009) 111802, `arXiv:0807.2405 [hep-ph]`.

[139] A. Kulesza and L. Motyka, *Soft gluon resummation for the production of gluino-gluino and squark-antisquark pairs at the LHC*, Phys. Rev. **D80** (2009) 095004, `arXiv:0905.4749 [hep-ph]`.

[140] W. Beenakker, S. Brensing, M. Krämer, A. Kulesza, E. Laenen, et al., *Soft-gluon resummation for squark and gluino hadroproduction*, JHEP **0912** (2009) 041, `arXiv:0909.4418 [hep-ph]`.

[141] W. Beenakker, S. Brensing, M. Krämer, A. Kulesza, E. Laenen, et al., *Squark and gluino hadroproduction*, Int. J. Mod. Phys. **A26** (2011) 2637–2664, `arXiv:1105.1110 [hep-ph]`.

[142] M. Krämer, A. Kulesza, R. van der Leeuw, M. Mangano, S. Padhi, et al., *Supersymmetry production cross sections in pp collisions at* $\sqrt{s} = 7$ *TeV*, `arXiv:1206.2892 [hep-ph]`.

[143] J. Alwall, M. Herquet, F. Maltoni, O. Mattelaer, and T. Stelzer, *MadGraph 5: Going beyond*, JHEP **1106** (2011) 128, `arXiv:1106.0522 [hep-ph]`.

[144] T. Sjostrand, S. Mrenna, and P. Z. Skands, *PYTHIA 6.4 physics and manual*, JHEP **0605** (2006) 026, `arXiv:hep-ph/0603175`.

[145] G. Cowan, K. Cranmer, E. Gross, and O. Vitells, *Asymptotic formulae for likelihood-based tests of new physics*, Eur. Phys. J. **C71** (2011) 1554, `arXiv:1007.1727 [physics.data-an]`.

[146] *Search for supersymmetry in events with four or more leptons in* $\sqrt{s} = 8$ *TeV pp collisions with the ATLAS detector*, `http://hepdata.cedar.ac.uk/view/ins1297226/`.